

***The 2001 NNUN REU
Research Accomplishments***



The 2001 NNUN REU Research Accomplishments

Table of Contents

<p><i>The 2001 NNUN REU Interns</i> 2</p> <p><i>The 2001 NNUN Research Experience for Undergraduates Program</i> 3</p> <p><i>The National Nanofabrication Users Network</i> 4</p> <p><i>Cornell Nanofabrication Facility</i> 5</p> <p>Nanoimprinting by Hot Embossing in Polymer Substrates 6</p> <p>VLSI Interconnect Characterization for Deep-Submicron Technology 8</p> <p>Novel Method for Large Scale NanoPatterning 10</p> <p>Fabrication and Optimization of Organic Thin-Film Transistors .. 12</p> <p>The Fabrication and Characterization of Silicon Tips for the Deposition of Gallium Phosphide 14</p> <p>Chemical Mechanical Polishing Characterization and Process Development 16</p> <p>Studies of the Formation of Sub-Surface Voids in Silicon Substrate Induced by Silicon Surface Migration 18</p> <p>Evaluation of Collagen as a Molecular Filtration Material 20</p> <p>Construction of Thin Optical Microcuvettes 22</p> <p>Development of Ultramicroelectrode Arrays for Microfluidic Biosensor Devices 24</p> <p>Processing of Next Generation Resist Materials using Supercritical CO₂ 26</p> <p>Process Characterization of LPCVD Silicon Nitride and the Consequential Fabrication of Low Stress Microcantilevers 28</p> <p><i>Howard University, Materials Science Research Center of Excellence</i> 31</p> <p>Characterization of Peptide Sorption onto GaAs (100) Surfaces by AFM, Optical Microscopy and FT-IR Spectroscopy 32</p> <p>The Growth and Characterization Processes of Gallium Nitride (GaN) Nanowires 34</p> <p>InGaAsN Solar Cells made by Molecular Beam Epitaxy 36</p> <p>Fabrication of 3C-SiC Nanofiltration Membranes 38</p> <p><i>The Penn State Nanofabrication Facility</i> 41</p> <p>Study of Gamma-Aminopropyltriethoxysilane Coatings on Glass Substrates for DNA Microarrays 42</p> <p>Investigation of Cell Differentiation and Film Behavior of Nanofabricated Thin Films 44</p> <p>Enhancement of Large Molecule Detection and Signal Sensitivity for MASiF 46</p> <p>Fabrication and CV & IV Characteristics of Metal-Insulator-Metal Structures 48</p> <p>Fabrication and Superconductivity of Ge/Ag/Ge Nanowires 50</p> <p>Nanoscale Patterns and Networks made by Molecular Rulers grown on Dot Arrays formed by Nanosphere Lithography 52</p>	<p><i>Stanford Nanofabrication Facility</i> 55</p> <p>Electron Beam Lithography of Nanoscale Hall Probes for Scanning Microscopy 56</p> <p>Integration of Nanotubes into Devices 58</p> <p>Alignment System of Distributed Axis Multiple Beam Electron Lithography 60</p> <p>Development of a Microfluidic System for Separation of Lipids with Various Composition Ratios 62</p> <p>Optimizing DNA “Inks” for Microarrays 64</p> <p>Flow-Through Processing on a Microchip for DNA Pyrosequencing® 66</p> <p>Analysis of Electron Emission from Diamond using an E-Beam Micro-Column 68</p> <p>Minimum Line-Width Features for Cryogenic Optical Photon Detectors 70</p> <p>The Integration of Carbon Nanotubes into Electronic Devices..... 72</p> <p>Characterizing the Viscosity of Concentrated Solutions of DNA with Cationic Agents 74</p> <p>Microfluidics for DNA Pyrosequencing 76</p> <p>Magnetostrictive Thin Films for MEMS Applications 78</p> <p><i>UCSB Nanofabrication Facility</i> 81</p> <p>Engineering Protein Molecules for the Ordered Structuring of Silica 82</p> <p>The Effects of Penetration Point on Quantitative Drug Delivery by Jet Injection 84</p> <p>Evaluation of Novel Growth Techniques for Dislocation Reduction in Gallium Nitride 86</p> <p>Cavitation Surface Effects of Low Frequency Ultrasound 88</p> <p>Development of a C⁺ Program to Study Five-Layer, Thin-Film Systems using Multiple Beam Interferometry 90</p> <p>Photoluminescence and AFM on Strain-Coupled, Self-Assembled InAs Quantum Dots and Quantum Rings 92</p> <p>AFM Image De-Convolution on Synthetic Spider Silk Protein Fiber 94</p> <p>MicroElectroMechanical Chemical Sensors 96</p> <p>Asymmetric Diblock Copolymer Films for Nanopatterning 98</p> <p>Spectroscopy of the Ir³⁺ Organo-Metallic Complexes 100</p> <p>Conformational Analysis of Phenylenevinylene Oligomers 102</p> <p><i>Index</i> 105</p>
---	---

Cover image of a GaN nanowire under test by Unyime Eshiet, 2001 NNUN REU intern at Howard University, Harris Research Group

The 2001 NNUN REU Interns

Intern	School Affiliation	Field of Study	NNUN Site	Page
Ms. Sara Alvarez	UCSB	BioSci	UCSB	82
Ms. Anna Bacon	Michigan State University	MatSciEngr	CNF	6
Ms. Nitasha Bakhru	Rensselaer Polytech Inst	BioSci	UCSB	84
Mr. Lukmaan Bawazer	The Ohio State University	MatSciEngr	UCSB	86
Mr. Noah Beck	Harvey Mudd College	Engr/Physics	SNF	56
Ms. Teresa Bixby	Susquehanna University	Chem/Physics	PSU	42
Mr. Julio Bracero Rodriguez	University of PR Mayaguez	Biology/PreMed	Howard	32
Ms. Mary Brickey	University of IL at Chicago	BioChem/Spanish	UCSB	88
Mr. Arthur Carter	Wake Forest University	Chemistry	PSU	44
Ms. Aileen Chang	UC Berkeley	Physics	SNF	58
Mr. Philip Choi	Cornell University	EE	CNF	8
Mr. Matthew Daniels	Pacific Lutheran University	Physics	CNF	10
Mr. Andrew Davenport	Washington University, St. Louis	MechEngr	SNF	60
Ms. Caitlin Devereaux	Harvey Mudd College	Chemistry	CNF	12
Mr. Peter Ercius	Cornell University	AEP	UCSB	90
Ms. Unyime Eshiet	Temple University	EE/CompSci	Howard	34
Ms. Jamie Fontaine	The Pennsylvania State University	Genetics	PSU	46
Ms. Danna Freedman	Harvard University	Chemistry	CNF	14
Ms. Ashley Harness	Virginia Commonwealth Univ	ChemEng	CNF	16
Mr. Damon Hebert	Macalester College	Physics	UCSB	92
Ms. Sondra Hellstrom	Johns Hopkins University	EE	SNF	62
Ms. Samar Hubbi	New Jersey Institute	EngrSci	SNF	64
Mr. Noel Jensen	Colorado College	Physics	SNF	66
Mr. Matthew Kittle	University of Michigan	Chem&MatSciEngr	UCSB	94
Ms. Kate Klein	Trinity College	Engr/Spanish	SNF	68
Mr. Robert Klein	UCSB	ChemEng	Howard	36
Ms. Hayley Lam	UC Berkeley	BioEngr	UCSB	96
Ms. Joy Liu	UC Berkeley	EE/CompSci	PSU	48
Ms. Natalie Lui	Harvard University	Physics	SNF	70
Ms. Fatou Maiga	NC State University	ChemEng	CNF	18
Mr. Brian Manuel	Morehouse College	MechEngr	CNF	20
Ms. Meredith McElroy	University of South Carolina	ChemEng	CNF	22
Mr. Nathan Morris	Messiah College	Chemistry	SNF	72
Ms. Laura Moussa	Binghamton University	Chemistry	CNF	24
Ms. Linda Ohsie	Dartmouth College	BioChem	SNF	74
Mr. Nagesh Rao	Rensselaer Polytechnic Institute	MatEngr/Phil	CNF	26
Mr. Gregory Roman	Bard College	Chemistry	CNF	28
Ms. Heather Russell	Pacific Lutheran University	Physics	PSU	50
Ms. Kathleen Schaefer	University of Pittsburgh	Chemistry	UCSB	98
Mr. Jonathan Schuller	UCSB	Physics	SNF	76
Mr. Metages Sisay	Santa Clara University	EngrPhysics	UCSB	100
Ms. Marina Sofos	Brown University	MatEngr	SNF	78
Mr. Chau Tang	University of Southern Mississippi	PolymerSci	UCSB	102
Ms. Linh My Tran	UCLA	ChemEng	UCSB	90
Mr. Court Wilson	Trinity College / Duke University	Chemistry	Howard	38
Mr. Alexander Wissner-Gross	MIT	Physics/EE/Math	PSU	52

The 2001 NNUN Research Experience for Undergraduates Program



The 2001 NNUN REU Convocation at Howard University, Washington D.C., August 2001

This year was the worst so far! 202 applications for only 42 internships. It was awful. As the NNUN REU program becomes more and more popular, the award process becomes harder and harder. Not to mention having to enter all that information into a database!

But somehow we survived, and hired our 2001 NNUN REU interns. They came from Bard College to Washington University, majoring in Biological Chemistry through to Physics. We hired 24 women and 18 men - a first! And you may notice that the section for the University of California Santa Barbara has a few more reports than their reported number of interns - 8. That's because UCSB had so many great projects to research, they decided to hire 4 extra interns with their own funds but include them in the NNUN REU process. Those reports are included here because the students did excellent work worth reporting, even though they were not covered under the NSF REU contract.

As I say, the more popular the program becomes, the harder it is to turn down motivated researchers.

As always, we are indebted to the NSF. Drs. Mary Poats and Rajinder Khosla were patient and encouraging. In addition, we would like to thank the following companies for their financial support:

Agilent Technologies, Advanced Micro Devices, Analog Devices, Inc., Applied Materilas, Ericsson, Hewlett-Packard Co., Hitachi, Ltd., Infineon, IBM, Intel, Motorola, National Semiconductor, Panasonic, Philips, Robert Bosch Corporation, Taiwan Semiconductor Mfg. Corp., Texas Instruments, Toshiba, Varian Semiconductor Equipment Associates, and Xerox Corporation.

Each year, it is only because of the kind attentions of our NNUN REU site coordinators and staff that anything gets done at all. So a warm and well-deserved 'thank you' to Denise, Marsha, Mike, Yvette, James, Crawford, Lisa, Mark, Jane, Mike, Liu-Yen, Holly and Kirsten.

*Melanie-Claire Mallison
NNUN REU Program Coordinator*

The National Nanofabrication Users Network (NNUN)

URL: <http://www.nnun.org/>

Stanford Nanofabrication Facility
Prof. John Shott, Interim Director

Stanford University
CIS 129, Via Ortega St
Stanford CA 94305-4085

Voice: (650) 725-3715

Fax: (650) 725-6278

URL: <http://www-snf.stanford.edu/>

Cornell Nanofabrication Facility

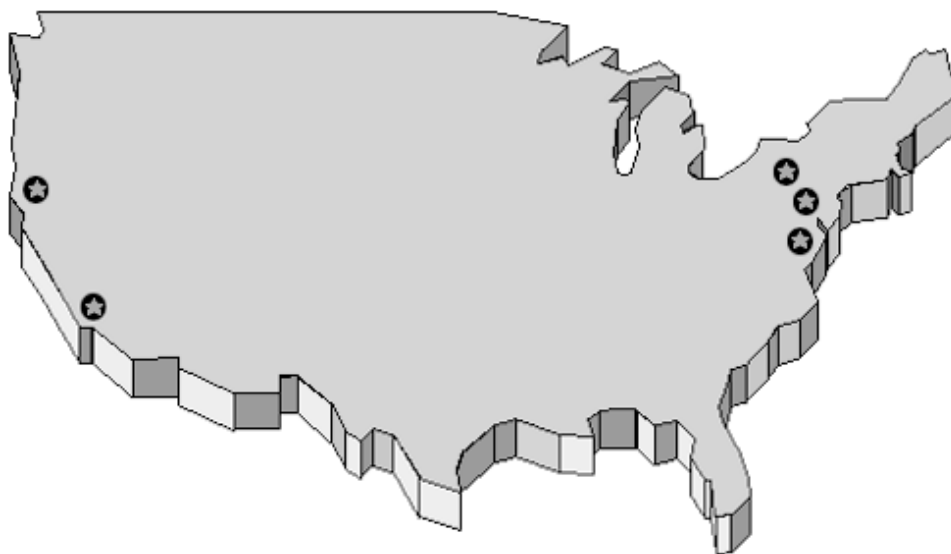
Prof. Sandip Tiwari, Director
Cornell University

Knight Laboratory, CNF
Ithaca, New York 14853-5403

Voice: (607) 255-2329

Fax: (607) 255-8601

URL: <http://www.cnf.cornell.edu/>



UCSB Nanofabrication Facility

Prof. Mark Rodwell, Director

University of California at Santa Barbara

Department of Electrical & Computer Engineering

Santa Barbara, CA 93106-9560

Voice: (805) 893-3244

Fax: (805) 893-8544

URL: <http://www.nanotech.ucsb.edu/>

The Penn State Nanofabrication Facility

Prof. Stephen Fonash, Director

The Pennsylvania State University

189 Materials Research Institute

University Park, PA 16802

Voice: (814) 865-4931

Fax: (814) 865-3018

URL: <http://www.nanofab.psu.edu/start/default.htm>

Materials Science Research Center for Excellence

Prof. Gary Harris, Director

Howard University School of Engineering

2300 Sixth St, NW

Washington, D.C. 20059

Voice: (202) 806-6618

Fax: (202) 806-5367

URL: <http://www.msrce.howard.edu/~nanonet/NNUN.HTM>

**Cornell Nanofabrication Facility
Cornell University, Ithaca NY
<http://www.cnf.cornell.edu>**

2001 REU Interns



REU Intern School Affiliation Principal Investigator

Front Row, L to R:

Mr. Brian Manuel Morehouse College Michael Spencer
 Ms. Laura Moussa Binghamton University Antje Baeumner
 Ms. Fatou Maiga NC State University Michael Skvarla

Second Row, L to R:

Ms. Danna Freedman Harvard University James Engstrom
 Ms. Ashley Harness Virginia Commonwealth Univ Daniel Woodie
 Ms. Caitlin Devereaux Harvey Mudd College George Malliaras
 Ms. Melanie-Claire Mallison Cornell Nanofabrication Facility NNUN REU Coordinator

Third Row, L to R:

Mr. Philip Choi Cornell University Edwin Kan
 Mr. Nagesh Rao Rensselaer Polytechnic Institute Christopher Ober
 Mr. Gregory Roman Bard College Daniel Woodie
 Ms. Anna Bacon Michigan State University Sandip Tiwari
 Mr. Matthew Daniels Pacific Lutheran University Jack Blakely
 Ms. Meredith McElroy University of South Carolina Andreas Albrecht
 Mr. Daniel Woodie Cornell Nanofabrication Facility CNF Staff and REU PI

Nanoimprinting by Hot Embossing in Polymer Substrates

Anna E. Bacon, Material Science and Engineering,
Michigan State University, baconann@msu.edu

Principal Investigator(s): Sandip Tiwari, Lynn Rathbun, Cornell Nanofabrication Facility,
Cornell University, st222@cornell.edu, rathbun@cnf.cornell.edu

Abstract:

This project details the process for Nanoimprinting by Hot Embossing with the EV-520. Trials were performed with templates having raised features sized 300 μm to 50 nm. Hot Embossing was performed on bulk polymer and polymer spun on standard 4" silicon wafers. Processes were characterized qualitatively and results are shown by optical microscopy.

Introduction:

Nanoimprinting is the process of transferring a pattern from template to substrate by physical contact. Hot Embossing Lithography is the subset of nanoimprinting which uses downward piston pressure and raised temperature to bring the substrate and template into contact and cause the polymer to flow and take the shape of the pattern. After the temperature cools the piston pressure is released, and the pattern will be transferred.

Experimental Procedure:

This project involved the EV-520 hot embossing machine. This machine uses a pressure controlled chamber with temperature controlled chucks for the embossing. The top and bottom chucks have independent temperature control. A piston mechanism normal to the two chucks applies the downward force needed to transfer the pattern. Templates were created with patterns in order to conduct embossing trials to characterize how effective the embossing process is under different temperatures and piston force. All trials were conducted at atmospheric pressure with a hold time of 10 minutes.

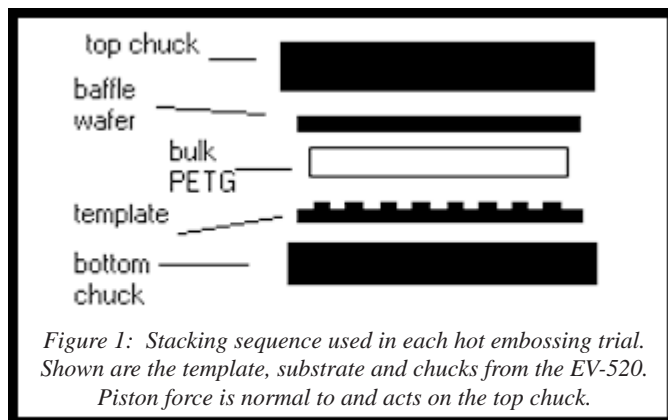


Figure 1: Stacking sequence used in each hot embossing trial. Shown are the template, substrate and chucks from the EV-520. Piston force is normal to and acts on the top chuck.

The variables examined in this project included the top and bottom temperature and the piston pressure. The temperature is raised on the bottom and top chucks. When the desired temperature is reached the piston force is applied. A time is chosen to hold the pressure. The temperature should be lowered to below the glass transition temperature and then the piston is raised. A plot of this process is shown in figure 1. The embossing stack should be further cooled in the chamber to reduce shrinkage caused by quick cooling as the stack comes into contact with air.

Three templates were created on silicon wafers that had a layer of approximately 600 nm of SiO_2 grown on the surface. The first template was created using photolithography and reactive ion etching. The photolithography process used a positive field mask, and then the template was subjected to image reversal. This left the pattern as raised features. The features were an array of lines and dots with size and spacing ranging from 1 μm , 2 μm pitch to 2 μm , 10 μm pitch. The features were reactive ion etched to depths of 200 nm, 300 nm, and 10 μm . These templates were used to emboss bulk PETG and PMMA spun on a Si wafer. The PMMA was spun on at a thickness of 900 nm. One trial was performed on the PMMA spun-coat wafer. The temperature of the top and bottom chucks (T_t and T_b) was 107°C and piston pressure 7000N.

The second template was created using e-beam lithography and reactive ion etching. The features had a height of 100 nm raised above the surface. Features on the template were an array of lines sized 50 nm, 50 nm pitch. It was used to emboss onto the bulk PETG. One trial was performed with T_t and T_b set to 100°C and piston lowered to 4000N.

The third template was a previously produced pattern microfluidic device. It was used to pattern into the bulk PETG. For this template, again, the features were raised from the surface. Size of features ranged from 300 μm width of a cell to 50 μm width of a channel. Trials were conducted with T_t and T_b set to 105°C with a piston force of 7000N.

The machine will transfer a pattern, template to substrate, one at a time. The set up was to place the template, pattern up, on the bottom chuck. The substrate

was then placed on top of that. A baffle wafer separated the plastic from the top chuck. Figure 1 illustrates the stacking sequence that was used for each trial.

Results:

Table 1, below, shows the qualitative results from the trials with the general template in the bulk PETG. The general template was used once to transfer the pattern into the PMMA spun onto a Si wafer. The trial on PMMA resulted in a nice pattern transfer, but the PMMA pulled up from the wafer in between dies. The e-beam lithography template was only used for one trial, and it broke upon release. The pattern was not transformed uniformly across the bulk. A few dies were transformed and showed faithful, if partial reproduction of the pattern in the 50 nm size. The result from the microfluidic template, shown by optical micrograph in figure 2, saw some thermal distortion.

The trials that cooled the sample near ambient before lifting piston force were more likely to result in a broken template. Lowering the temperature about 5°, raising the piston, and then further cooling the sample to near room temperature was less likely to break the template.

Discussion:

For larger patterns, such as the microfluidic pattern, temperatures around 100°C produced good results. For smaller patterns, it would have to be determined what properties were desired and needed, and a temperature and force could be chosen for processing. Further trials should be investigated before drawing conclusions on PMMA spun wafers and embossing for feature size < 100nm.

Acknowledgements:

I would like to thank Mandy Esch and Uygur Avci for all of their time and help with this project.

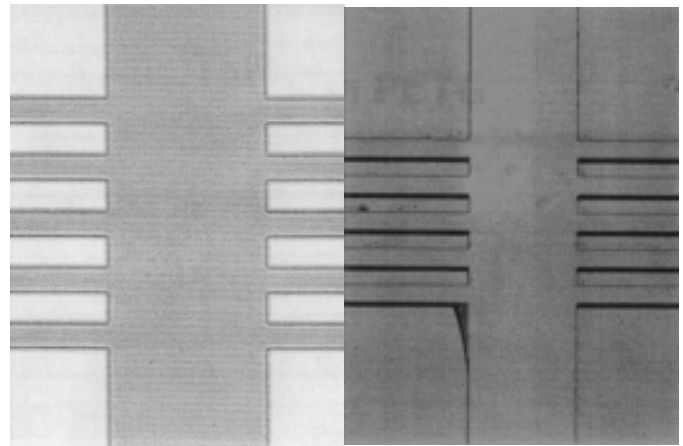


Figure 3: Microfluidic pattern hot embossed in bulk PETG. Main channel width 300 μm, side channel widths 50 μm. Optical micrograph shown at 100x.

Table 1, below: Qualitative results from general template trial

- F = Faithful Reproduction of Shape, Not Clean
- R = Surface Ripples of Bulk Plastic that deform pattern
- U = Uniformity of Pattern Across the Bulk
- D = Deformation of Bulk Shape
- C = Clean Edge Line of Embossed Pattern, and Faithful Reproduction of Shape

Blank Cells Indicate No Trial Performed
 (* Heating rates only)

Force (N)	T _n °	AMB	75	80	98	100	100	120	105
	T _r °	AMB	40	45	60	60	100	110	105
3500									R, C, U, D
4000		No E	C	F			R, C, U	R, C, U, D	R, C, U, D
7000		No E	C	F	U	U			
10,000		No E	C	F					
20,000		No E	C						
30,000		C	C						
40,000		C	C						

VLSI Interconnect Characterization for Deep-Submicron Technology

Philip Choi, ECE, Cornell University, philip-choi@cornell.edu

*Principal Investigator(s): Prof. Edwin C. Kan, Electrical and
Computer Engineering, Cornell University, kan@ece.cornell.edu*

Mentor(s): Pingshan Wang and Myongseob Kim, ECE, Cornell University

Abstract:

Successful miniaturization of integrated circuit components has been the driving force behind the booming computer industry. When transistor structures are reduced in size, the switching time is also reduced, resulting in faster circuits. However, unfavorable results occur when the interconnecting wirings between transistors are made narrower and closer together. As the dimensions for Very Large Scale Integration (VLSI) circuits are continually reduced, electrical signal distortions and possible logic failures are imminent.

Primary focus of this project was geared towards the fabrication of copper testing structures which mimic interconnect lines. The samples were used to study the proximity effects on the resistance of the wires, and signal cross-talk between neighboring wires. Photolithographic patterning and lift-off processes were used to create the test structures.

Process Details:

Layouts of the desired testing structures were designed using L-Edit, the mask design program of Tanner Tools. Structures included simple transmission lines, pairs of coupled transmission lines, "serpentine" structures, and inductor loops as shown in Figure 1. Lines range from 1 μm to 8 μm wide and 1mm to 8mm long with spacing between coupled lines from 1 μm to 4 μm . These layouts

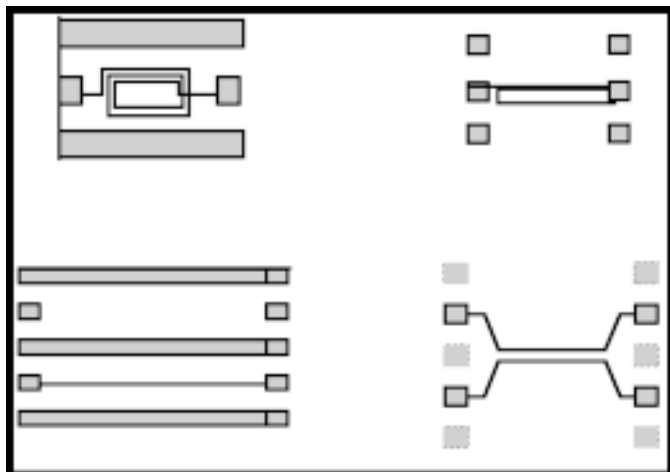


Figure 1: Structures included simple transmission lines, pairs of coupled transmission lines, "serpentine" structures, and inductor loops.

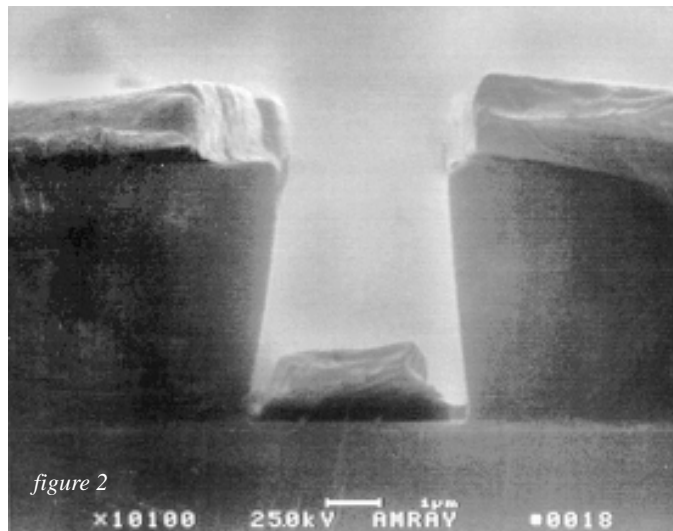
were transferred to chrome plated photomasks to be used in g-line lithography.

Standard photolithography can be accomplished relatively quickly and affordably on an available GCA 6300B DSW Wafer Stepper machine. Testing features on the order of 0.05 μm are highly desirable when one considers that industry standard CMOS lithography is in the 0.17 μm regime. Structures in this form factor will provide useful measurement and characterization data for future VLSI scaling. The smallest typical feature size definable by the GCA is 0.5 μm ; this limit is due to the physical wavelength of the g-line light. If, however, the photoresist on the wafer is overexposed, the originally designed micron sized features can be shrunk, hopefully to the desired 0.05 μm range.

To guarantee successful lift-off, a photoresist with a thickness approximately two to three times the desired 1.5 μm line thickness was needed; Microposit Shipley 1045 photoresist was used. Proper spin-on technique was developed to achieve an acceptably uniform thickness of 4 μm ; focus and exposure settings for the stepper were also varied to find optimal patterning and definition of the photoresist. Initial characterization and successful patterning of regular-sized (that is, normally-exposed) features was first accomplished. These wafers were baked in NH_3 to make the exposed regions less soluble to the developer. After a flood exposure and developer dip, image-reversed patterning (with re-entrant sidewall profiles) was achieved. Deposition of copper onto the wafers with a CVC SC-4500 electron-beam evaporator resulted in this profile, shown in Figure 2. Notice the clean discontinuity between the metalization on resist and on the wafer, resulting from the image-reverse sidewalls. These features ensured successful lift-off that was not hindered by thin connections between the desired transmission lines and the layer to be removed.

Analysis:

Interconnect structures were fabricated on thick SiO_2 surfaces, to ensure electrical isolation from the underlying substrate. The lines were made from Cu, because industrial VLSI interconnects are made from Cu (such as IBM's Cu process). Because the Cu would gradually oxidize, the wafers were tested and electrically

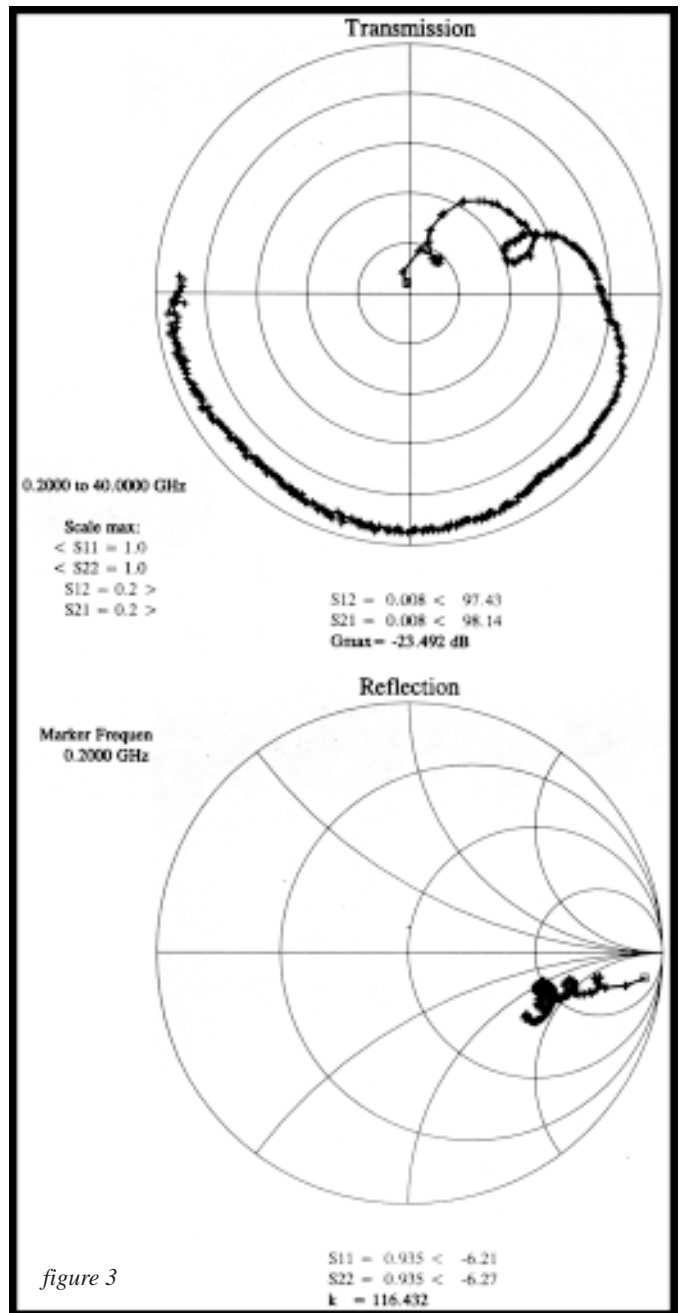


characterized three days after completion. Analysis was performed with an HP 85107 in an effort to derive the S-parameters of the interconnects. The network analyzer was used to transmit signals sweeping from 200 MHz to 40 GHz. Although interconnect lines of micron scale width are by no means novel, their frequency characterization, notably in the upper 20 to 40 GHz range, has not been thoroughly investigated yet. Results from the characterization of these relatively wide interconnect features can be used to model further S-parameter measurement of smaller, sub-micron features. At this point, only limited measurements have been performed. Figure 3 shows data gathered from a pair of 1 μm wide 1 mm long coupled transmission lines.

Future Work:

Further attempts at characterizing overexposure settings to create smaller width features were largely unsuccessful due to inconsistencies in width across the length of the transmission lines, as well as difficulties in reliably reproducing the same fabrication conditions from one wafer to the next. It is hypothesized that the resist thickness (which is greater than typical applications of 1 μm or less) is a contributing factor to the inconsistencies experienced in focus and definition.

All things considered, however, it is questionable whether the use of standard photolithography to produce these sub-micron features can be reliable. E-beam lithography, though more complex, may be more appropriate. The photomasks that were produced, as well as the CAD layouts, can be used for further lithography. Micron width structures can be reliably fabricated over a span of time with the methods developed, facilitating the gathering of S-parameter measurement by supplying “fresh” Cu interconnect structures with minimal contamination from oxide growth and electro-migration. More refinement in exposure settings and resist coating methods is required to create the sub-micron testing structures needed. Also, the inductor structures designed



require a three-mask process. All masks for the process have been created, facilitating future work in developing a reliable fabrication method for these devices.

References:

[1] J. A. Davis and J. D. Meindl, Compact Distributed RLC Interconnect Models-Part I: Single Line Transient, Time Delay, and Overshoot Expressions, IEEE Trans. Electron Devices, Vol. 47, No.11, 2000.

[2] Y. Eo, W. R. Eisenstadt, and J. Shim, S-Parameter-Measurement-Based High-Speed Signal Transient Characterization of VLSI Interconnects on SiO₂-Si Substrate, IEEE Trans. Advanced Packaging, Vol. 23, No.3, 2000.

Novel Method for Large Scale NanoPatterning

Matthew Daniels, Physics, Pacific Lutheran University, danielmj@plu.edu

Principal Investigator(s): Prof. Jack Blakely, Dr. Christopher Umbach, Materials Science, Cornell University, blakely@ccmr.cornell.edu, umbach@ccmr.cornell.edu

Abstract:

The focus of the project is to develop methods to etch periodic features in silicon (Si) that are 100 Å high and 200-300 Å apart. A silicon dioxide (SiO₂) film with a gradient in thickness is deposited on a silicon wafer. Sputtering the oxide in an ion mill at an off normal angle creates ripples on the oxide surface. These ripples are then used as an etch mask and the ripple pattern is transferred into the Si by a reactive ion etch (RIE). The quality of the pattern transfer depends on the oxide thickness, the degradation of the ripples during the etch and the initial long-wavelength roughness of the deposited oxide.

Introduction:

Large area nanoscale periodic surface corrugations (ripples) are formed when an ion beam's energy is deposited below the surface. An atom that receives the ion beam's energy is more likely to be ejected from areas of negative curvature which are closer to the energy deposition than from areas of positive curvature. Therefore, areas of negative curvature erode faster than areas of positive curvature. This increase in negative curvature is opposed by the viscous flow in the SiO₂ which smoothes out the SiO₂ surface. The balance between these two factors allows one wavelength to dominate and become the only wavelength on the surface of the sputtered samples after a short amount of time. The length of this wavelength depends on the ion beam's energy [1].

Procedure:

A 4" silicon wafer was placed in the CVC sputter deposition tool, and a film with a gradient of thickness of either SiO₂ or aluminum oxide was sputtered on to the wafer. This was done using the shutter to control the stationary deposition of the SiO₂. The gradient ranged from 5000 Å to 1000 Å across the wafer. It was scribed and broken into two to four pieces, and then placed in a Veeco Ion Mill at an off-normal angle of 45 degrees. Next the sample was milled for six to eight minutes with a beam and neutralizer density of 69 mA. After milling, the piece of the wafer was scribed and broken into several samples, which then had their SiO₂ thicknesses

characterized using an ellipsometer and a Leitz interferometer. A separate set of samples with a silicon substrate and thermally grown SiO₂ were placed in another ion mill. This ion mill created a gradient and the ripples in the samples at the same time. This was due to the fact that the mill's beam sputtered the sample at different rates with the center of the beam sputtering SiO₂ quicker than the outside. A Plasma Therm SSL-RIE 720 was then used to etch the samples with a Boron Tri-Chloride RIE. The voltages used for the etch ranged from 25 to 250 volts, with times ranging from thirteen seconds to twelve minutes. Finally, the samples were looked at in an Atomic Force Microscope (AFM) to determine if and where the ripples in the SiO₂ had been transferred to the silicon. The AFM was also used to look at how the ripples degraded with varying times and voltages.

Results and Conclusions:

Several interesting results were discovered. Using the AFM, we were able to determine that ripples did form on deposited SiO₂, which was not known before this summer. It was also discovered that ripple degradation depends on the voltage used in the RIE. Although the exact relationship is not yet known, we did discover that higher voltages degrade ripples much faster than lower voltages. Figure 1 demonstrates how the ripples degraded after being etched at 250 volts. As seen in figure 2, when a sample is etched at 50 volts, with the same amount of oxide removed, the ripple formation still exists.

Next, ripples have been transferred to the silicon substrate from a layer of thermally grown SiO₂ on the wafer. Although more characterization must be done on the ripples, the features from the AFM images are consistent with what is expected from the ripples being transferred into silicon. Figure 3 is an AFM image of the ripples before the RIE. The AFM image in Figure 4 shows the region where the SiO₂ has been milled almost down to the Si/SiO₂ interface. The surface profile of the ripples in Figure 4 after etching (Figure 5) shows a much higher amplitude than the ripples before etching. This is consistent with what we would find if the ripple pattern had been transferred into the silicon, with the crests of the ripples being SiO₂ and the troughs being silicon. Due to the fact that the ion etch etches silicon at a higher rate

than the SiO_2 , ripples with larger amplitudes are created.

Further work needs to be conducted using thermally grown oxide to transfer the ripple pattern into the silicon substrate. Work also needs to be done on using a smoother deposited aluminum oxide to form and transfer the ripples into the silicon substrate. Although it is known that crystalline aluminum oxide forms ripples, we believe the roughness of the deposited aluminum oxide used in our experiments stopped ripples from forming.

Acknowledgements:

I would like to thank Dr. Kit Umbach for his support, and the CNF and NNUN for the REU program.

References:

- [1] Spontaneous nanoscale corrugation of ion-eroded SiO_2 : the role of ion irradiation-enhanced viscous flow, C. C. Umbach, R. L. Headrick, K. Chang, Phys.Rev.Letter (under review).

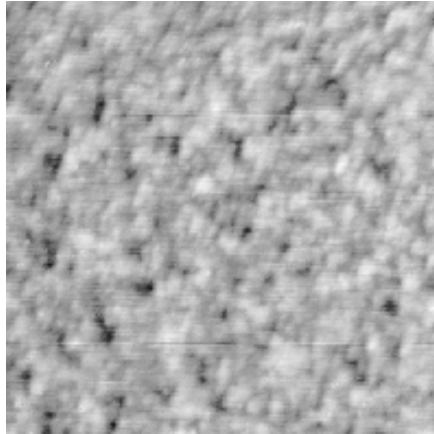


Figure 1: Rippled oxide surface after reactive ion etching at 250 volts. ($2\ \mu\text{m}$)

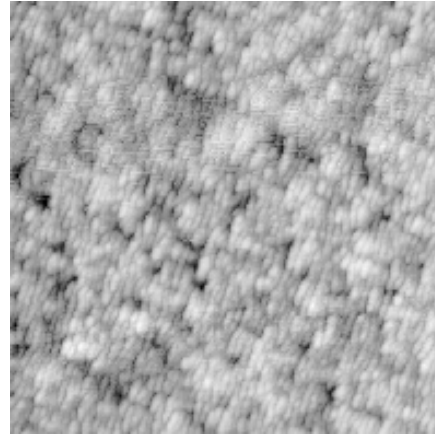


Figure 2: Rippled oxide surface after reactive ion etching at 50 volts. ($2\ \mu\text{m}$)

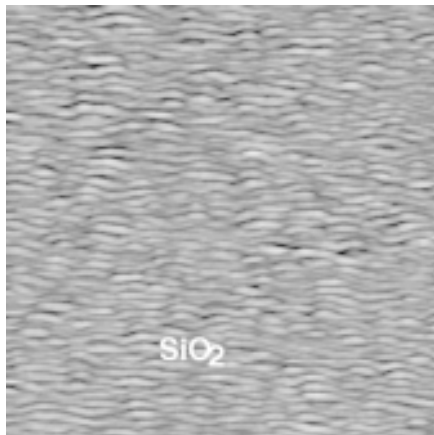


Figure 3: Rippled SiO_2 film on Si. ($3\ \mu\text{m}$)

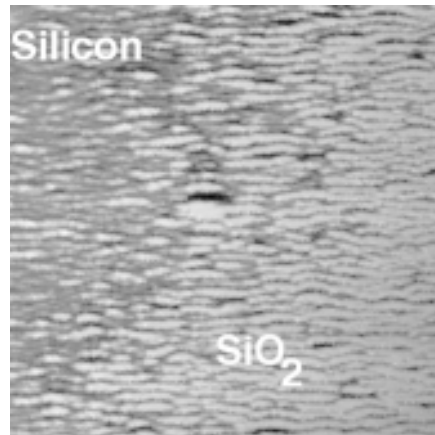


Figure 4: Area at the edge of an SiO_2 film on Si after ion etch. The ripple pattern has been transferred to the Si substrate. ($3\ \mu\text{m}$)

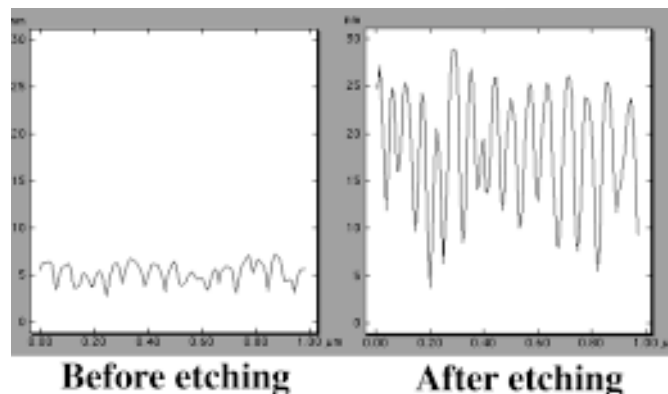


Figure 5: Line scans showing ripples before RIE and after RIE on an area where the film is very thin. The pattern has been successfully transferred to the Si.

Fabrication and Optimization of Organic Thin-Film Transistors

Caitlin Devereaux, Chemistry, Harvey Mudd College, cdevereaux@hmc.edu

Principal Investigator(s): George Malliaras, CCMR,
Cornell University, george@ccmr.cornell.edu

Mentor(s): Michele Swiggers, CCMR, Cornell University

Abstract:

Organic thin-film transistors (OTFTs) provide a useful alternative to conventional inorganic TFTs. The use of an organic conducting layer (pentacene, in our case) allows for inexpensive, low-temperature processing of the devices. These processing qualities make OTFTs ideal for flexible electronics and disposable electronics applications. The goal of the research was to improve OTFT performance by (1) varying the dimensions and spacing of the source and drain electrodes and (2) changing the type of material used for the electrodes. A variety of OTFT devices were fabricated via photolithographic methods and were characterized electrically.

Introduction:

Transistors are ubiquitous in today's electronics-rich world. The structure of a thin-film transistor (TFT) is shown in Figure 1. Inorganic TFTs use amorphous silicon as a transport layer and are used in most electronics applications because they have desirable electrical properties such as high mobility and large on/off ratios. Mobility is a measure of how easily charge carriers can move in the device. High mobility is needed for devices in which data must be transferred quickly.

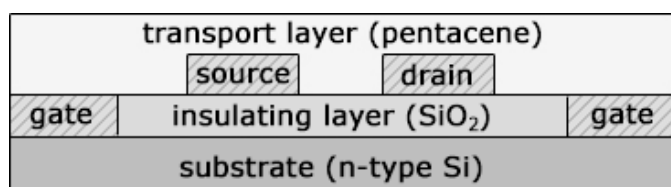


Figure 1. Thin-film transistor layout

Organic thin-film transistors (OTFTs) use small organic molecules or conducting polymers as the transport layer. OTFTs can be fabricated at low temperatures, which allows the use of flexible plastic substrates. Additionally, the organic molecules used in the transport layer can be applied by spin-coating, which allows fast, inexpensive coverage of large areas. OTFT mobilities are quickly approaching those of inorganic amorphous silicon TFTs [1], but mobility still must be improved before OTFTs will replace inorganic TFTs in

the electronics industry.

The following research looked at two possible factors in improving OTFT mobility. First was the dimensions of the source and drain electrodes as well as the separation between the two. The second factor under investigation was the electrode material.

Procedure:

A set of chrome/glass masks was created using CAD and the Mann 3600 Pattern Generator. These masks contained an array of 320 source-drain pairs as well as three gate contact pads. The channel length (L) was 2, 5, 10, 20, or 50 μm , and the channel width (W) was either 250 or 500 μm . Each combination of channel dimensions was repeated 32 times over the mask to ensure

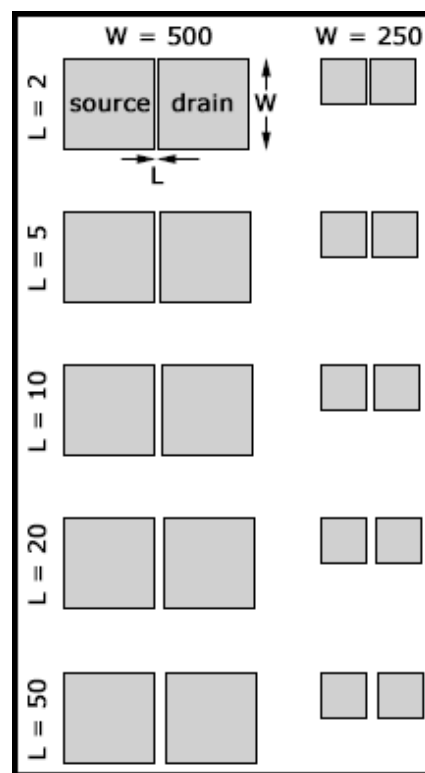


Figure 2. Device array containing 10 source-drain pairs (all values in microns)

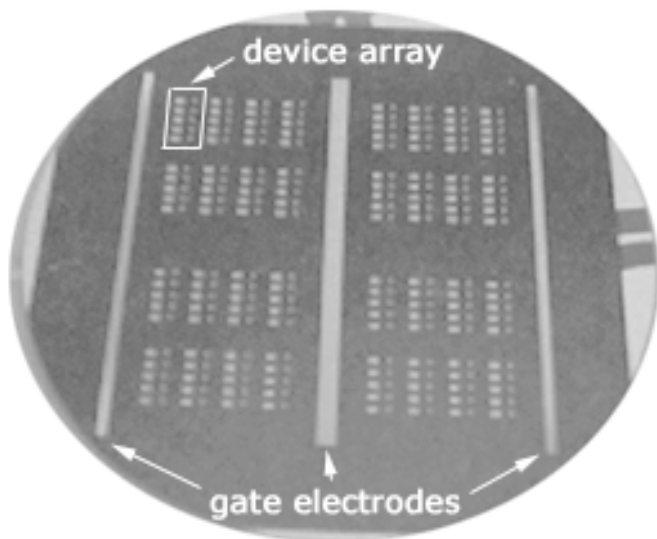


Figure 3. Completed 3 inch wafer

reproducibility of the data.

Devices were fabricated in a two-step lithographic process, followed by metal deposition and lift-off. First, a layer of silicon oxide, 3000Å thick, was thermally grown on heavily-doped n-type silicon wafers by Phil Infante (CNF). Shipley 1813 photoresist was used in both lithographic steps. The gate pattern was transferred to this resist layer using the Hybrid Technology Group (HTG) 3HR contact aligner. The pattern was then etched through the silicon oxide into the silicon (4000Å deep) with the Plasma Therm 72 Reactive Ion Etcher.

Following removal of the residual resist, a new layer of resist was applied and patterned with the source-drain array as well as the gate electrodes. After image reversal to obtain a retrograde profile, the electrode metal was deposited in one of two ways: (1) 500Å of Au (with a 10Å Cr adhesion layer) was deposited using the CHA RAP-600 Thermal Evaporator or (2) 500Å of Pt (with a 10Å Ti adhesion layer) was deposited using the CVC SC4500 Electron Gun Evaporator. Excess metal was removed by soaking wafers in acetone for 12 hours. Finally, a layer of pentacene (500Å thick) was thermally deposited on the wafers.

Devices were tested using the Keithley I-V Measurement System. Care was taken to make intimate contact between the probe needles and the source-drain electrodes. For each source-drain pair, a family of I-V curves was obtained for gate voltages ranging from 0 to -110V. Mobility (μ) was determined by plotting the square root of the saturation current for each I-V curve versus the corresponding gate voltage.

Results and Conclusions:

Mobilities obtained ranged from 0.0002 to 0.004 $\text{cm}^2/\text{V}\cdot\text{sec}$, two orders of magnitude lower than expected. The main cause

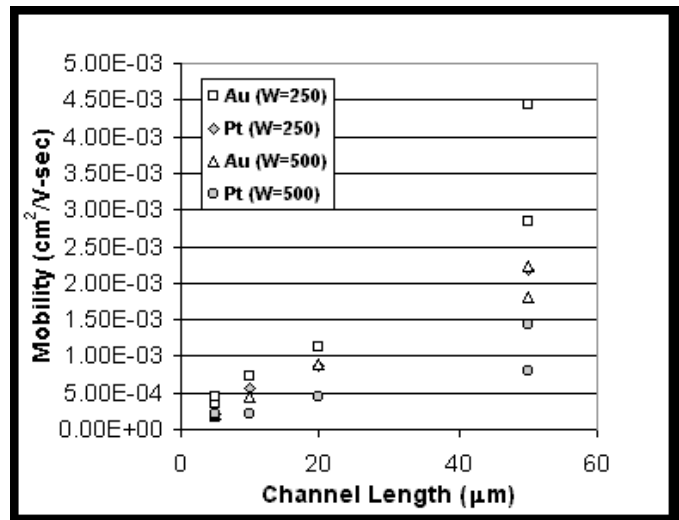


Figure 4. Plot of Mobility vs. Channel Length

of poor device performance was probably contamination of the electrodes. Both gold and platinum are quickly covered in a layer of oxide when exposed to air. Care was not taken to clean the electrodes before pentacene deposition, so it is likely that a thin layer of non-conducting oxide was present between the electrodes and pentacene, impeding charge injection.

Based on the mobility data summarized in Figure 3, it appears that gold electrodes work slightly better than platinum electrodes. Also, small electrodes with large spacing (L) give the best mobilities. These trends were reproducible but could have been affected by the unclean electrodes mentioned above.

In the future, the procedure outlined above should incorporate an electrode-cleaning step in order to improve performance. Additionally, smaller features should be investigated and flexible substrates, such as indium tin oxide (ITO), should be explored.

Acknowledgements:

I'd like to thank the National Science Foundation and the Cornell Nanofabrication Facility for giving me the opportunity to explore such an exciting field. Also, I'm forever grateful to George Malliaras for his wonderful attitude and encouragement throughout the summer.

References:

- [1] Gundlach, D.J.; H. Klauk; C.D. Sheraw; C.C. Kuo; J.R. Huang; T.N. Jackson Int. Electron Devices Meeting Technical Digest. December 1999.

The Fabrication and Characterization of Silicon Tips for the Deposition of Gallium Phosphide

Danna Freedman, Chemistry, Harvard University, freedm@fas.harvard.edu

Principal Investigator(s): James Engstrom, Chemical Engineering,
Cornell University, jre@cheme.cornell.edu

Mentor(s): Todd Schroeder, Paul Ma, Chemical Engineering,
Cornell University, tws11@cornell.edu, pfm12@cornell.edu

Abstract:

The fabrication of three-five semiconductors on silicon wafers has been a goal of industry for the past few years because of the optical properties of the semiconductors which can be used for many computer applications, and because silicon is the industry standard for computers. Combining the silicon wafers and the semiconductors is the most practical way to introduce the benefits of these semiconductors to the computer industry.

This summer we explored ways of accommodating the lattice mismatch between gallium phosphide and silicon. The two crystals do not line up, and the resulting strain eliminates the most useful properties of gallium phosphide: a III-IV semiconductor. The method we used this summer involved the fabrication of an array of microtips on a silicon wafer. These tips served to accommodate the lattice strain by pushing the strain onto the silicon. Once the correct specifications were determined for the tips, the final array of tips was created, and later gallium phosphide will be deposited using a form of chemical vapor deposition.

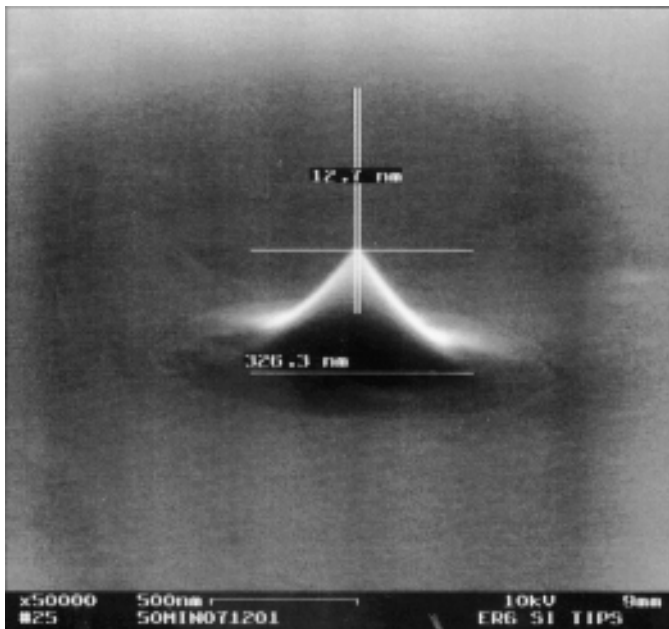


Figure 1: Fabricated silicon tip.

Process:

The focus of my project was to fabricate and analyze the tips before they were inserted in the deposition machine. It is very important that the tips be sufficiently sharp, so the gallium phosphide does not strain and lose its properties. We created the tips with a series of oxidations in the chemical hood. We started with the pattern generator and created small boxes on the wafer, then etched them down and oxidized them to form the correct shape. The correct form of the tips involved many layers of different materials to support the tips, however, the layers of material could not be involved in the characterization under the scanning electron microscope (SEM), so the fabrication process had to be stopped in the middle for characterization. After the most basic part of the tips were formed, they still had a layer of thermal oxide which was removed with hydrofluoric acid. Once the layer was removed, the tips were moved to the SEM for characterization.

We used the SEM to characterize the tips and determine the correct oxidation times. The initial array of tips was a test wafer with several variables that could affect the tip shape. Oxidation time, size of array, tip width, and distance between the tips were the variables we studied. The characterization was done using settings of ten volts and a 75 degree tilt. The goal of characterization was to find a set of variables that produced tips that were as high as possible with a tip radius of less than thirty nanometers.

The problems with the tips were that they either spent too much time being oxidized, or they did not spend enough time being oxidized. The tips that were over oxidized were extremely short or nonexistent. Every tip began at a height of 0.7 μm , however the tips that were over oxidized ended up at heights of approximately .35 μm . Another difficulty was tips that instead of having a width of thirty nanometers or less had widths of several hundred nanometers. These tips needed to spend more time being oxidized. The three oxidation times we experimented with were fifty minutes, seventy minutes, and ninety minutes. The tips that were oxidized for ninety minutes almost completely disappeared, while all of the tips that were oxidized for fifty minutes were extremely wide. The seventy-minute tips showed a

significant amount of promise. While the .8 μm tips and the .6 μm tips were both over oxidized, the 1 μm tips were nearly perfect. Therefore, our goal was almost reached. However more experimentation is needed to focus in on the precise variables.

The second problem we dealt with in our project was the fabrication of the final array of tips. The tips need to be densely packed, and the limits of the pattern generator interfered with the creation of an array of tips made from cylinders. The pattern generator operates by creating rectangles. We needed eight rectangles to make each circle, which was a problem because the time it takes to make many circles is prohibitive to the project. Instead, eight rectangles, or flashes can be used to make nine squares, which is what we did. The square tips appear to have worked as well as the round ones did. The concern we had was whether or not the edges would be uniform, but the oxidations appear to have taken care of that concern. More experimentation is required to confirm this initial conclusion. With an array of square tips, we can pack them as densely as required for the project. This is useful because a more densely packed array of tips can accommodate more strain.

Results and Conclusions:

The conclusion of the project was that a tip radius of one micron is ideal for this project, and that an oxidation time of seventy to eighty minutes is ideal for the project. We also confirmed our original assumption that array size and the distance between the tips would have no effect on tip shape. Additionally, we discovered that using a square pattern on the computer aided design software is useful for cutting down the time on the pattern generator and making better tips.

Acknowledgements:

I'd like to thank Todd Schroeder and Paul Ma for all of their help, as well as the Cornell Nanofabrication staff. Also James Engstrom for his help.

Chemical Mechanical Polishing Characterization and Process Development

Ashley Harness, Chemical Engineering, Virginia Commonwealth University,
s2aeharn@mail2.vcu.edu

Principal Investigator(s): Daniel Woodie, Cornell Nanofabrication Facility,
Cornell University, woodie@cnf.cornell.edu

Abstract:

Chemical mechanical polishing (CMP) is a current method used to planarize wafers, remove films, and construct damascene circuits. Characterization of the Strasbaugh 6EC instrument was performed at the Cornell Nanofabrication Facility (CNF). Three, four, and six-inch diameter silicon wafers with a thermal oxide film were studied. In addition, trenches were etched into three and four-inch diameter silicon wafers and polished. Film thickness and step height data were obtained in a specific pattern before and after polishing to provide removal rates and wafer uniformity.

The average removal rate increased with an increasing wafer diameter. Three and four-inch wafers ranged from 15% to 3% non-uniformity. Six-inch wafers consistently polished to a non-uniformity of 3%. Removal rates and wafer uniformity were affected by pad age, run order, pad conditioning, and carrier head ring attachment.

Introduction:

CMP has become a fundamental component in industrial semiconductor manufacturing since the development of copper damascene technology. High areas of wafer are removed while not affecting low areas, allowing the surfaces to become isotropic and planar. The chemical aspect of CMP involves slurry with nanoscopic particles suspended in an aqueous media. Slurries are designed for a specific type of wafer polishing, such as oxide, tungsten, or bare silicon. The slurry reacts to soften the wafer surface, thus assisting in substrate removal. Removal is achieved by the mechanical action of wafer friction against a polishing pad. Various types of polishing pads have been developed for changing degrees of removal, planarization, and polishing. Softer pads tend to deform around the features, removing less substrate and decreasing surface roughness and scratches. Harder and rigid pads will remove more material while sacrificing surface roughness. Pads contain pores and grooves designed to transport slurry across the pad surface evenly.

Experimental Procedure:

Carrier head extension was checked in three locations, directly above the bolts. The wafer should sit uniformly approximately 1/3 of the wafer thickness above the surface

of the carrier head. If the three measurements were not within the given range, appropriate thickness shims were added or removed from within the carrier head.

Three, four, and six-inch diameter wafers were used to study film CMP. Thermal silicon dioxide films were grown using chemical vapor deposition at the CNF by Daniel Woodie. The film thickness was obtained using a Prometrix FT-750 reflectometer at 29 positions on each wafer. After each wafer was polished, the FT-750 was used to measure the remaining film thickness at each previous location. All data were saved to a disk and Excel software was used for further analysis.

The final film thickness at each wafer position was subtracted from the corresponding initial film thickness to obtain the amount polished. This value divided by the number of minutes polished resulted in the removal rate. Standard deviation of film removed per wafer was found. Wafer percent non-uniformity was calculated by dividing the standard deviation by the average amount of film removed multiplied by 100. Uniformity and removal rates were plotted based on run order and pad age.

Trenches were etched into three and four-inch silicon wafers using photolithography techniques. Primer and photoresist were spun onto each wafer and baked. Exposure was performed with the EV620 contact mask aligner for 10 seconds. The mask was a grid of trenches 100 μm wide and 1 mm apart. Wafers were developed, post-exposure baked, wet etched, and residual resist stripped.

Trench step heights were determined using a Tencor P-10. The wafer was placed near the chuck center and vacuum was applied. Using software, the sensor was positioned on the center of the wafer. The wafer surface was scanned until a trench was found. The coordinates and the step height were recorded. A step height measurement was taken near the center of the wafer and in four cardinal directions. After polishing, the remaining step height was measured at approximately each original location. The same method for determining uniformity and removal rates was used.

Each wafer was polished using the parameter recipe developed by Strasbaugh for silicon oxide films. A diamond disk conditioning pad was run *in-situ* while polishing. Polishing wafers immediately after one another had an effect on the removal rate and uniformity. Variations were due to the temperature increase from pad friction. Three wafers

were polished with approximately 25-second intervals between cycles. The tool was allowed to return to its initial cold state. The carrier head rubber ring was removed to provide easier wafer balancing. Several more wafers were polished continuously in this manner. The tool was again allowed to cool down. One pad-conditioning sweep was performed using the diamond conditioning disk. Several other wafers were polished. The wafers were cleaned and dried.

Results and Conclusions:

Polishing characteristics of thermal silicon dioxide films were obtained. For three-inch diameter wafers, removing the carrier head improved non-uniformity from approximately 15% to 5%. Three-inch diameter wafers polishing rate was 1350Å/minute (A/min). Four-inch diameter wafers average polishing rate was 2050A/min while non-uniformity ranged from 3% to 11%. The average six-inch wafers polished at approximately 2400A/min. Six-inch wafers consistently polished to a non-uniformity of 3%. Figure 1 graphs average film removal rates by run order. Figure 2 graphs film percent non-uniformity by run order.

Silicon trenches were polished to determine removal rate and uniformity. Polishing three-inch diameter wafers removed 4740A/min. The non-uniformity ranged from 2% to 7%. Four-inch diameter wafers removed 6250A/min silicon with non-uniformity between 2-5%. Figure 3 graphs silicon trench average removal rates by run order. Figure 4 graphs silicon trench percent non-uniformity by run order. Bare silicon had a higher removal rate than thermal silicon dioxide films. The polishing slurry used for both wafer types contained potassium hydroxide, a known silicon etchant. The potassium hydroxide was likely reacting and softening the bare silicon surface more than film surfaces, making the mechanical CMP aspect easier.

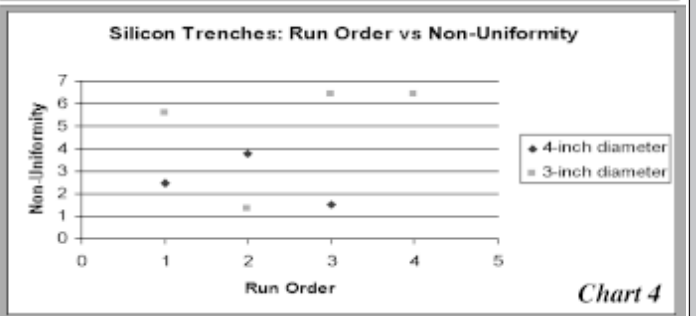
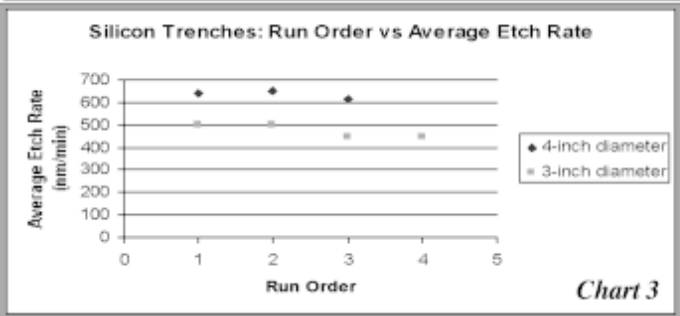
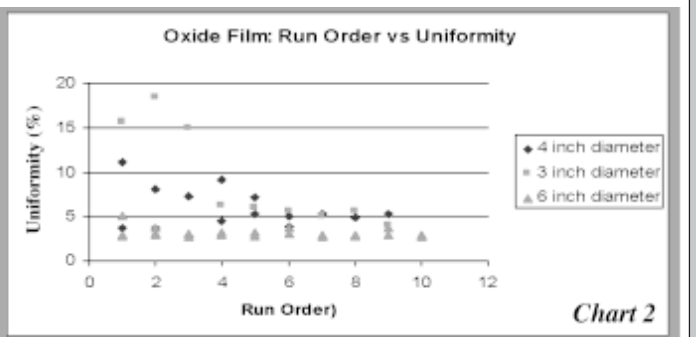
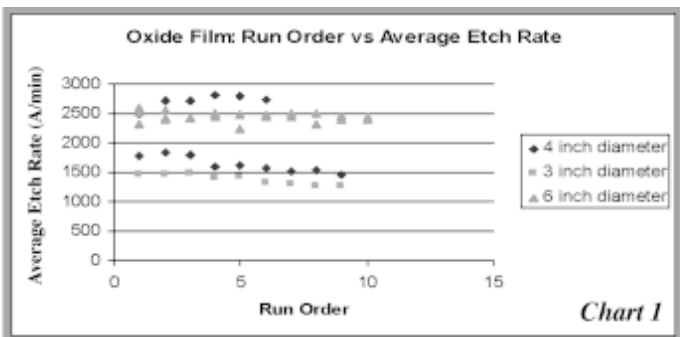
Removing the rubber carrier head ring had the greatest impact on three-inch diameter wafers. Removing the ring provided superior carrier head balancing by allowing all rings to rotate more freely. This additional rotation was needed due to the smaller surface area and less downward force during polishing. Removing the carrier head ring had no affect on either four or six-inch diameter wafers. All future three-inch wafers should be polished without the ring attached for improved results.

One pad-conditioning sweep with the diamond disk slightly improved the first wafer issues of poor uniformity and low removal rates. In addition, it is recommended for future users to first polish one dummy wafer to allow the system to achieve equilibrium. All other runs should be performed with little time between polishing cycles to maintain equilibrium and minimize first wafer effects. Increasing pad age had a slightly negative effect on polishing characteristics. Polishing pads at the CNF were most often replaced due to special polishing requirements, not old age.

Additional research should be performed to further characterize the Strasbaugh 6EC. The affects of changing slurry chemistry on one pad should be analyzed. Additional types of films (such as nitride) should be studied along with film variations due to growth in different chemical vapor deposition furnaces. Discrepancies between various wafer diameter removal rates could be attributed to improper machine calibration and warrants additional experimentation.

Acknowledgements:

Thank you to: PI Daniel Woodie, CNF, Cornell University, National Science Foundation, and fellow REUs.



Studies of Voids Formation in Silicon Induced by Silicon Surface Atoms Migration

Fatou Maiga, Chemical Engineering, North Carolina State University,
fgmaiga@hotmail.com

Principal Investigator(s): Michael Skvarla, Cornell Nanofabrication Facility,
Cornell University, Skvarla@cnf.cornell.edu

Abstract:

Large empty spaces below a silicon substrate can be formed by connecting single empty spaces or voids formed by the migration of silicon surface atoms. In this study, pores varying from 0.2 to 2 μm were created using Photolithography and Electron Beam Lithography. When the pores were etched and annealed in hydrogen ambient at a temperature of 1100°C and pressure of 10 torr, the silicon surface atoms migrated to minimize the surface energy, creating single empty spaces (voids). By rearranging the matrices of pores, the voids can be connected to form sub-surface channels which have applications in many areas such as fluid transport and sensor actuation. This technique is a promising method to form silicon-on-insulator (SOI) structures, one of the most desirable substrates for high speed, low power metal-oxide semiconductor devices.

The objective of this study is to characterize the void formation as a function of pore size, etched depth, and repeat spacing between the pores.

Introduction:

The proposed technique was derived from research done at Toshiba Corporation, Process and Manufacturing Engineering [1]. The transformation of patterned silicon

to extended spaces is based on the theory of surface-diffusion-dominated by a breakup model at high temperature. According to previous studies, Empty Spaces in Silicon (ESS) were formed by placing deep etched pores in a reducing environment at high temperature. By reducing the size of pores and/or the distance between the pores, sub-structures or extended areas were formed.

In this study, the concept of ESS and the procedure used to form ESS are presented, in which the surface-diffusion-dominated by break up model is used. Figure 1 taken from the early study illustrated the formation of ESS: in Figure 1(a), an isolated trench breaks up to empty space. The atoms at the curvature are smaller and denser than the top surface atoms. As the surface atoms diffuse along the surface plane, a tension is created between the top and bottom planes leading to necking; the necking persists until a break occurs. The number of empty spaces depends on the radius and the depth of the trench. In Figure 1(b), a row of etched pores combined to form a large void. As more trenches are created, larger empty space results as seen in Figure 1(c).

A design of pores of different sizes was created using Computer-Aided Design (CAD). The ESS process required a two level-exposure; therefore two masks were made. The first mask was used to create pores and the second mask was used for the analysis portion. Prior to the first exposure, the wafers were spun to form a 0.6 μm layer and pre-baked at 90°C for one minute. The first mask was used to create pores of 0.5-2 μm on the bare and oxide silicon wafers embedded in photoresist using a 10x i-line stepper. Smaller features of 0.2-0.4 μm were created using electron beam lithography. Figure 2 illustrates etched pores before the annealing.

The patterns on the bare silicon wafers were etched with the Plasma Therm 770 at a rate of 2 $\mu\text{m}/\text{min}$ using the resist as the mask. For the silicon oxide wafers, the oxide was etched with Plasma Therm 72; the wafers were then examined under the alpha step to check if all the oxide was etched; the resist was removed with GaSonic's Aura 1000 and the silicon portion was etched with the Plasma Therm 720.

The features were cleaned in acid and base baths, and annealed in hydrogen ambient from 10 minutes to 4 hours

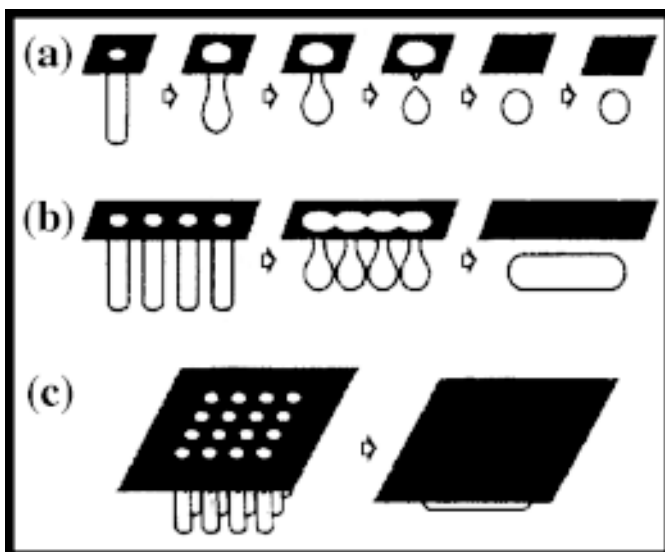


Figure 1: Illustration of ESS formation.

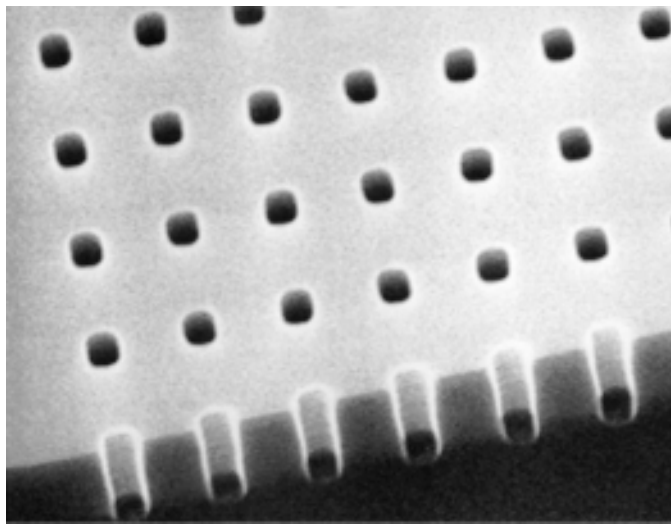


Figure 2: Etched pores before the annealing.

at a temperature of 1100°C and a pressure of 10 torr. After the annealing, the features were exposed to the second level exposure such that the original holes were revealed for analysis. The features were then examined under the scanning electron microscope.

Results and Conclusions:

Upon analysis the annealed pores showed a reduction in size, in agreement with the previous study. The formation of sub-surface channels or areas was not apparent; however, the trenches necked at several places, which could have led to the desired features if the conditions of the experiment were more appropriate.

Many factors may have hindered the formation of the ESS. (1) Oxide deposited on the trenches walls during etching may have remained during the analysis. The contaminants may have inhibited the movement of the surface atoms, or hidden any structure formed. (2) The technique is a multiple step process: an error in one step may have affected the remaining steps. (3) The temperature and the pressure of the furnace were not high enough to allow the formation of ESS.

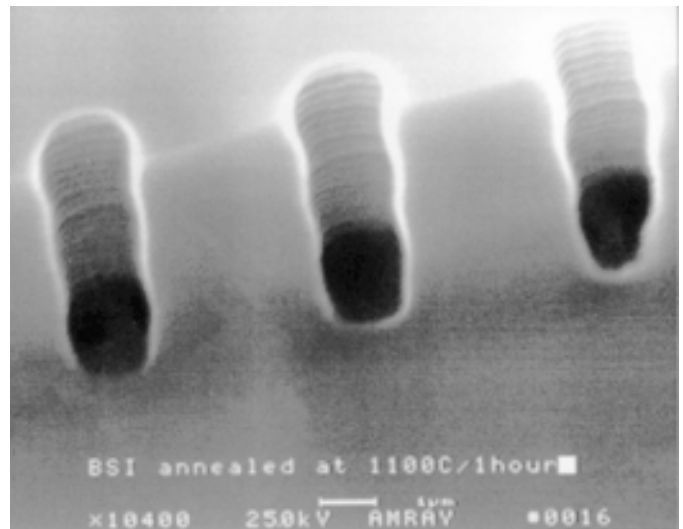


Figure 3: Bare silicon annealed at 1100°C for 1 hour.

Acknowledgements:

I would like to thank the National Science Foundation for funding this project. I extend my thanks to the National Nanofabrication Users Network and the Cornell Nanofabrication Facility for giving me the opportunity to gain experience in Nanotechnology. My special thanks to my principal investigator, Mike Skvarla, for his guidance in this project and to Wendi Maeda for providing the mask.

References:

- [1] Mizushima et al., Applied Physics Letters, V77, N20, p.3290-3292, 2000.
- [2] Sato, T. et al., IEDM, p.517-520, 1999.

Evaluation of Collagen as a Molecular Filtration Material

**Brian Manuel, Mechanical Engineering/Physics, Morehouse College,
brman70@hotmail.com**

*Principal Investigator(s): Dr. Michael G. Spencer, Electrical
Engineering, Cornell University, spencer@EE.cornell.edu*

Mentor(s): Hemant Benghale, Electrical Engineering, Cornell University

Abstract:

Experiments were conducted under the supervision of Dr. Michael Spencer, EE, at the Cornell Nanofabrication Facility to develop and execute a process to test collagen as a possible biological filter.

Introduction:

Collagen is formed from three long chains of amino acids that form a triple helix structure. Three of these triple helixes coil around each other to form a long structure called a fibril. These fibrils are about 300 nm long and about 1.5 nm in diameter. These fibrils are interwoven to form the collagen matrix which serves as a template for bone, cartilage, tendon, and skin cells to grow. Filtering, using collagen, and the successful patterning of a collagen structure has numerous biological applications. Some of them include replacement of degraded collagen matrices in teeth, skin, and cartilage as well as insertion of collagen filters in defective kidneys.

Procedure:

In this primary investigation of a bio-molecule used in nanofabrication, multiple layers of an aqueous solution of Type I collagen, derived from calfskin, were spun on 2% silicon wafers until the desired thickness of 80nm was achieved. The collagen layer was then placed in a .02% Gluteraldehyde solution. Gluteraldehyde is an enzyme created in the body that causes the collagen fibrils to bond together, forming a more stable collagen matrix. It was observed that Gluteraldehyde prevented the photolithography developer, 300 MIF solution, from reacting adversely with the collagen layer. Next photo-resist was then spun on top of the collagen layer. A bio-compatible, lactate-based resist, HPR-504, was used to minimize an unwanted reaction with the collagen layer. The resist was then patterned into a series of rectangular wells divided by walls varying in thickness from 2 μm up to 1300 μm .

Certain unforeseen setbacks did occur because the experiment was the primary investigation of the fabrication of a biomolecule. One such set back occurred in the development process of the resist layer. The resist used was intended to adhere to the silicon wafer and not to a biological substrate. Maintaining patterned resist

adhesion and structural integrity on the collagen surface became a problem. In the initial trials, the patterned resist layer was almost completely removed when shaken in developer solution. Other methods for removing the patterned resist such as varying the stirring speeds and repeated dipping were tested. Repeated dipping of the wafer at an angle into the developer solution aided in preventing the unexposed resist from rinsing away along with the exposed resist. Along with new development techniques, changes in the design of the pattern were made so that more of the resist was left unexposed which created more resist surface to adhere to the collagen layer.

The next step in preparing the wafers for filtration experiments was to create wells in the collagen layer of the same dimensions as the resist layer above it. To create these wells, wafers having collagen and patterned resist were etched using a 0.05% solution of collagenase, an enzyme in the body that dissolves the collagen matrix. Initial use of collagenase solution found that the rate at which collagenase dissolves collagen is extremely slow. The length of time that wafers were left in collagenase was gradually increased to achieve best dimensions of wells as possible. After two hours, the maximum time tested, collagenase was only able to dissolve 20 nm of the 80 nm thick collagen layer. A new initial filtration process was developed because of this time constraint. Instead of observing fluorescent tagged molecules flowing through collagen barriers of different thicknesses to determine the thickness of the barrier needed to stop the flow of 0.02 μm molecules, molecules were inserted into the wells in the resist layer and allowed to filter down and throughout the collagen layer. Dispersion of molecules was then observed using a special microscope modified to pick up the specific wavelengths of light emitted by the fluorescent molecules.

A directional dependence in the path of diffusion of the tagged molecules was observed. Molecules were observed to flow to wells only at a certain position on the wafers. It was hypothesized that the collagen fibrils were re-oriented during the spinning of the collagen solution onto the wafer in a spiral pattern creating nano-scopic channels only passing under certain wells in the resist layer. The molecules could therefore only migrate and be detected through those certain wells in the resist. In order to test this hypothesis, a new pattern in resist was

designed to better visualize an potential spiraling pattern. An octagon shaped well was surrounded by eight smaller square wells a varying distance of 100 to 1000 μm from each side of the center well. The tagged molecule solution was inserted into the center well and allowed to diffuse. The directional dependence was more easily observed. However not all trials resulted in the same data. There was one wafer that exhibited partial diffusion to a surrounding well other than those previously entered.

Results and Conclusion:

New techniques were created to aid in the preparation of wafers for filtration experiments. A possible directional dependence caused by spiraling fibrils was detected. However, diffusion of 0.02 μm molecules was obstructed by the collagen fibrils in other wells. In future experiments, more techniques for applying the collagen solution to the silicon wafer will have to be developed. Likewise, better methods to ensure resist's strong adhesion to collagen layer will have to be researched. Also, an increase in the pH of the collagenase enzyme may decrease time needed for wells to be created in collagen layer.

Acknowledgements:

Special thanks to:

Dr. Michael G. Spencer

Hemant Benghale

Michelle Stephens

Melanie-Claire Mallison

Mandy Esch

The Entire CNF Staff

National Science Foundation

Construction of Thin Optical Microcuvettes

**Meredith McElroy, Chemical Engineering, University of South Carolina,
meredithmcelroy@hotmail.com**

*Principal Investigator(s): Professor Andreas C. Albrecht,
Chemistry, Cornell University, aca7@cornell.edu*

Mentor(s): Peer Fischer, Ph.D., Chemistry, Cornell University, pf43@cornell.edu

Abstract:

A number of important nonlinear spectroscopies, such as sum-frequency generation and third-harmonic generation cannot be phase matched in normally dispersive liquids. If the chromophores in the solution show strong linear absorption, then it is necessary to use cuvettes with ultra short path lengths ($< 2 \mu\text{m}$) for these nonlinear spectroscopies.

There are two designs that have been pursued for the construction of the microcuvettes. A temporary structure was achieved by sputter deposition of $0.5 \mu\text{m}$ of aluminum onto a UV grade fused silica wafer. The liquid cell chamber was patterned by a piece of tape that was removed after the deposition, leaving a $0.5 \mu\text{m}$ well. This was then covered by another fused silica wafer which had holes drilled into it through the use of a sonic press.

A more permanent structure is a sealed cell in which a layer of silicon and silicon dioxide has been deposited onto a quartz wafer with plasma vapor deposition. The wafer with the deposition is then patterned using standard lithography techniques. Another wafer which has sonically drilled holes is then bonded to the first with an EV-501 bonding machine.

Introduction:

The specific aim of this project was to build microcuvettes for use in observing the chirality of molecules with nonlinear spectroscopy. In particular the cuvettes will be used to study a class of molecules known as Carotenoids. These are similar to the light receptor molecules in photosynthetic systems, and give fruits, vegetables and leaves their orange and yellow coloring. Since these molecules are colored, they strongly absorb visible light, and therefore cuvettes with very small pathlengths must be used. The planned experiments require cuvettes with pathlengths of between 0.5 to $2.0 \mu\text{m}$. In addition, the cuvette windows need to be transparent into the ultraviolet, the fluid needs to be channeled so that there are no air gaps, and the design should allow for multiple chambers. There were two experimental designs worked on this summer: an aluminum sputtered de-mountable cuvette and a sealed multi chamber cuvette.

Experimental Procedure:

For the aluminum sputtered de-mountable cuvette a 2 inch-diameter optical grade fused silica wafer, purchased from Chemglass, was cleaned with soap, water and a BetaWipe for 5 minutes. It was then dried with a nitrogen gun and masked off with tape in the shape of the desired chamber. Using CVC sputter deposition, $0.5 \mu\text{m}$ of 99.9% aluminum was sputtered onto the surface of the fused silica wafer. The masking tape was then removed. A second fused silica wafer was pre-drilled with 1.0 mm holes with the use of a sonic drilling press. These two wafers are held together with a mechanical press. Liquid is loaded into the cuvette by a dropper. The fluid is carried into the chamber through capillary action.

For the sealed multi-chamber cuvette, 3-inch diameter optical grade fused silica wafers (ChemGlass) were cleaned using the following procedures: 1) Soap, water and a Beta wipe for 5 minutes, 2) Soaked in H_2O , NH_3OH , H_2O_2 in a 5:1:1 mixture at 65°C for 10 minutes, rinsed in de-ionized water and dried with a nitrogen gun, 3) Polysilicon etch (Nitric Acid, H_2O , 40% HF in a 300:150:1 mixture) then rinsed with de-ionized water followed by cleaning process number 2 from above.

Following the cleaning process, $0.5 \mu\text{m}$ of amorphous silicon were deposited onto the substrate with the IPECVD machine. $0.3 \mu\text{m}$ of silicon dioxide were then deposited on top of the amorphous silicon. Standard lithography techniques were used to pattern the cuvette wells. The silicon and silicon dioxide were dry etched out of the wells with the PT72 machine. Hydroxyl groups were then attached to the surface using H_2O , NH_3OH , H_2O_2 in a 5:1:1 mixture at 65°C for 10 minutes. The patterned wafer and a pre-drilled wafer are then bonded together in the EV-501 bonding machine. Many different recipes were tried. The manufacturer recipe for bonding silicon dioxide to silicon dioxide is: 500N for 30 seconds at low vacuum and 30°C . Recipes tried included various forces from 500N to 5000N for 0.5 minutes to 1 hour at 30°C to 450°C , all at low vacuum.

Results and Conclusions:

Viable cuvettes were obtained with the aluminum de-mountable cuvette design. The measured well depths of these cells were approximately $0.8 \mu\text{m}$. A viable sealed

multi-chamber cuvette has not been achieved. Using the cleaning techniques 1 and 2, amorphous silicon immediately flaked off of the fused quartz substrate after removing it from the IPECVD. After cleaning the substrate with Polysilicon Etch, good adhesion was achieved. However, the Polysilicon Etch appears to leave surface abrasions on the substrate in a scratching pattern, which is believed to be caused by the polishing of the wafer by the manufacturer.

Permanent bonding of the patterned wafers has not been achieved. A recipe of 750N at 100°C at low vacuum was used to successfully bond two 3-inch un-patterned wafers that had been cleaned using cleaning procedure number 2. Duplicate attempts to bond patterned wafers were unsuccessful. Cleanliness and contamination are believed to be the primary problems impeding the desired results.

Development of Ultramicroelectrode Arrays for Microfluidic Biosensor Devices

Laura Moussa, Chemistry, Binghamton University, bh10309@binghamton.edu

Principal Investigator(s): Dr. Antje Baeumner, Biological and Environmental Engineering, Cornell University, abj23@cornell.edu

Mentor(s): Sylvia Kwakye, Biological and Environmental Engineering, Cornell University

Abstract:

The primary goal of this project is the customization of an interdigitated ultramicroelectrode array (IDUA) for use in pathogen biosensors. The IDUAs are made on three-inch diameter, one-millimeter thick glass wafers. To produce the IDUA, a layer of photoresist is patterned with a CAD design using the 5x g-line stepper. The pattern consists of two leads attached to a row of interdigitated "fingers" which form a channel for the substrate to flow through. The width of the fingers and the gaps are five μm . Following an image reversal process, the wafer is descummed and the electrode array patterned in platinum by evaporation, followed by lift-off in acetone. A thin layer (100 nm) of titanium between the Pt and the glass improves adhesion.

Fabricated wafers are then cut into individual electrode dies and tested for potential short circuits with a multimeter (i.e. resistance has to be $> 1\text{M}\Omega$). The percentage of working electrodes after cutting is approximately 20%. Sample chips are tested amperometrically with varying concentrations of ferri- and ferrocyanide.

Introduction:

Interdigitated electrode arrays are useful in the determination of pathogen concentration at the single cell level. Biosensors have 3 components, 1) the biorecognition element which identifies the analyte, 2) the transducer which measures the interaction between biorecognition element and analyte, and 3) the signal recorder which translates measured interaction into analyte concentration.

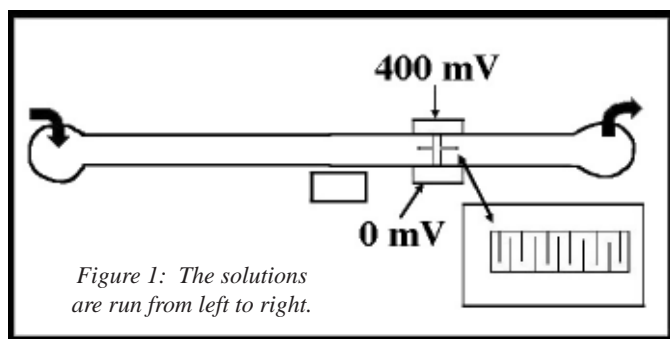


Figure 1: The solutions are run from left to right.

Figure 1 is the schematic for the general pathogen biosensor. The analyte and biorecognition elements are mixed and inserted into the first well. The biorecognition element consists of two sets of DNA probes able to specifically bind to the analyte (mRNA molecules from the pathogen). One set of DNA probes is immobilized on nanovesicles (liposomes entrapping electroactive molecules). The other set of probes is attached to magnetic beads. While flowing through the channel, analyte and probes mix and bind to each other. Complexes of beads, analyte and liposomes form. These complexes are captured on a magnet in proximity to an IDUA. All free liposomes will pass the magnet toward a waste well. Subsequently, a lysing solution is passed through the channel, breaking open the liposomes and releasing the entrapped electroactive compounds. A potential of 400 mV is applied across the two contact pads of the IDUA. The electroactive compounds are oxidized and reduced on the IDUA surface producing current. This current is directly proportional to the concentration of electroactive molecules contained in the nanovesicles. Since one nanovesicle can bind per target analyte, the concentration of electroactive molecules (and current) is directly proportional to the pathogen concentration in the sample.

Procedure:

The most important part of the process is cleaning the wafers thoroughly to allow for better adhesion of photoresist and metal onto the glass. The wafers were soaked in nanostrip for 2 hours before the process began. The wafers were vapor primed, also for better adhesion, by baking in the yield engineering systems vapor prime oven using HMDS primer. Positive photoresist (Shipley 1813) was spun onto the wafers at 2000 rpm for 30 seconds and then baked on a hot plate at 90°C for 2 minutes.

The pattern was transferred onto the wafers with a 5x g-line stepper from a mask previously prepared using CAD and a pattern generator. The exposure time was 1.06 seconds and the focus was 282. For image reversal, the wafers were exposed to NH_3 in the YES oven. Subsequently, the wafers were flood exposed for one minute to light using the 3HR contact/proximity mask

aligner, hardening the resist. The wafers were then developed in 321 MF developer for 2 minutes, rinsed with water, and dried. In order to remove photoresist residue, the wafers were descummed in the Plasma Therm 72 reactive ion etch. Descum typically ran for 1.5 to 2 minutes.

For optimal electrochemical properties, the IDUA electrodes were made with platinum. Titanium was evaporated as a first layer of 10 nm onto the wafers in order to improve platinum adhesion to the glass surface.

Platinum was evaporated to a height of 100 nm. For lift-off, the wafers were placed in acetone for 8-12 hours, then sonicated and rinsed. The wafers had to be cut into separate dies to be mounted into the biosensor microchannels. Using a diamond scribe rendered about 50% of the chips short-circuited, so instead a diamond-cutting wheel was employed to cut the wafers. However, even less IDUAs were intact after cutting. A better method must be found in the future.

Characterization was done optically using the microscopes at the CNF and a multimeter to test for resistance across the electrode. Also, sample chips were supposed to be tested amperometrically in order to determine a dose response curve for the electroactive compounds (potassium ferrihexacyanide and potassium hexa-ferrocyanide).

Results and Conclusions:

Twenty percent of the chips processed were confirmed as working using a multimeter. However, it proved to be difficult to test the small feature size IDUA with the laboratory's potentiostat. Therefore, no electrochemical characterization of the IDUAs was done. Figures 2, 3 and 4 are micrographs of complete electrodes on silicon wafers using the scanning electron microscope. In figure 2, the fingers are contained in the cross bar. The solution would flow through this channel to create the signal. Figure 3 shows the electrode fingers.

Future work would include the insulation the IDUAs using polyimide in the lithography room before dicing the wafers, allowing electrochemical analysis in the laboratory. Also, electrodes with smaller gap sizes should be designed to increase the electrochemical signals and signal to noise ratio.

Acknowledgements:

Thanks to the following groups for funding and support:

- National Science Foundation
- The Cornell Nanofabrication Facility and Staff
- The Antje Baeumner Research Group, especially Sylvia Kwakye and Jun Hong Min

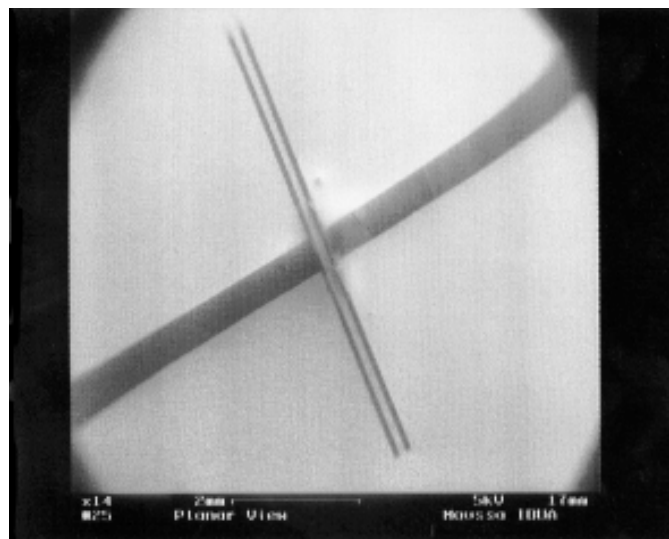


Figure 2. 14x magnification of an IDUA.

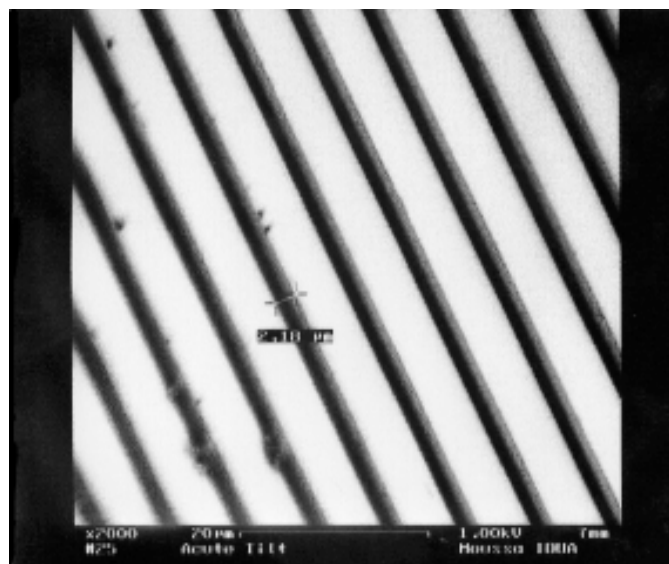


Figure 3. 700x magnification of an IDUA.

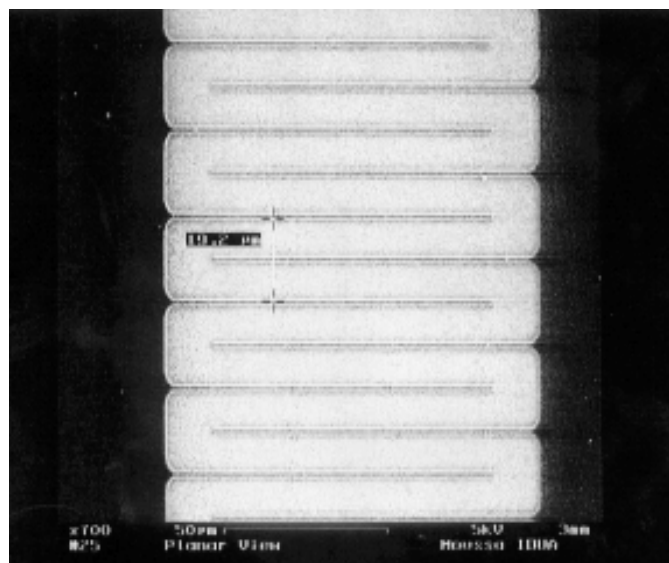


Figure 4. 7000x magnification of electrode in photoresist.

Processing of Next Generation Resist Materials using Supercritical CO₂

G. Nagesh Rao, Mat Sci&Engr/Phil, Rensselaer Polytechnic Institute, raona@rpi.edu

Principal Investigator(s): Dr. Christopher Ober, Mat Sci&Engr,
Cornell University, Cober@ccmr.cornell.edu

Mentor(s): Victor Q. Pham, Chemical Engr, Cornell University, Vqp2@cornell.edu

Abstract:

Supercritical CO₂ (SC CO₂) has become an important medium of fluids technology for environmentally benign semiconductor processing. The solvent has received attention for processing and cleaning abilities of various photoresist materials, specifically chemically amplified fluorinated photoresists. Some resist materials were designed for next generation 157 nm photolithography, and have the potential to be developed in a nontoxic environment and reduce hazardous chemical waste. The focus of the project was divided into three main areas. (1) Studying development of THP-(r)-F7MA photoresists with and without a Au/Pd substrate coating for optimal processing and sample preparation conditions for other photoresists dissolved by SC CO₂. (2) Development of a chemical process to convert negative toned resists into positive toned resists, through Diffusion Enhanced Silylated Resist (DESIRE). (3) Using a Dissolution Rate Monitor (DRM) to study polymer film thickness changes within a SC CO₂ medium. The behavior of this curve depends on polymer dissolution rate and extent. It is expected to see an approximate sinusoidal curve when processing conditions were ideal. Photoresist processing and characterization included a SC CO₂ film development chamber, SEM, and AFM. Results obtained included feature sizes of sub-micron width on THP-(r)-F7MA photoresist, creation of DESIRE processing apparatus, and fractional sinusoidal curves for an arbitrary block co-polymer film.

Introduction:

To understand the engineering and science of these new technological regimes, a multi-faceted research project is required to gain a more in depth knowledge of the study. With the development of general fluoropolymers in microelectronic fabrication, it usually requires an arduous chemical process. Their specific polymeric nature requires a lot of time and energy, as well creates significant chemical waste. Substituting a more benign process for these polymers is desirable. Thus the innovation of using SC CO₂ to chemically process certain types of fluoropolymers that can be environmentally friendly and useful in the development of these major-scaled photoresists for 157 nm lithography. Since both SC CO₂ and many fluoropolymers are characterized as being non-polar, the basic chemistry "Likes Dissolve in Likes" can be applied.

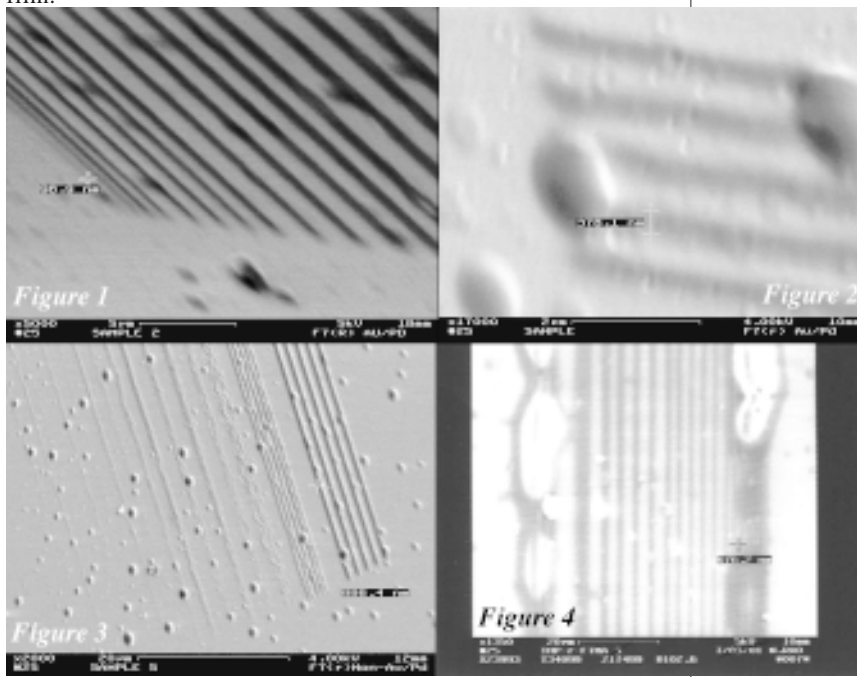
A more general fact about SC CO₂ is that it is a great benign chemical to use as a cleaning agent for various portions of semiconductor processing. With these creative ideas of utilizing supercritical fluids technology in the microelectronic industry, new tools, metrics, and standard characterization procedures need to be developed and implemented to better understand optimal conditions for ideal candidates. The goals for understanding the advantages of SC CO₂ research for next generation photoresists was split into the three main areas previously described.

Experimental Procedures:

For research area number one, the main idea was to see how much of an effective measure the Au/Pd could provide in protecting the THP-(r)-F7MA polymeric films during the patterning exercises of E-beam lithography. Following the lithography sessions would be the SC CO₂ development and then SEM and AFM characterization to study the various E-beamed dosages patterned in sets of right-angled lines to help determine what the right conditions are necessary to obtain sub-micron features within the developed photoresists.

These patterns of lines consisted of

Figure 1: Processed for 3 minutes at a constant pressure of 4500 PSIG's and temperature of 45°C. We see a line relatively close to .098 μm. Figure 2: Processed for 5 minutes at a constant pressure of 4,900 PSIG's, 45°C, and an open flow rate of 66 LPM CO₂. We see .378 μm width lines. Figure 3: Processed for 5 minutes at a constant pressure of 4,900 PSIG's 45°C, and an open flow rate of 66 LPM CO₂. We see .886 μm width lines. Figure 4: Another example of poor feature quality between the polymer resist lines.



smaller lines that made up their pattern. Through this technique, it could be determined what pressures and temperature were required for the SC CO₂ to properly dissolve the polymer films down to the smallest lined features. The theory was to maintain a constant temperature of around 45°C, and vary the solvating pressure between 4000 and 5000 PSIG's with an open continuous constant flow of the supercritical solvent along the polymer film. There were a lot of processing parameters to keep in mind when trying to determine the most ideal conditions for the film's development.

The next area of work was to figure out a method of converting our resists, which are negative toned, into a positive tone material. The concept can be denoted along the lines of an Image Reversal Process. Hexamethyldisilazane (HMDS), commonly used as an adhesive primer between typical resists and the silicon substrate, can remove hydroxyl side groups from certain types of fluoropolymers that would be inhibited in complete thorough processing in SC CO₂. The process implemented for this area of study was the following: Begin with spin-coating the film onto the Si wafer, followed by an Ultraviolet Exposure. Then a very much necessary Post Exposure Bake at 90°C to release the PAG's (photo-acid generators) within the film. HMDS in a vapor form would be introduced onto the film surface for removal of the hydroxyl-groups. Then the film can be processed in SC CO₂ to remove unexposed UV-areas of the film. Finally the entire film sample would be treated with a UV flood-exposure resulting in the positive toned photoresist.

The final facet of work done this summer with respect to studies of SC CO₂ and polymer film development, was the continued implementation and promotion to use the DRM to create an analytical metric which proves ideal conditions are being met in the dissolution of the polymer film in the SC CO₂. Arbitrary polymer films will be spin-coated onto the silicon substrate, and then broken into small pieces to individually fit into the processing vessel. One small piece will be placed in such way that the HeNe laser can shine through a quartz window onto the film surface so that the film's specific refractive intensity beam can be picked up by the intensity meter. Usually a minimum initial value of around .5 intensity was satisfactory for study. The change in the intensity readings are then monitored through Data Logger software, as the SC CO₂ flows over the thin film to dissolve the material. If conditions are ideal for the specific polymer's processing conditions, then a sinusoidal curve of some form will be translated from the change intensity readings and displayed on the computer program.

Results and Conclusions:

From project 1, it can be seen as advantageous to use the Au/Pd coating in protect the THP-(r)-F7MA polymer film from the intense energy of electrons from the E-beam lithography. Samples not coated clearly displayed stresses along the patterned lines of the polymer material. Or, if not stresses, definitely polymeric degradation and sometimes fusing between the patterned polymer lines. Also noted for optimal processing was that at medium to lower solvent pressures of around 4,000 to 4,500 PSIG's, at a temperature of 45°C, and a constant open flow of SC CO₂ for 3-5 minutes provided very good development of the E-beamed polymer film. From sub-micron feature sizes of 0.378 to relatively 0.1 μm width lines were confirmed under SEM and AFM imaging. Although ideally, feature sizes below .1 μm width could be obtained by even

more precise processing conditions. Attached results below with subheadings indicate the progress and capabilities SC CO₂ has for environmentally friendly photoresists.

It was concluded in the DESIRE project that HMDS would possibly serve very well as a reagent to convert our negative toned resists into positive toned resists. However the present method of applying the HMDS vapor onto the polymer film, in this case a THP-(b)-F7MA, was not effective enough. To guarantee whether or not the image reversal process technique can be accomplished, an apparatus to apply the chemical was mullied over with various designs. A suitable setup was decided upon and created with the help of the Chemistry Glassblower, but not in time for further analysis of the research before the term had ended.

The DRM setup as stated before was a continued study to develop a tool to analyze thin film rate dissolution in SC CO₂. The major results of this study included some semi-sinusoidal curves for a type of co-block polymer film. Mainly the understanding of the purpose behind the metric was important to learn and utilize. The experimental setup can be seen in the attached figures, labeled DRM schematic which describes the logistics.

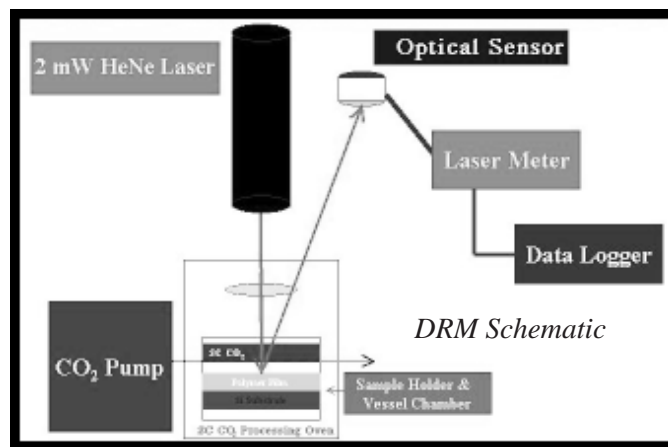
Through these various projects, a more fundamental understanding of the many uses of SC CO₂ and its important benefits, furthered the development of next generation photoresists which can be cost-effective and environmentally benign in the microelectronic industry.

Future Work Includes:

Work on developing better conditions for SC CO₂ exposure on the photoresists. Attempt to produce smaller feature sizes on the order of .09 μm and below. Use the apparatus for the DESIRE studies and learn more about the use of HMDS for imaging reversal of fluoropolymers developed in the SC CO₂ medium. Finally, continue DRM film studies to develop a tool/metric standard for SC CO₂ dissolution of polymer films. In essence, apply and understand the use of the sinusoidal curves in determining "Ideal Film Processing Conditions".

References:

- [1] F. Rodriguez, P.D. Krasicky, R.J. Groele. Dissolution Rate Measurements. Solid State Technology, May 1985, 125-131.
- [2] Ober, C. et al. Current Research on SCF CO₂ Technology at Cornell University, Materials Science and Engineering, Bard Hall.
- [3] Ober, C.; Pham, V.; Rao, G.N. NSF/SRC/ERC Environmentally Benign Semiconductor Manufacturing Semi-Annual IAB Meeting at Stanford, Palo Alto, C.A.. "Studies of Polymers in Supercritical CO₂ (Dissolution Rate Monitoring System)" (August 2000).



Process Characterization of LPCVD Silicon Nitride and the Consequential Fabrication of Low Stress Microcantilevers

Gregory T. Roman, Chemistry, Bard College, gr833@bard.edu

Principal Investigator: Daniel Woodie, CNF, Cornell University, woodie@cnf.cornell.edu

Abstract:

Low Pressure Chemical Vapor Deposition (LPCVD) of silicon nitride (Si_3N_4) is an important process in the construction of micromachined devices that depend upon low stress thin films. This paper presents a logical method for modifying the deposition parameters of a hot wall type reactor to obtain desired stress levels for use in micromachined devices. The primary parameters of investigation are: total gas flow of dichloro silane (DCS) and ammonia, gas chamber pressure, and the gas ratio of DCS to ammonia. At a fixed point inside the reactor, these parameters were found to have significant effects on the thin film that was formed. We found that by varying one or more of the specified variables that we could lower the stress of our Si_3N_4 film to $1.4 \pm 11\text{MPa}$. Trends for each of the adjustment parameters were identified and explained. The results of this optimization process allowed us to form a low stress film for the construction of microcantilevers.

Introduction:

Silicon nitride is a popular ceramic material that can be used in the fabrication of many different devices. A popular way to deposit silicon nitride is by low pressure chemical vapor deposition (LPCVD) using an ASM hot wall reactor. The process depends upon four critical parameters which are the total flow rate of the gasses, gas ratio of ammonia and DCS, chamber pressure, and chamber temperature. All of these quantities are explored in previous papers [1, 2], but they do not fully correlate

the results with an overall view of the chemistry and gas mechanics of the chamber itself.

The most significant factor in the LPCVD silicon nitride furnace is the gas ratio. By modifying the ratio at which ammonia and DCS enter the gas chamber one can drastically change the film properties obtained at a specified point within the chamber by several hundreds of MPa. Rough optimization of this parameter can be achieved through analyzing previous literature [1]. Other secondary factors are pressure, boat location, and total flow rates; all of which have direct implications on the stress of the film, and were extensively investigated.

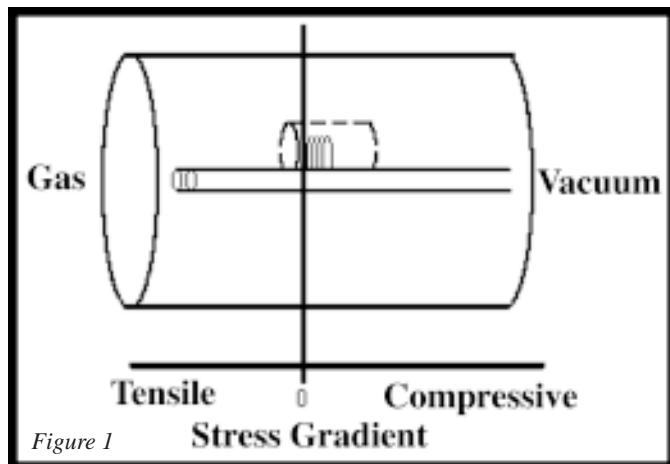
Methods and Materials:

We used an ASM hot wall 9 inch diameter LPCVD furnace for all silicon nitride depositions. Stress measurements of the silicon nitride thin films were performed with laser interferometry (Flexus 750), and reactive ion etching (Plasma Therm 72) to etch off one side of the wafer. Typical standard deviations were significantly lower than previous literature due to use of double-sided and single-sided polished silicon wafers.

Results and Discussion:

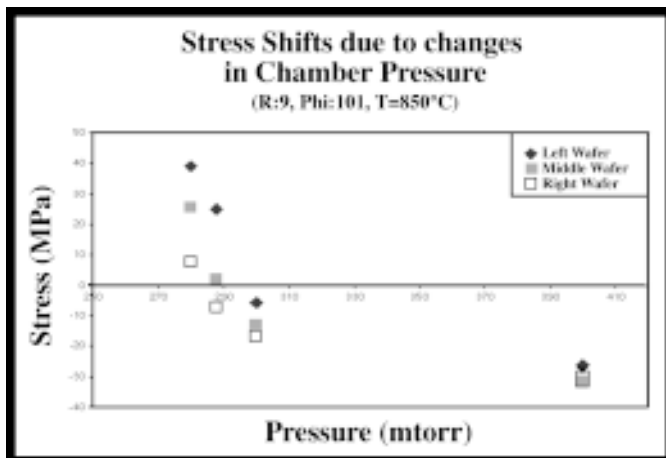
The trends that were seen can be summarized into a very simple paradigm. Consider the idea that there are different reactions occurring at every different point in the furnace. These different reactions deposit different molecules at different rates. So in the end, you will obtain different stresses for every single point inside the furnace. Changing the reactions that occur through the tube are most heavily affected by the gas ratio of DCS to NH_3 . Other variables like pressure and total gas flow also have substantial effects on the stress of the film, but are secondary to that of the gas ratio.

The underlying reason why the gas ratio affects the LPCVD deposition chamber the most is because it has the greatest effect on what is being deposited at different points in the chamber. By increasing the amount of ammonia that is in the chamber, the film stress becomes increasingly tensile, whereas, decrease the amount of ammonia in the chamber and the stress of the film in the chamber becomes increasingly compressive. By balancing these two extremes, one can create a point in the chamber



that closely approximates zero stress. As seen in Figure 1, this zero stress has a gradient of tensile stress that increases towards the gas inlet, and also has a gradient of compressive stress that increases towards the vacuum inlet.

These stress gradients can be moved in the chamber by changing the pressure and the total flow. By increasing the pressure of the chamber, the extents of reaction are not allowed to move as far down the chamber (towards the vacuum). So by increasing the pressure of the chamber for a fixed gas ratio, total flow and temperature, the resulting film will become more compressive. On the other hand, if you decrease the pressure within the chamber, the extents of reaction will migrate further down the chamber and resulting thin films will be more tensile. A similar relationship is involved with the total flow rate of the furnace. By increasing the total flow you can push the reactions further down the chamber (with high flow rates) or keep them confined to the point of entry (with low flow rates). By increasing the flow rates, the film will be more tensile, and by decreasing the flow rates, the film will be more compressive.



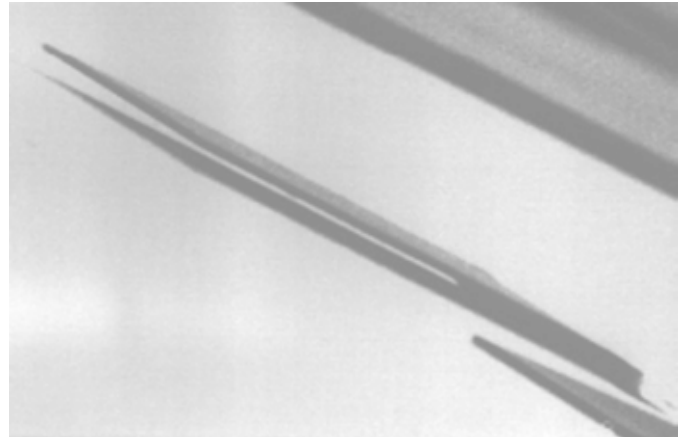
By optimizing the stress of the film, we were able to construct very low stress microcantilevers. The primary function of these microcantilevers was to determine the existence of a differential stress in the film. If there was a differential stress in the film, the microcantilever would either curl up or down. We found that by holding the pressure constant in a closed loop program for a silicon nitride deposition, we could eliminate differential stresses in the resulting thin films. The resulting cantilevers were perfectly flat.

Acknowledgements:

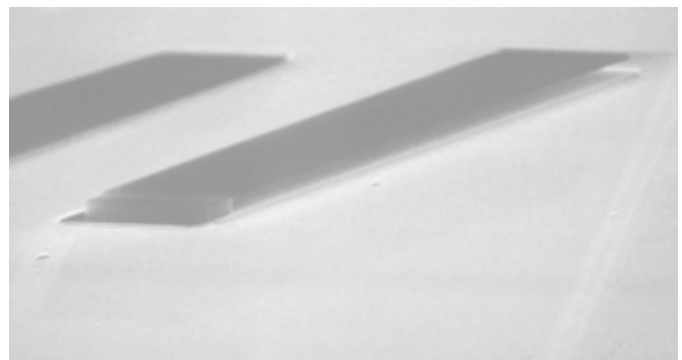
I thankfully acknowledge Dan Woodie, Phil Infante, Melanie-Claire Mallison, and NSF.

References:

- [1] Gardeniers, Tilmans, Visser. LPCVD silicon-rich silicon nitride films for applications in micro-mechanics, studies with statistical experimental design.



SEM examples of flat cantilevers



**Materials Science Research Center of Excellence
Howard University, Washington, D.C.
<http://www.msrce.howard.edu/~nanonet/NNUN.HTM>**

2001 REU Interns



REU Intern School Affiliation Principal Investigator

From L to R:

Ms. Yvette Williams	MSRCE, Howard University	Howard REU Coordinator
Mr. Court Wilson	Trinity College / Duke Univ	Gary Harris and Kimberly Jones
Ms. Unyime Eshiet	Temple University	Gary Harris and Peizhen Zhou
Mr. Robert Klein	UCSB	Gary Harris
Mr. Julio Bracero Rodriguez	University of PR Mayaguez	Gary Harris and Mamadou Diallo
Mr. Gary Harris	MSRCE, Howard University	Howard NNUN Director & REU PI

Characterization of Peptide Sorption onto GaAs (100) Surfaces by AFM, Optical Microscopy and FT-IR Spectroscopy

Julio Bracero Rodríguez, Biology, University of Puerto Rico, Mayagü Campus

Principal Investigator(s): Dr. Gary Harris, EE, Dr. Mamadou Diallo, Civil Eng and Chemistry, Howard University, gharris@msrce.howard.edu, diallo@wag.caltech.edu

Mentor(s): James Griffin, Howard University

Abstract:

The characterization of peptide sorption onto semiconductor surfaces such as GaAs, Si and SiC is of critical importance to the development of novel hybrid organic-inorganic nanoscale devices for molecular electronics.

This project focuses on the characterization of peptide sorption onto GaAs (100) surfaces. The first phase of the project consisted of exposing GaAs crystals to aqueous solutions of two model peptides, G1-3 and G12-3, buffered with Tris at pH = 7.8. We exposed the surfaces to the peptide solutions for 16 hours with and without a continuous nitrogen gas flow. The surfaces were also exposed to a Tris-buffered saline (TBS) solution as a control. We then searched for peptide binding on the GaAs (100) surfaces using atomic force microscopy (AFM) and optical microscopy. Findings using both AFM and optical microscopy showed various patterns on the surface of the semiconductor that suggest possible peptide binding. The use of Fourier Transform-Infrared (FT-IR) spectroscopy on the surfaces revealed an absorption spectra that suggests the presence of various of the peptide functional groups.

Introduction:

Researchers in the University of Texas, Austin, have found that peptides can bind selectively to various semiconductor surfaces, such as Si, GaAs and InP. The nature of the peptide binding, be it physical, chemical or

electrical, is still unknown and is an area of intense research. In this experiment, we attempt to characterize the peptide binding in GaAs (100) surfaces by various methods, such as AFM, optical microscopy and Fourier Transform-Infrared Spectroscopy.

Procedure:

We selected the peptides G1-3, which contains the amino acids: R L E L A I P L Q G S G, and G12-3, which contains the amino acids: A Q N P S D N N T H T H, and used GaAs (100) as our semiconductor surface. The peptides were tagged with the fluorescent molecule marker C-1311, molecular formula $C_{25}H_{15}NO_9$, with an absorption wavelength of 494 nanometers. We prepared two peptide solutions in a Tris-buffered saline solution, mixing 1mg of the peptide in 50mL of Tris buffer at pH = 7.8. The GaAs (100) crystals had dimensions of 1 cm x 1 cm and were washed with acetone and methanol, rinsed with water and then introduced to an etching solution of HCl:H₂O 1:1, then rinsed again with water.

A. Surface Exposure:

Once the surfaces were properly cleaned, we exposed the surfaces to each peptide solution for 16 hours with two different setups: with and without a continuous nitrogen flow. The main purpose in doing so was to prevent an oxide layer from forming on the surface. In order to maintain a continuous nitrogen flow for the given amount of time, a stainless steel wire was coiled and connected to a nitrogen tank. After the exposure, the surfaces were blown dry without rinsing. At first, we rinsed with water, but we didn't find any formations on the surfaces at this concentration. Only when we stopped rinsing the surfaces did we find any formations.

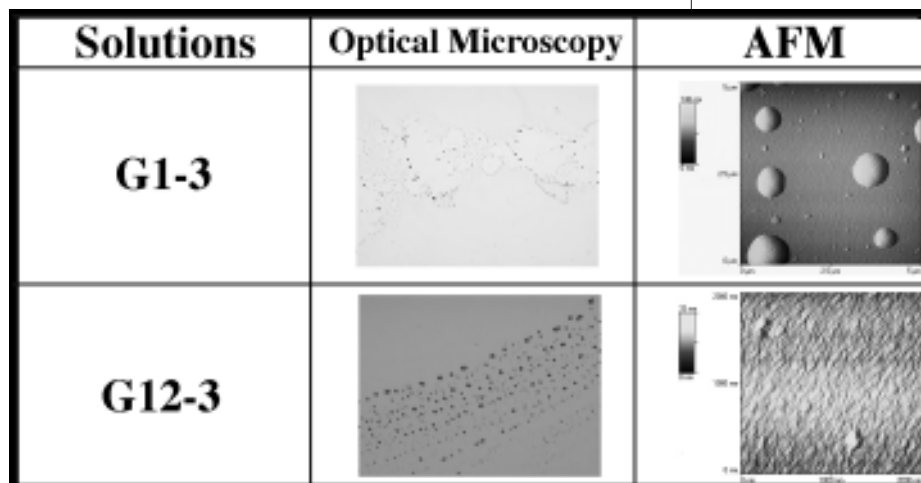


Figure 1, Left: GaAs (100) Surfaces under Optical Microscopy

B. Surface Analysis with AFM and Optical Microscopy:

We only found formations on the surfaces that were exposed to a continuous nitrogen flow. The samples appeared violet when analyzed with the optical microscope which corresponds with the wavelength of the fluorescent marker. Please see figure 1. We also found some patterns using AFM. Please see figure 1.

C. FT-IR Analysis:

The analysis revealed marked absorbance peaks in various regions which correspond to some of the peptides' functional groups: bands in the 3500-3000 cm^{-1} range suggests the presence of O-H and N-H stretches; bands around 3000-2800 cm^{-1} suggest the presence of alkenes or C-H stretches; bands in the 1250-1000 cm^{-1} region suggest the presence of amine groups, or C-N and C-N-C stretches, which is the basic backbone of proteins. Please see figure 2.

Conclusions and Discussion:

This investigation focused on the characterization of peptide sorption onto GaAs (100) crystals using AFM, optical microscopy and FT-IR. We found formations and identified them with the tagged fluorescent marker using the optical microscope, plus we found some patterns using AFM. The FT-IR spectra provided us with some data that strongly suggests the presence of peptide layers on the surface.

The G1-3 and G12-3 peptides have 4 and 10 amino acids respectively, with functional groups (Arg, Glu, Gln and Gly / Arg, Leu, Glu, Ile, Gln, Gly and Ser) that can

donate electrons to the GaAs surface. We propose a model of peptide binding in which the interaction between Lewis bases on the peptides and Lewis-acids sites on the GaAs surface may mediate the selective binding between the two model peptides and the GaAs crystals.

Future investigations will involve more analysis using other techniques and designing a computer model of peptide-peptide and peptide-substrate interactions.

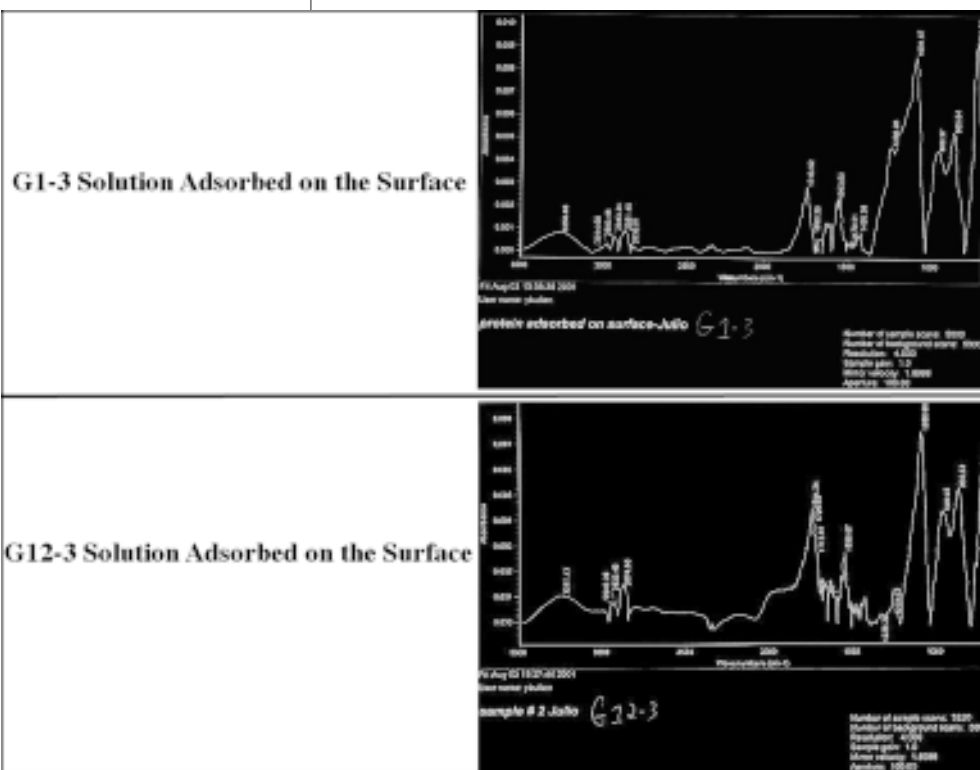
Acknowledgments:

I would like to thank Dr. Mamadou Diallo, James Griffin, Yemi Bullen of the Chemistry Department, Simone Christie of the Civil Engineering Department, and Dr. Gary Harris, Yvette Williams and the rest of the MSRCE staff, for a productive and unforgettable summer.

References:

- [1] Whaley, Sandra R., Hu, Evelyn L., Barbara, Paul F., Belcher, Angela M. "Selection of Peptides with Semiconductor Binding Specificity for Directed Nanocrystal Assembly"; Nature, Vol. 405:665-668, June 2000.
- [2] Benaki DC, Aggeli A, Chryssikos GD, Yiannopoulos YD, Kamitsos EI, Brumley E, Case ST, Boden N, Hamdrakas SJ. " and FT-IR Spectroscopic Studies of Peptide-Analogues of Silkmoth Chorion Protein Segments"; Int J Biol Macromol, 23 (1):49-59, July 1998.
- [3] Allivisatos, A.P. "Organization of Nanocrystal Molecules Using DNA"; Nature, Vol. 382: 609-611, 1996.

Figure 2, Right: FT-IR Analysis of GaAs (100) Surfaces.



The Growth and Characterization Processes of Gallium Nitride (GaN) Nanowires

Unyime Eshiet, Electrical & Computer Engineering, Temple University

Principal Investigator(s): Gary Harris, PhD., PE., Dr. Peizhen Zhou,
MSRCE, Howard University, gharris@howard.edu

Abstract:

Gallium nitride (GaN) semiconductor nanowires were grown and fabricated to show its possible use in making quantum devices. The ability to grow and use nanowires in making quantum devices such as lasers, light detectors, diodes and transistors offers great promise for the future of science and technology. GaN nanowires were grown by reacting 3g of gallium metal with ammonia gas flowing at 100 sccm in a quartz liner inside a tube oven at 900°C for 4 hours in a vacuum system at 15 Torr pressure.

The characterization process involved categorizing the physical and the electrical properties of the nanowires. The physical properties of the nanowires were determined using the optical microscope and the scanning electron microscope. Some nanowires were found to be uniform, short and straight and others were found to be curvy, long and non-uniform. The electrical properties (I-V characteristic) of the nanowires were tested by extracting individual nanowire and placing it on an insulated copper circuit board with tweezers and securing a fixed position with conductive silver epoxy, and then testing its conductivity with a programmable curve tracer. Photoluminescence was done to test and determine the band gap of the GaN nanowires and it was found to be 3.4 electron volts.

Introduction:

Gallium nitride nanowires were grown by reacting gallium metal with ammonia gas through a vapor phase deposition process. There are 3 stages by which GaN nanowires are formed. Figure 1a shows the setup apparatus for this experiment. Figure 1b shows the different stages and NH₃ flow rate vs. temperature, and Figure 1c shows the growth stages. At first an amorphous GaN matrix is formed and then followed by polycrystalline hillocks, and then finally the nanowires form from the edges of the crystal or hillocks. The characterization processes of GaN nanowires involved categorizing the physical and the electrical properties of GaN nanowires. The electrical (I-V) characterization was performed using the programmable curve tracer and the physical characterization was performed

using the optical microscope, scanning electron microscope and the UV beam emitter by the process of photoluminescence. GaN nanowires were successfully grown and characterized during this experiment.

Gallium Nitride (GaN) is a semiconductor material that has many benefits in the fabrication of quantum devices because of its high melting temperature property which helps in the fabrication of high temperature electronic devices, and its ability to be light sensitive which helps in the fabrication of light detectors, and light emitters. Also, gallium nitride is also known to have a large band gap compared to other materials. GaN material is chosen over carbon because it is known to be a semiconductor material at all times whereas carbon nanowires are sometimes semi-conducting, conducting or non-conducting depending on the chirality of the material. This report covers how the GaN nanowires were grown and the procedures that were followed in order to characterize them.

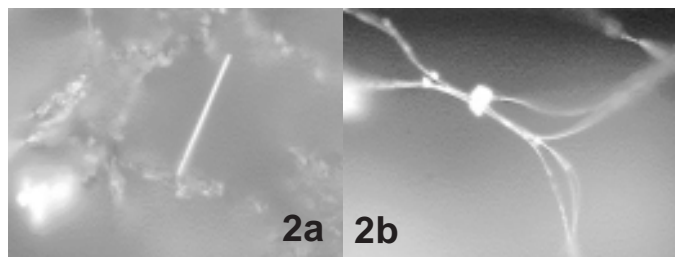
Experiment:

GaN nanowires were grown catalyst free in a vacuum system by reaction of gallium metal vapor with ammonia gas. The boron nitride (BN) boat was first being cleaned with a rough sand paper edge #2 and then finally cleaned with a smooth sand paper to smooth the surface of the boat. Then we obtained a solid sample of about 3 grams of gallium metal and deposited it in the cleaned boron nitride boat. The boron nitride boat containing the 3 grams of gallium is then inserted into the quartz liner. The liner protected the quartz process from contamination during growth and also provided a surface upon which GaN material is collected. Caution was taken so that the quartz did not touch the inside of the cap. We opened the NH₃ valve and then regulated the flow rate to 100 sccm. Then we turned on the oven and set the temperature to 900°C and then let the growth cycle continue for approximately 4 hours.

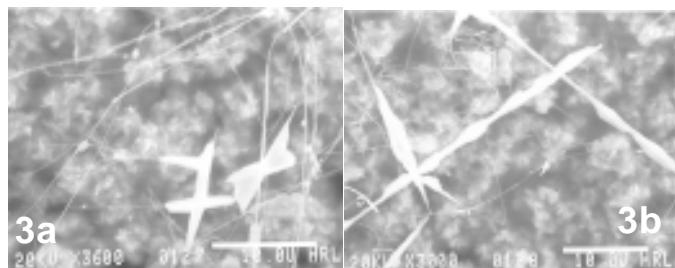
After the 4 hours period of growth cycle, the NH₃ valve is closed and the flow rate is set to zero. The vacuum system is turned off and then the appropriate procedures were followed in order to remove the quartz. When the oven temperature was



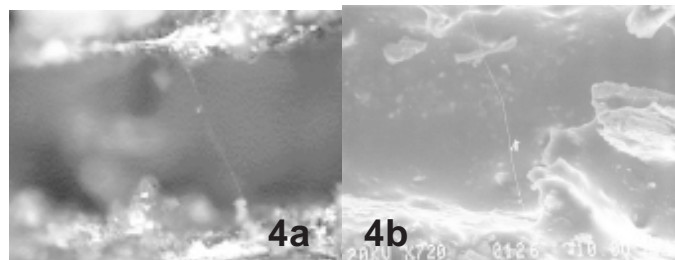
Figures 1a, 1b and 1c



below 100°C, we took the quartz liner out from the oven tube and took out the BN boat from the quartz liner. The content of the BN boat was carefully scraped out into a clean lab container. Likewise, the contents of the quartz line is also scraped out into the container. Then we began viewing the material from the container under the optical microscope. Each surface of the GaN material is carefully viewed under the optical microscope in search for the grown nanowires. Pictures of these nanowires were taken with the help of the computer, and the images are saved and stored. Figure 2a and Figure 2b shows the image extracted from the optical microscope, and Figure 3a and Figure 3b shows the image that was extracted from the scanning electron microscope.



We searched for nanowires for testing. The nanowires for test were extracted with tweezers and the extracted nanowire placed on an insulated copper circuit board. A conductive silver epoxy is used to glue down the nanowire to the copper circuit board. Figure 4a and Figure 4b shows an image of a GaN nanowire under test. The I-V characterization of the nanowire is obtained with the use of the programmable curve tracer. When the expected I-V curve is obtained, the nanowire can be fabricated into a device like diodes, lasers, led, transistors, etc. In order to determine the band gap of the nanowires, a photoluminescence test was performed. Figure 5 shows a PL result of our GaN sample at liquid nitrogen and Figure 6 shows a PL result at room temperature.



Discussion and Result:

The experiment was successfully completed. As a result, we found that physical structures of some nanowires were straight, short and uniform, and others long, curvy, and non-uniform. By testing the nanowires, the following was found. The band gap was found to be 3.25 electron volts. The wave length was found to be within the range of 364-369 nm when measured at room temperature and 371-372nm when measured at liquid nitrogen temperature.

Conclusion:

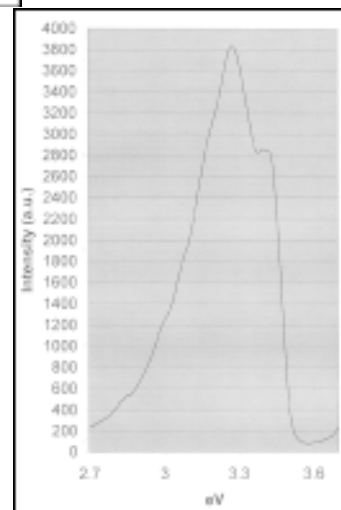
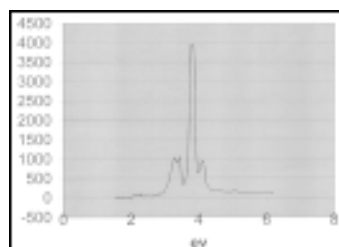
Generally, it is believed that nanowires have many great promises for the future of science and technology. Thus, in the future, we expect that nanowires will replace actual devices like diodes, transistors, detectors, emitters, etc. If nanowires replace devices, then the total size of computers will be decreased, and the speed will be increased. Altogether, at the completion of this project, GaN nanowires were successfully grown and characterized.

Acknowledgments:

I wish to thank the National Nanofabrication Users Network (NNUN) for organizing this REU program and Howard University (MSRCE) for providing the facilities that support research. Also, my thanks goes to Dr. Peizhen Zhou, Dr. Garry Harris, Michael Beyer and everyone for their support throughout my research period at Howard University.

References:

- [1] M. He, I. Minus, P. Zhou, S.N. Mohammad, J.B. Halpern, R. Jacobs, W.L. Sarney, L. Salamanca-Riba, R.D. Vispute. Appl. Phys. Lett. 77(2000) 3731.
- [2] W. Han, S. Fan, Q. Li, and Y. Hu, Science 277 1287-1289(1997).
- [3] C.M. Lieber, A.M. Morales, P.E. Sheelan, E.W. Wong, P. Yan., Proceedings of the Robert A. Welch 40th Conference on Chemical Research: Chemistry on the Nanometer Scale; 165-187, (1997).
- [4] R.N. Jacobs, L. Salamanca-Riba, M. He, G.L. Harris, P. Zhou, S.N. Mohammad, and J.B. Halpern., Structural Characterization of GaN Nanowires Fabricated via Direct Reaction of Ga Vapor and Ammonia., (to be publish in Appl. Phys.).
- [5] M. He, P. Zhou, S. N. Mohammad, G. L. Harris, and J. B. Halpern., (to be publish in Appl. Phys.).



Figures 5 & 6

InGaAsN Solar Cells made by Molecular Beam Epitaxy

Rob Klein, Chemical Engineering, UCSB, Rklein00@umail.ucsb.edu

*Principal Investigator(s): Dr. Gary Harris, Electrical Engineering,
Howard University, gharris@mscre.howard.edu*

Mentor(s): James Griffin and Crawford Taylor, MSRCE, Howard University

Abstract:

The basic InGaAsN structure was based on a 1999 paper from Sandia Laboratory, and using this same design we showed an open circuit voltage of 0.195 V and a short circuit current of 0.080 mA at AM1.5, which translates into an efficiency of 0.43% and a saturation current of 1.4×10^{-6} A/cm². We also varied the internal structure to try to increase efficiency. The main difficulty throughout testing was a high leakage current due to exposed edges and incomplete metal contacts.

Introduction:

InGaAsN could potentially greatly enhance the efficiency of a multi-layer GaAs-based solar cell. Despite the 4.3 eV band gap of GaN, when small amounts of N (1 to 3%) are added to GaAs the band gap drops to close to 1.0 eV [1]. The potential of the InGaAsN is centered around its low band gap and also its ability to have a 95% lattice match on GaAs.

Multiple materials with different band gaps, when layered together from highest band gap to lowest, can utilize the different frequencies of light according to which best fits their band gap, and thus create a solar cell with a much higher overall efficiency than an individual cell could get. An InGaAsN layer added to a 30% efficient GaP-GaAs cell could increase the efficiency to close to 40% [2].

Procedure:

The structures tested in this experiment were based on an InGaAsN solar cell structure previously made by Sandia Laboratory [2]. They were grown using molecular beam epitaxy. Hall and Conductance/Voltage tests were done on InGaAsN layers grown on semi-insulating GaAs substrates. The dots put down for the Hall measurement were Ge/Au/Ni, and the substrates were annealed at 530°C for 90 seconds. The dots put down for CV measurements were Cr/Au. Doping measurements were done for $n = 1 \times 10^{18}$, $n = 2 \times 10^{17}$, $p = 4 \times 10^{18}$, and $p = 1 \times 10^{15}$ (background).

A test GaAs sample solar cell was made using lithography techniques and metal evaporation. The ohmic contacts were Ge/Au/Ni, and were annealed at 530°C for

90 seconds. The Shoktty contacts consisted of a transparent layer of aluminum with an aluminum cross on top. Three attempts at an InGaAsN solar cell were made by MBE. The first (sample 1884) consisted of the structure shown in Figure 1 with an additional 500 Å $n = 3 \times 10^{18}$ GaAs between the n-InGaAsN and AlGaAs. The second (sample 1885) consisted of the structure shown in Figure 1. The third (sample 1888) was the structure of Figure 1 with the n-InGaAsN layer decreased to 0.85 μm. The mixed layers were approximately $\text{In}_{0.07}\text{Ga}_{0.93}\text{As}_{0.98}\text{N}_{0.02}$ and $\text{Al}_{0.8}\text{Ga}_{0.2}\text{As}$. Properties of the InGaAsN are assumed to be approximately equal to those found by Kurtz et al [2].

Multiple processing techniques were attempted, including lithography and evaporation, etching, scribing, and metal mask evaporation. The final processing involved metal mask evaporation, scribing, and testing. Metal was evaporated on the surface (Ge/Au/Ni) in the form of fingers with a wider backbone (shown in Figure 2), and the sample was annealed at 530°C for 90 seconds and then tested to ensure ohmic behavior. Boxes were then scribed around the metal contacts. InZn contacts were melted onto the backside and annealed at 450°C for 90 seconds, and then tested for ohmic behavior. No anti-reflection coatings were applied. Annealed samples were annealed at 700°C for 2 minutes, between sacrificial GaAs wafers. The solar simulator was calibrated for AM1.5.

Results and Conclusions:

The depth of scribing, found using a surface profiler, was 5 to 8 μm. This was deep enough to penetrate to the p^+ layer and essentially isolate the individual cells. Sample 1884 gave diode behavior, but had no response to light. The extra GaAs had two probable effects: absorbing most of the incoming light and thus preventing a light response; and providing a local surface for easy recombination of the electron hole pairs created in the InGaAsN p-n junction. Sample 1885 gave good diode behavior in the interior boxes of the sample, and produced a downward shift with applied light. This shift, when averaged across multiple test regions, gave data of $V_{oc} = 195$ mV, $I_{sc} = -80$ mA, $\text{Area} = 2.9$ mm², $\text{FF} = 0.636$, $I_0 = 4 \times 10^{-6}$ A/cm², and $n = 0.0043$.

The saturation current, I_0 , is a measure of the internal efficiency of the device. This I_0 was one order higher than that of the Sandia paper, indicating that our device was not quite as efficient as theirs. Sample 1888 gave leaky diode behavior at low applied voltages, but went ohmic at a relatively small collector voltage. The thinner p-n junction probably could not withstand the applied voltage and went into breakdown. Annealed versions of samples 1885 and 1888 performed the same as sample 1888, quickly going ohmic. The failure of these and sample 1888 indicate that the p-n junction was very sensitive and delicate.

The test GaAs sample gave data of $V_{oc} = 320$ mV, $I_{sc} = -20$ uA, Area = 0.364 mm², FF = 0.733, and $n = 0.016$. This efficiency is 3.5 times that of the InGaAsN. Calculations based on the band gap of GaAs and InGaAsN indicate that the GaAs should have an efficiency approximately 1.5 times that of the InGaAs. Thus it can be concluded that InGaAsN needs further optimization before a respectable power output can be created.

References:

- [1] Giant and Composition-Dependent Optical Bowing Coefficient in GaAsN Alloys. S. Wei, A. Zunger. Phys. Rev. Let., 76, 664-667 (1996).
- [2] InGaAsN solar cells with 1.0 eV band gap, lattice matched to GaAs. S.R. Kurtz, A.A. Allerman, E.D. Jones, J.M. Gee, J.J. Banas, B.E. Hammons. Appl. Phys. Let., 74, 729-731 (1999).
- [3] Green, Martin A., Solar Cells. Prentice Hall.
- [4] Donati, S. Photodetectors: Devices, Circuits, and Applications. Prentice Hall, New Jersey, 2000.

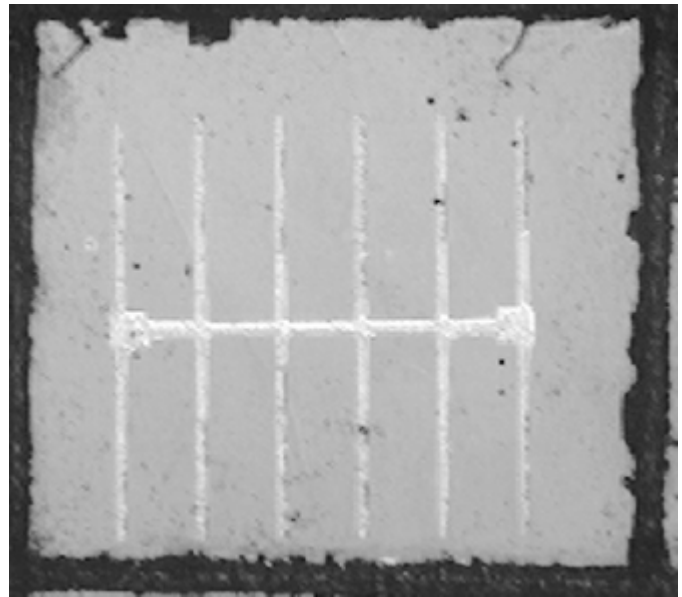


Figure 2: Top View of Device

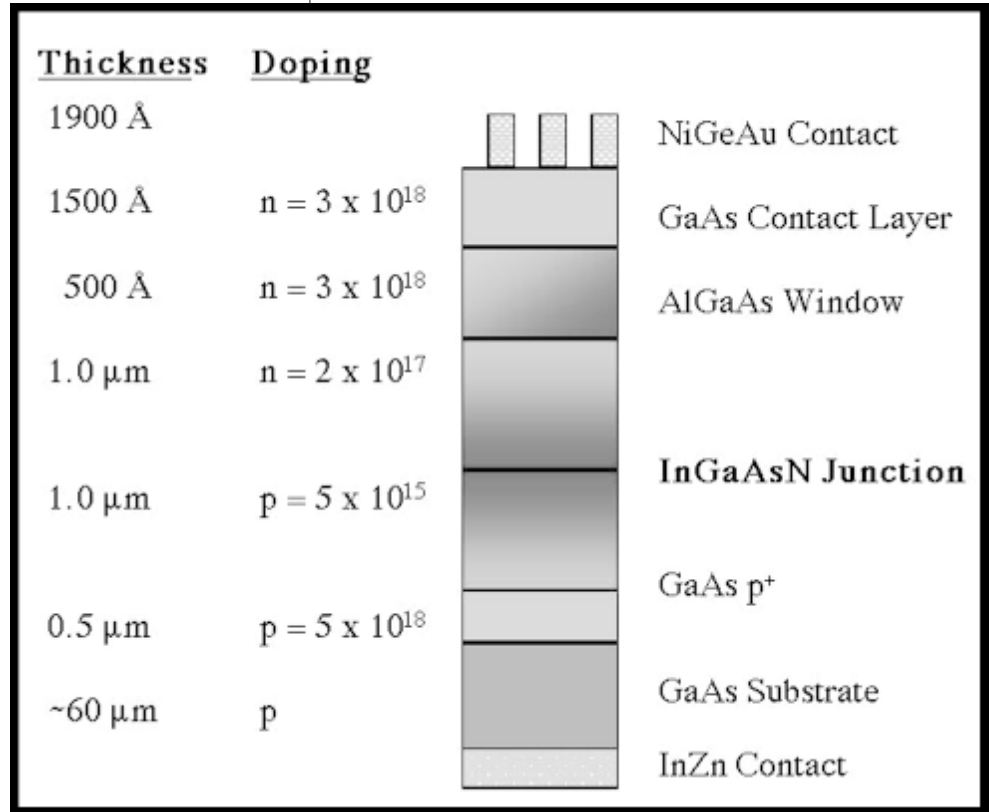


Figure 1: Solar Cell Structure

Fabrication of Ion Implanted SiC Nanofiltration Membranes

Court Wilson, Chemistry, Trinity College, Duke University, cpw@duke.edu

Principal Investigator(s): Dr. Gary L. Harris, Electrical Engineering, Dr. Kimberly Jones, Environmental Engineering, Howard University, gharris@msrce.howard.edu, kjones@scs.howard.edu

Mentor(s): Crawford Taylor, MSRCE, Howard University

Abstract:

Silicon Carbide (SiC), due to the semiconductor's high breakdown voltage threshold, allows for strong permanent electric fields to exist across large voltage differentials. Thus, when used as a Nanofiltration Membrane in conjunction with voltage differentials created by way of Ion Implantation, the result would be a static electric field within the membrane pores. Interaction of the resultant electric field with charged particles would help counter membrane fouling from colloidal and particulate matter.

This experiment was designed to fabricate and test SiC nanofiltration membranes, and investigate the effects of ion implantation on the efficiency of such devices. Using metallization and lithography techniques, 1 μm pores were etched into 1 to 6 μm layers of SiC on silicon backing. SiC nanofiltration membranes were then implanted with chloride and fluoride ions, and compared to identical unimplanted membranes by way of flux, percent rejection of contaminants, and amount of membrane fouling from prolonged use. A significant reduction in fouling characteristics in such a membrane would translate into more reusable and less costly membrane technologies that would require much less maintenance.

Introduction:

Nanofiltration Membrane-based technologies, while extremely efficient in filtering molecular and ionic material from hard water, are beset by the phenomenon of membrane fouling. Insoluble inorganic substances, colloidal and particulate matter, and soluble organic matter all constitute foulants which become deposited either on the membrane's surface or within the membrane's pores. As a result, increasing pressures are required to drive water through a membrane as it becomes fouled, which takes considerably more power in a water treatment plant. Furthermore, most microfiltration and nanofiltration membranes demand continuous cleaning, in some cases requiring cleansing every 20 minutes to clear the membrane surface, and eventually must be discarded and replaced. Thus the buildup of foulants contributes significantly to the expenses involved in the treatment of hard water using nanofiltration membranes.

Dr. Kimberly Jones of Environmental Engineering at Howard University has engineered a temporary solution to the buildup of ionic foulants. The process involves the implantation of negative ions within the surface of a nanofiltration membrane

through ion implantation, thus creating a zeta potential that acts to increase the rejection of divalent ions. However, due to the nature of the membranes, the implanted ions slowly dissipate in charge over several days, once again leaving a neutral membrane.

This experiment attempted to expand on the implementation of charged membranes in overcoming the hindrances of membrane fouling, but with a unique variant in nanofiltration membrane technology. Using fabricated SiC semiconductor membranes as the recipient of a voltage bias, the effectiveness of ion rejection was expected to become much stronger and more permanent. The advantages of SiC over previously implanted membranes include its strength and ability to retain the ions implanted within it. Furthermore, due to SiC's unique semiconductor properties, particularly its high breakdown voltage allowing it to operate in strong self-induced electric fields, voltage biasing of a SiC filter would result in permanent electric fields between high and low potentials across the material. The presence of such electric fields within the pores of a SiC membrane could act as a strong deterrent to fouling by charged ions and polar compounds.

Unfortunately, the presence of a strong electric field within the pores of a membrane, while leading to a higher rejection of unwanted ions in a filtered solution, could also serve as a hindrance to water flow across the membrane. Therefore, it was necessary to test the effects of voltage biasing on the reduction of flux through SiC membranes.

Procedure:

The experiment was conducted in three phases. The first involved the fabrication of a 1 μm thick SiC filter with pores of 1 μm diameter, and on top of similarly porous silicon backing for structural support. 3C-SiC was grown by way of using carbon and silicon sources gases by chemical vapor deposition (CVD). A layer of SiC from propane was first deposited so as to create a buffer between the structures of Si and SiC. Inert N_2 and H_2 were introduced as carrier gases, with silane and propane providing gaseous sources of silicon and carbon, respectively.

Membrane Fabrication:

Following the growth of 1.2 μm SiC on Si, the samples were cleaned with detergent, trichloroethylene (TCE), acetone, methanol, and deionized water. A 3000 \AA layer of nickel was then deposited on their surface by way of metallization. This

was accomplished by evaporation, which reduced the chamber pressure to 5×10^{-7} Torr, then melted and evaporated a nickel source under the samples using an electron beam to deposit the desired layer of nickel atop the SiC surface. Samples were then annealed at 550°C in argon gas to ensure nickel adherence.

Lithography was used to prepare the samples for the etching of 1 μm pores. By first covering their surface completely, and then spinning the samples at 4000 rpm for 30 seconds, the samples were covered with a 0.4 μm layer of photoresist. After being hardened for 30 minutes, the photoresist layer was then exposed to ultraviolet radiation while covered by a negative mask exposing uniform 1 μm dots. The source of radiation served to break apart 1 μm wells of photoresist, which during the ensuing immersion in toluene and developer served to open 1 μm holes in the photoresist layer.

Acid etching was used to extend the 1 μm pores in the photoresist layer into the deposited nickel above the SiC. The samples were immersed in a solution of 1:1 HNO_3 and HCl for 30 seconds, followed by the removal of the photoresist layer with acetone to leave a nickel membrane on the SiC layer.

Using reactive ion etching with SiF_6 as an etching agent, the 1 μm pores in the nickel layer were extended into the underlying SiC, creating the desired SiC membrane. Subsequent immersion of the samples in 1:1 HNO_3 and HCl removed the nickel layer atop the SiC.

With the SiC membrane completed, the Si backing was then fabricated. First the rear faces of the samples were sanded and polished to yield a smooth surface, which was subsequently cleaned. Lithographic techniques similar to those involved in the creation of the SiC membrane were then implemented. Exposing and developing windows of approximately 0.5 centimeters in length to an applied layer of photoresist left square surfaces of Si underneath a frame of covering photo-resist. Subsequent immersion of this surface in acidic 5:5:2 $\text{HF}:\text{HNO}_3:\text{H}_2\text{O}$ etched the Si backing through the windows, creating a structural foundation for the supported SiC membrane.

Though the Si frame provided considerable support, the SiC film was still considerably fragile in the unsupported regions within the windows. Therefore, in order to strengthen the membranes, a 2500 Å layer of gold was deposited using metallization across the back of the filters, providing more localized support for the SiC layers. Subsequent analysis by a scanning electron microscope (SEM) concluded that the layer of gold did not obstruct the pores within the SiC membrane, and fully adhered to the rear of the filter.

Ion Implantation:

Ion implantation of the fabricated membranes was not conducted, as the fabrication process was too costly and time consuming. However, a simulation of the ion implantation process was performed by the program SRIM in order to calculate and project embedding depth of the implanted ions given initial ion energy in kilo-electron-volts (KeV), which provided the implanting ions with the momentum to penetrate the upper surface of the membrane. Other independent variables factored into the SRIM equation included membrane density,

which decided the nuclear forces slowing the ions' penetration rates, and ion size and charge, which determined the electrical forces acting to similarly slow ion penetration rates. The dependant variable was the depth at which the penetrating ions would be halted from retarding electrical and nuclear forces. In order to isolate implantation to the upper surface of the SiC membrane and create a bias across the membrane pores, ion energies that resulted in short stopping depths were decided to be optimum. The resultant stoppage depths were 150 Å from 17KeV for chloride ions and 154 Å from 10KeV for fluoride ions.

Results:

Testing of the membranes was conducted using a nitrogen pressurized water pump to drive water through the filter. As an alternative to the permanent voltage biases of ion implantation, several attempts were made to include the membrane as a resistor in an electrical circuit, which would create a similar voltage bias. However, due to incompatibilities between electrical circuitry and membrane technology, such attempts were unsuccessful. Therefore testing was conducted exclusively on un-biased membranes. Membranes were tested for the flux of water flowing through them at varying pressures, with organic membranes serving as a negative control against which non-biased membranes were compared.

Membranes were held in place by customized membrane backings constructed for each membrane, as their fabrication did not structurally prepare them for insertion into the testing apparatus. 0.1 μm membranes, which at the tested pressures were effectively impenetrable to water, were placed around the membranes to isolate desired porous areas for testing. Water pressurized at from 2 to 10 psi in increments of 2 psi was then run through the membranes and collected in a beaker. Measurements of the amount of time for specific mass collections of water in the beaker were then taken. Graphing this data allowed for determination of the slope of the calculated linear regression, revealing the average rate of mass accumulation of water in grams per second for each set pressure. Then, using the density of water, the average flow rate in milliliters of water per second was determined. Flux was determined from this information using membrane surface area, number of pores, and pore size.

Conclusion:

Further avenues of research include creating a voltage bias using ion implantation, fabricating membranes with thicker layers of SiC and smaller pore sizes, and testing for membrane fouling and rejection of negative ions.

**The Penn State Nanofabrication Facility
 Pennsylvania State University, University Park, PA
<http://www.nanofab.psu.edu/start/default.htm>**

2001 REU Interns



REU Intern School Affiliation Principal Investigator

Front Row, L to R:

Ms. Lisa Daub Penn State Nanofabrication Facility PSNF REU Coordinator
 Mr. Alexander Wissner-Gross MIT Paul Weiss
 Mr. Arthur Carter Wake Forest University Stephen Fonash
 Ms. Joy Liu UC Berkeley David Allara

Second Row, L to R:

Ms. Teresa Bixby Susquehanna University Carlo Pantano
 Ms. Jamie Fontaine The Pennsylvania State University Stephen Fonash
 Ms. Heather Russell Pacific Lutheran University Ying Liu
 Dr. Mark Horn Penn State Nanofabrication Facility PSNF REU Coordinator

Study of Gamma-Aminopropyltriethoxysilane Coatings on Glass Substrates for DNA Microarrays

Teresa J. Bixby, Chemistry and Physics, Susquehanna University, bixby@susqu.edu

Principal Investigator(s): Dr. Carlo Pantano, Ezz Metwalli, Material Science,
Penn State University, pantano@ems.psu.edu

Abstract:

DNA microarrays have the capability of revolutionizing biological research because of the ability to simultaneously test multiple experimental conditions. A library of known DNA fragments are bound to a substrate in a printing process, and then this 'DNA Chip' is exposed to an unknown mixture of DNA. Subsequently, the substrate is thoroughly cleaned to remove all excess or non-specifically bound DNA strands. The degree of DNA immobilization for each of the DNA fragments on the chip is determined from fluorescence measurements. Therefore, creating a bonding site that will strongly attach the specific strands is advantageous for testing minute or dilute samples.

Glass substrates were coated with gamma-aminopropyltriethoxysilane (APS) from aqueous solution to create a linker system on the glass surface for DNA immobilization. Several different post-printing conditions, similar to those that the substrates might undergo during DNA testing, were analyzed using x-ray photoelectron spectroscopy (XPS). Atomic force microscopy (AFM) was used to measure the roughness of the surface and to examine the coating morphology and uniformity. Contact angles were measured to determine hydrophobicity of the coating, important when spotting the substrate with the DNA.

Introduction:

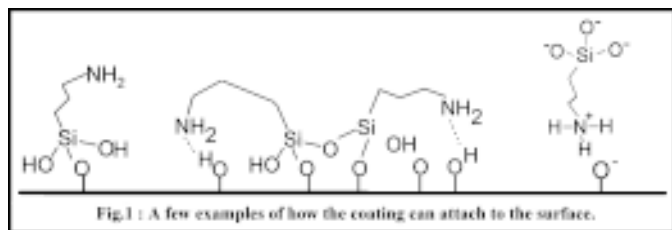
The DNA immobilization process as a whole has been tested using several different substrates, coatings and procedures, but individual steps have not been examined. Because boiling is one of the steps in DNA analysis, the linker system must be able to withstand this exposure. Curing temperatures have been tested in other research; this variable may strengthen the substrate-coating bond. Curing atmosphere, likewise, may have an effect on what is found on the surface. N_2 was used as a curing

atmosphere to determine if carbon and oxygen in regular atmosphere curing would bake onto the surface. One set of samples was also exposed to D-ribose, the sugar component in RNA, to test its retention on the coated surface. X-ray photoelectron spectroscopy will be used to qualitatively examine the amount of coating on the surface. Nitrogen content observed on the samples will be a reasonable indicator as it is an element unique to the coating and not found in the substrates. AFM will be used to determine whether there is a relationship between surface roughness and fluorescence yield. If, by boiling the coated samples, divots or holes were created on the surface, this may affect immobilization. Contact angle will be used with water to determine the hydrophobicity of the samples. A more hydrophobic surface is advantageous in the spotting of DNA; it allows more spots to be placed closer together with a minimum of overlap or bleeding. Contact angle was also used with the samples exposed to D-Ribose to examine the possibilities for the orientation of the molecules, useful in determining what functional groups the coating attracts.

Procedure:

Substrates used included BoroFloat (80% SiO_2 ~ 13% B_2O_3 ~ 2% Al_2O_3 ~ 3% Na_2O ~ 1% K_2O) and AF45 (50% SiO_2 ~ 14% B_2O_3 ~ 11% Al_2O_3 ~ 24% BaO ~ 1% As_2O_3).

Prior to coating with the linker, the substrates were cleaned. All of the glass samples were placed in a 10 weight percent solution of sodium hydroxide for 24 hours. After rinsing and sonicating for 5 minutes in R.O. water, the samples were placed in a 10 weight percent solution of hydrochloric acid for 15 minutes. Again, they were rinsed and sonicated in R.O. water for 5 minutes followed by 5 minutes of sonication in methanol. To coat the samples with the linker, the cleaned glass substrates were soaked in a 5 weight percent aqueous solution of gamma-aminopropyltriethoxysilane for 15 minutes, followed by a rinse with methanol and R.O. water and 10 minutes in 5 weight percent aqueous solution of D-ribose. Samples were again rinsed with methanol and R.O. water then boiled, if applicable, in R.O. water for 10 minutes. Each sample was then sprayed with ethanol, dried with N_2 and cured.



Results and Conclusions:

Results show that the AF45 substrate bound more originally, and retained more with boiling, of the coating. While much of the coating was removed during boiling, it is speculated that out of the many layers of coating originally found on the surface, the base layer bound to the substrate was not affected. This, however, suggests that any desired DNA not bound to that base layer might be removed by boiling. Comparable results were collected for the samples with D-ribose, except in those cases the Borofloat substrate retained more than the AF45. Contact angles taken for the D-ribose samples were noticeably higher than those without the D-ribose. No noticeable trends or differences were observed due to curing atmosphere. This could further be explored with varying temperatures and curing times. To form a more complete set of data, fluorescence tests would be advantageous. It was intended that these tests be done but due to time constraints, it remained unaccomplished.

An important conclusion remains, however, that boiling does remove the linker from the substrate, not the DNA from the linker. Therefore, more reliable chips require a linker system designed to form a stronger bond with the substrate without sacrificing its ability to bind DNA.

Acknowledgements:

I would like to thank Dr. Pantano, the entire group and all of the staff in the MRI building at Penn State for making my summer much more than a learning experience, especially to Vince Bojan for his infinite patience. Thanks to the NNUN program, the NSF, and all of my fellow interns who have become such good friends.

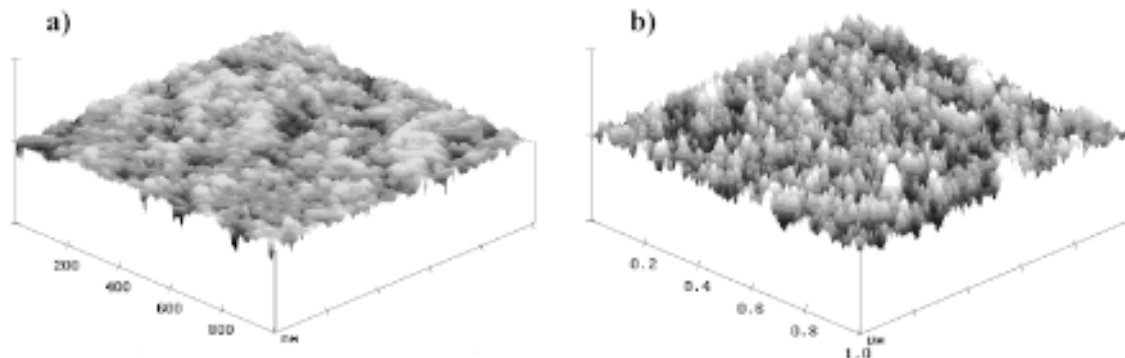
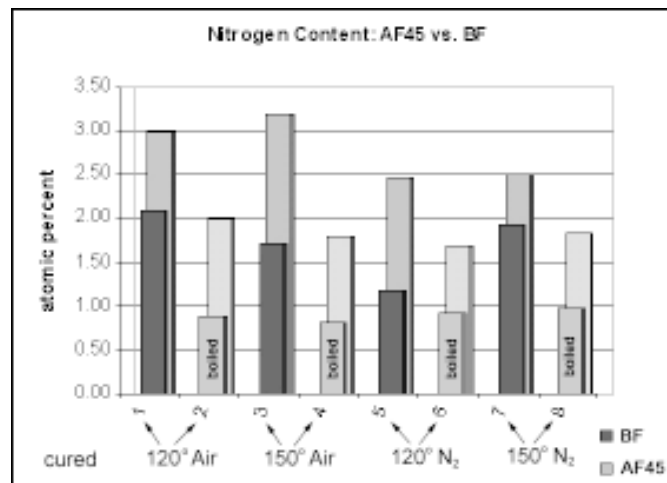


Fig 2: AFM images a) coated sample, RMS: 1.009 nm, b) coated and cleaned sample, RMS: 1.055 nm.



Investigation of Cell Differentiation and Film Behavior of Nanofabricated Thin Films

Arthur Francis Carter, Jr., Chemistry, Wake Forest University, cartaf03@wfu.edu

*Principal Investigator(s): Dr. Stephen Fonash,
Engineering Science, Penn State University, sfonash@psu.edu*

*Mentor(s): Joe Cuiffi, Dan Hayes, Engineering Science,
Penn State University, jdc167@psu.edu, djh195@psu.edu*

Abstract:

Films were investigated for a proposed cell culture and manipulation chip. Common and novel films' etching behavior was observed in Ham's Media. Select films were coated with collagen, and while coated and non-coated, films' compatibility with photolithographic patterning methods and collagen adhesion were observed. Hepatocyte cells were then deposited on films, while cell growth based on film selectivity was noted and observed through the use of a Field emission scanning electron (FE-SEM) microscope. Polymer BCB, and porous silicon both showed cell growth when used with collagen; while Silicon dioxide (SO₂) films showed cell growth with and without collagen. Non-coated obliquely deposited SO₂ gave the largest amount of adherent cells without collagen.

Introduction:

The future of industrial pharmaceutical drug testing depends on the development of a nanofabricated device that enables controlled cell growth, mobility, as well as controlled cellular environment exposures. The Food and Drug Administration requires pharmaceutical companies to test specified numbers of animals to have a drug approved; each test observes the effects on a specific cell type or organ. There is interest in the manufacturing of nanofabricated experiment and trial devices. With decreased size, nanofabricated devices decrease the

amount of animals tested, the duration for experiment results, while increasing the control of experiments run, subsequently decreasing the amount of reagents required, resulting in a significant decrease in cost and time. A chip composed of an inexpensive film, patterned for micro-fluidics by photolithography that tested a number of individual cell types, would revolutionize drug marketable testing.

This study looks at various common and novel films, on which desired cell growth occurs and cell adhesion is optimized. By observing cell growth and etch survivability, it is possible to select films which will be suitable for a drug testing device. Hepatocytes, as most somatic cells, are adherent cells; this means that normal life processes and protein production only occurs when the cells are adherent. Collagen is a substance that promotes cell-substrate adhesion. While collagen promotes cell adhesion, it is hypothesized that textured surfaces, increased surface area, will also increase cell adhesion. Collagen was added to films, while silicon dioxide texturing and porous silicon were used to observe study.

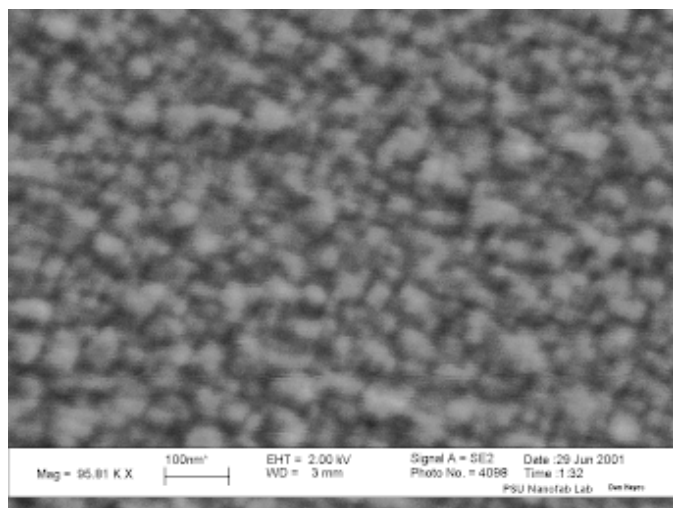
Procedure:

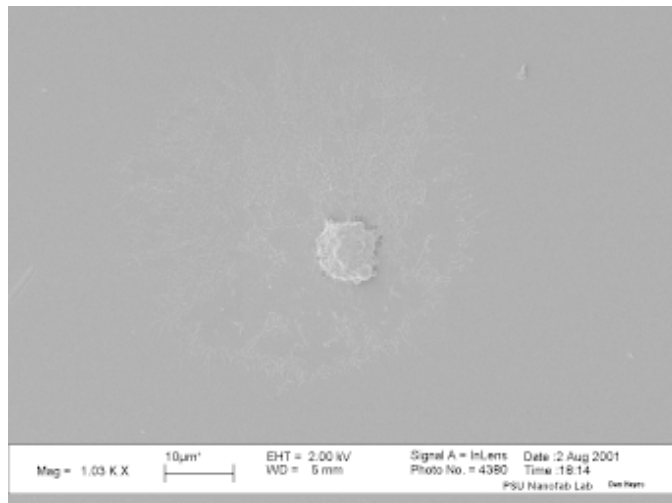
Media Preparation:

One liter, 95% deionized water and Ham's F12K medium with 1.5 grams sodium bicarbonate, and 5% heat inactivated fetal Bovine serum. 10 mL 2 mM L-Glutamine with added penicillin and streptomycin was also added to the media (Ham's). This media was stored in a standard refrigerator unit.

Film Production:

Columnar Porous Silicon samples were prepared and provided [1], as were Benzocyclobutene (BCB) [2]. The SO₂ samples were prepared and altered with the aid of Joe Cuiffi. SO₂ samples were evaporated normally and obliquely onto silicon wafer. Some oblique samples were not cleaned with isopropyl alcohol (IPA) or acetone, while other samples were cleaned with deionized water, IPA, and acetone.





Cell Preparation and Survivability Testing:

FL83B Hepatocyte cell lines were purchased from the American Type Culture Center (ATCC) and cultured in 10 mL of Ham's media at 37°C incubator with 5% CO₂. Based on visual and microscopic inspection cells were split as needed.

Photoresist was added to the edges of each film and placed in a petri dish containing 5 mL of Ham's media. Initial etch studies were run for two hours. Subsequent etch studies ran between one and three hours. The films were then washed with IPA and acetone to remove the photoresist. Preliminary analysis was visual and further analysis was done by profilometer.

Patterning and Cell Adhesion:

A provided pattern [3] was used to pattern select films [4] through standard wet photolithographic methods using photoresist 1813. Patterned samples had a collagen solution applied to the surface prior to patterning.

Results:

The columnar porous silicon samples proved fragile in the Ham's media. After two hours, these samples were entirely etched. BCB samples did not etch over any period of time. Normally deposited SO₂ samples did not etch, while the oblique SO₂ samples showed slight signs of etching. Oblique SO₂ samples showed growth of a thin protein film, which was characterized by X-ray photoelectron spectroscopy [5].

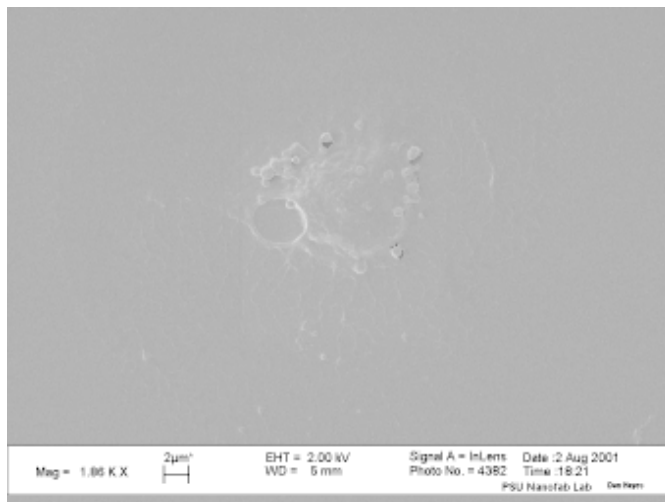
BCB allowed good collagen adhesion, and patterning ability. Cells adhered to the surface of the collagen. The porous silicon allowed for collagen adhesion, with marginal success for cell adhesion to collagen. The porous silicon samples showed collagen liftoff when the film etched in media. The oblique SO₂ samples showed good cell adhesion with and without collagen.

Conclusions:

All tested samples allow cell adhesion if collagen coating is used. Oblique SO₂ samples seem optimistic because of their creation of a protein layer and greatest cell adhesion without collagen. Along with more cell adhesion tests, and optimization of dehydration techniques, future tests should be conducted with microfluidic flow chamber devices, observing the actual adhesion strengths.

Acknowledgements:

- [1] Samples provided by Dan Hayes and Joe Cuiffi of Stephen Fonash's research group at the Pennsylvania State University.
- [2] Samples provided by Guy Lavelle of the Pennsylvania State University.
- [3] Pattern was made by Amy Brunner of the Pennsylvania State University. Cell imaging was take by Dan Hayes on a Field-Emission Scanning Electron Microscope.
- [4] Dewez JL, Lhoest JB, Detrait E, Berger V, Dupont-Gillain CC, Vincent LM, Schneider YJ, Bertrand P, Rouxhet PG. Adhesion of mammalian cells to polymer surfaces: from physical chemistry of surfaces to selective adhesion on defined patterns. *Biomaterials* 19 (16): 1441-45 Aug 1998.
- [5] XPS analysis done by Jeffery R. Shallenberger.



Enhancement of Large Molecule Detection and Signal Sensitivity for MASiF

Jamie Fontaine, Biology, Penn State University, jmf271@psu.edu

*Principal Investigator(s): Dr. Stephen Fonash,
Engineering Science, Penn State University, sfonash@psu.edu*

*Mentor(s): Joe Cuiffi, Dan Hayes, Engineering Science,
Penn State University, jdc167@psu.edu, djh195@psu.edu*

Abstract:

With increasing interest in the emerging field of proteomics, characterization and detection techniques of proteins are being developed and improved. Mass analysis using silicon films (MASiF) is a matrix-free technique useful in detection and characterization of proteins and molecules ranging between 0 and 6,000 Daltons. The purpose of this study was to develop an additive to enhance signal sensitivity, and specifically enhance large molecule detection for MASiF. Bradykinin (1060.2 Daltons) and Insulin (5777.6 Daltons) solutions were prepared and combined with amino acid additives; these combined solutions were tested on the surface of porous silicon coated glass substrates. Various amino acid additives increased analyte signal sensitivity, detection of large molecules, and were also found to suppress background signal.

Introduction:

The characterization and detection of proteins is an important application of mass spectrometry, and as the field of proteomics continues to develop, it is necessary to improve and develop such techniques. Mass analysis using silicon films (MASiF) is a matrix-free method for

laser desorption/ionization on column/void-network nanoporous silicon thin films. In contrast to matrix-assisted laser desorption ionization (MALDI) mass spectrometry, MASiF analyzes small molecules by Time of Flight (TOF) Mass Spectrometry. For analysis of low-mass analytes ($m/z < 500$), irreproducible and heterogeneous cocrystallization, suppression of ionization by electrolytes and other additives, and interference from matrix ions have limited the utility of MALDI [1].

Prior MASiF experimentation has proven detection of molecules ranging between 0-8,000 Daltons, depending on sample preparation. The purpose of this study was to improve MASiF by developing an additive to specifically enhance detection of large molecules and signal sensitivity. The amino acids: aspartic acid (133.1 Daltons), arginine (174.2 Daltons), alanine (89.09 Daltons), and phenylalanine (165.2 Daltons), were tested as additives for MASiF; these amino acids were acidic, basic, neutral, and neutral, respectively. Amino acids are small molecules that have novel acid-base properties, varied structures, chemical functionalities of the amino acid side chain, and are biologically compatible and inexpensive (Garrett, 1999). Solutions of amino acids were prepared at concentrations ranging between 100 mM and 50,000 mM; these solutions were combined with Bradykinin (1,060.2 Daltons) and Insulin (5,777.6 Daltons) molecules. These proteins were chosen because Bradykinin is used as a calibration standard for mass analysis and Insulin is a large molecule.

Experimental Procedure:

Substrate Preparation:

Our columnar/void-network silicon films are deposited onto glass substrates by plasma enhanced chemical vapor deposition (PECVD) using a Plasma Therm, electron cyclotron resonance (ECR) high-density plasma source. This technique produces a nano-structured columnar/void silicon film at low substrate temperatures (100°C) (Figure 1). The glass substrates were coated with between 500 and 10,000 Å of the deposited columnar/void-network silicon film. All mass spectra presented in this report were obtained using columnar/void-deposited silicon prepared at 8-mTorr process pressure [1].

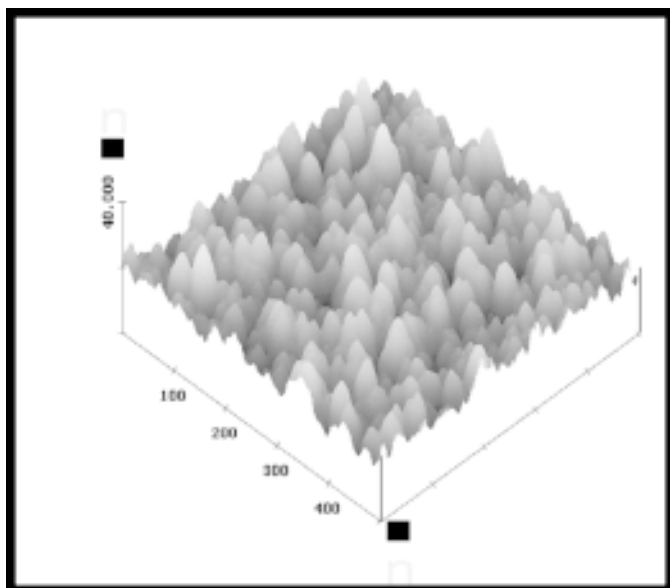


Figure 1: Atomic Force Microscopy image of void-columnar silicon films deposited at 100°C at 8 mTorr.

Sample Preparation:

The amino acids, Bradykinin and Insulin, used for this study were obtained from Sigma. The amino acid additives were prepared by combining the amino acids with Deionized (DI) water in concentrations of 100 mM, 1,000 mM, 10,000 mM, 25,000 mM, and 50,000 mM.

A 1 mM solution of Bradykinin and a 1 mM solution of Insulin were prepared using DI water. These solutions were used to make a 1 mM test solution of Bradykinin and Insulin, which was used to test the amino acid additives. Allowing 1 picoM of the Bradykinin and Insulin solution combined with 1 mL of the 100 mM, 1,000 mM, 10,000 mM, 25,000 mM, and 50,000 mM solutions of the aspartic acid, arginine, alanine, and phenylalanine, respectively, to air-dry on the surface, completed the matrix-free preparation of the sample on the columnar/void-network silicon film coated glass surface.

Sample Analysis:

All samples were analyzed using a Perseptive Biosystems (Framingham, MA) Voyager-DE STR mass spectrometer using 337-nm light from a nitrogen laser. The glass substrates were attached to the face of the conventional MALDI target using double-sided tape. Analyses were performed in a linear mode with instrument parameters identical to normal MALDI operation, except that no low-mass cutoff was employed [1].

Results and Conclusions:

Our results do not only show the usefulness of MASiF for large molecule detection and signal sensitivity, but

they also show that the additives tested reduced lower end noise unexpectedly. The MASiF results for the aspartic acid additive and Bradykinin and Insulin sample proved detection of both Bradykinin and Insulin molecules (Figure 2). Increased ionization of the Bradykinin and Insulin molecules and large molecule detection of the Insulin molecule was noticed with the addition of the aspartic acid additive in comparison to the MASiF results for pure Bradykinin and Insulin solution. Also, the lower end noise was unexpectedly reduced in the presence of the aspartic acid additive (Figure 3). The arginine, alanine, and phenylalanine sample solutions also suppressed the lower end noise to some degree. However, detection of the insulin molecule was not proven by the arginine, alanine, or phenylalanine.

These experimental results were expected, and matched the experimental design. The acidic amino acid, aspartic acid, provided the best results for detection and signal sensitivity, and the basic amino acid, arginine, suppressed detection and signal sensitivity. Aspartic Acid is the only amino acid additive that proved detection of both Bradykinin and Insulin. The use of this additive increased detection of larger molecules. Also, ionization was increased for both molecules, and upper and lower end noise was suppressed unexpectedly. Detection of large molecules has been successfully completed, therefore increasing the usefulness of MASiF.

References:

- [1] Cuiffi, Joe D., et al. 2000. Desorption-Ionization Mass Spectrometry Using Deposited Nanostructured Silicon Film. *Analytical Chemistry*. 10:1021.
- [2] Garrett, Reginald H., 1999. *Biochemistry*. Harcourt College Publishers. Orlando, FL.

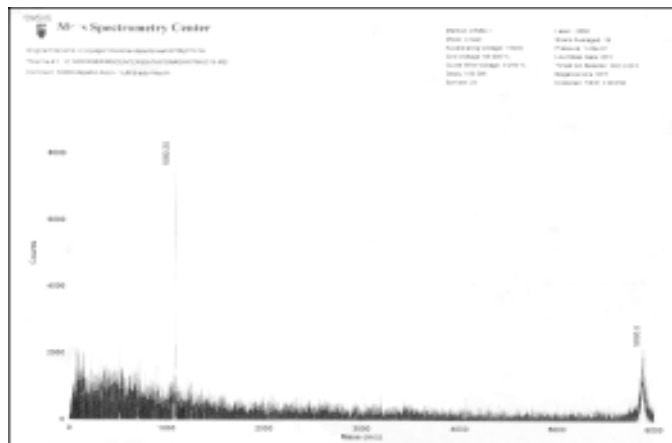


Figure 2: MASiF Mass Spectrometry spectrum of the aspartic acid 50,000 μ M additive combined with 1 picoM of Bradykinin and Insulin solution. The first peak at 1080.20 m/z represents the detection of the Bradykinin molecule, and the second peak at 5895.80 m/z represents the detection of the Insulin molecule.

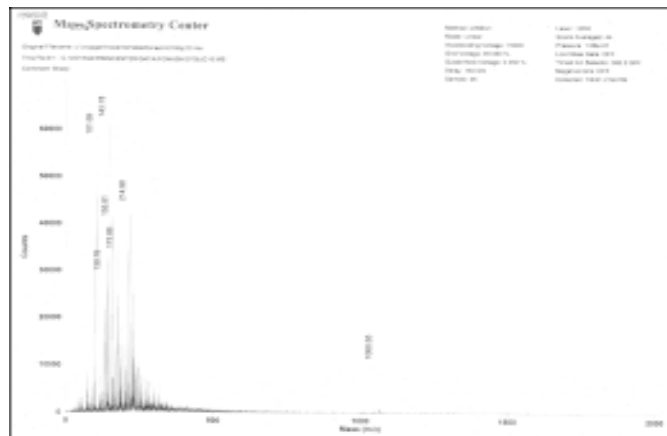


Figure 3: MASiF Mass Spectrometry spectrum of 1 picoM Bradykinin and Insulin solution. The peaks shown at the lower end of the spectrum are due to lower-end noise. The tiny peak at 1060.65 m/z represents the detection of Bradykinin.

Fabrication and CV & IV Characteristics of Metal-Insulator-Metal Structures

Joy Liu, EECS, UC Berkeley, joyliu@uclink4.berkeley.edu

Principal Investigator(s): Prof. David Allara, Chemistry,
Pennsylvania State University, dla3@psu.edu

Mentor(s): Tad Daniel, Chemistry, Pennsylvania State University

Abstract:

The basis of molecular electronics comes from the finding that molecules can function like semiconductor devices. With molecular electronics, the size of today's electronics could be significantly scaled down; thus, tiny devices with high production yield could be achieved.

Poly(methyl methacrylate) (PMMA), which is similar in thickness to molecular films, and Tetraethyl ethoxy silane (TEOS), which is a precursor of SiO_2 , are two well established insulators that can be made into nanometer thin films. Studying the fabrication methods and electric properties of metal-insulator-metal (MIM) structures using these films provides a foundation for the study of electron transfer in metal-molecule-metal structures and explores methods for making ultra thin dielectrics for molecular electronics.

Procedure:

0.1% PMMA solution was prepared, by weight, with chlorobenzene. TEOS solution was prepared, by volume with ethanol and pH with HCl. Undoped 2" Si wafers were cleaned with Piranha, ethanol, and N_2 gas. Each wafer was tested with single pt. null ellipsometry to the ensure substrate evenness and quality. Either 100 Å Cr with 1500 Å Au (thermal) or 500 Å Ti with 1500 Å Pt (e-gun) was evaporated onto the wafers, creating Metal Layer 1 (ML1), the base metal of the MIM structure. After the evaporation, null ellipsometry at three points was taken as a basis for future film thickness measurements and quality assurance. AFM images were taken for initial roughness measurements. The films were then spun on the wafers. If the wafers were left out for over a day after the evaporation, they

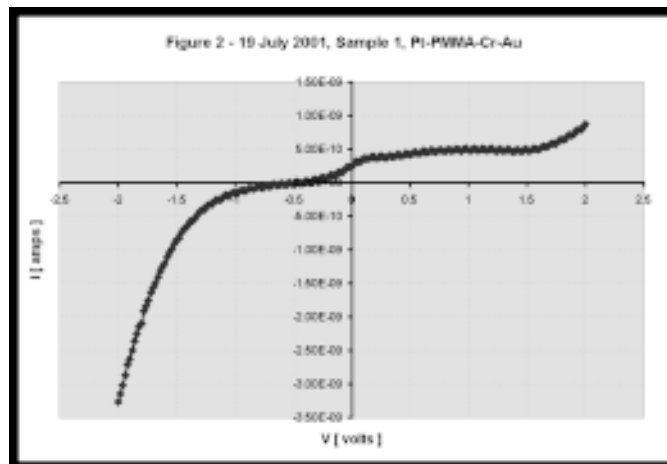
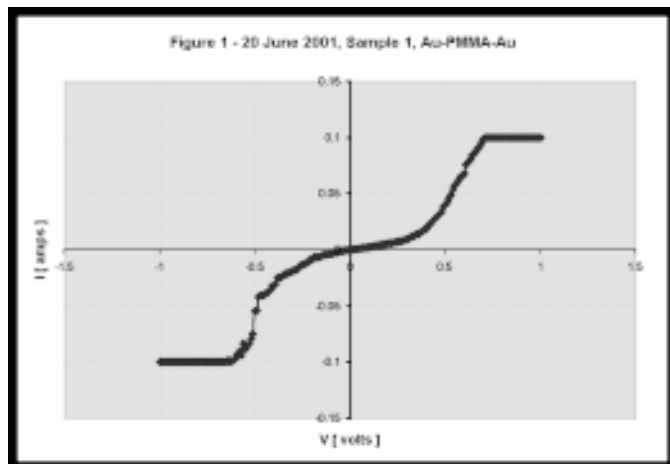
were UV ozoned for ~7 min so that organics, due to open-air exposure, would be removed.

Before applying film solutions to the Au ML1 wafers, ~3 mL (until surface is covered) of 30% H_2O_2 was applied to the wafers for ~5 min, then spun off at 7.5V (~3000 rpm) for ~5 min — until the H_2O_2 was no longer visible. The 30% H_2O_2 helped clean the Au and acted as a pre-bonding agent for the film. There was no pre-bonding step for the Pt ML1 wafers because H_2O_2 does not react well with Pt.

Using a syringe with a 0.45m or 1.0m filter, 3-5 mL of film solution was applied to each wafer until the surface was completely covered. For PMMA, the solution was left to sit on the wafer for 3-5 minutes before spinning. While the TEOS solution was immediately spun for better film smoothness because the solution was thicker. The wafers were spun for 5 min at 7.5V, until the solution was no longer visible. Null ellipsometry at three points was taken to determine the film thickness and uniformity with the AutoEl program. A refractive index of 1.43, 0.00 (k, n) was used for PMMA, and 1.46, 0.00 for TEOS. AFM images were also captured so that the ability of the film to planarize of the device could be analyzed.

Shadow masks with five different sized circular dots (diameters: 1.125 mm, 839.5 μm , 625 μm , 380 μm , 291.5 μm) were placed over the wafers for the second evaporation. The shadow masks were the final step responsible for creating ~100 devices on each wafer. A 1500 Å Au, 1500 Å Pt, 100 Å Cr with 1500 Å Au, or 500 Å Ti with 1500 Å Pt layer was evaporated through the mask, to complete the top, ML2, of the device.

Two probes and an optical microscope were used to measure IV and CV characteristics. The first probe was scraped through



% Solution	Approximate Film Thickness
50% PMMA (1 μ filter)	25-30 Å
60% PMMA (1 μ filter)	30 Å
70% PMMA (1 μ filter)	30-35 Å
100% PMMA (1 μ filter)	35-40 Å
100% PMMA (0.45 μ filter)	30-40 Å
20% TEOS (0.45 μ filter)	25-45 Å
40% TEOS (0.45 μ filter)	75-95 Å

the film surface until ML1 was probed. The second probe was slowly lowered onto ML2 until it was touching the surface. IV was measured with an HP4145. Wafers with IV characteristics that exhibited breakdown fields were probed until one device of each of the five different sizes was found. These working devices were noted with a permanent marker. CV was then measured on these working devices using an HP4284. The dielectric constant and breakdown fields of the devices with measurable capacitance and leakage current values were then calculated using the following equations:

$$(\text{dielectric})K = \frac{Ct}{A\epsilon} \quad (\text{breakdown})F = \frac{V}{t}$$

where t is the film thickness, C is the capacitance, A is the device area [$\pi(\text{diameter}/2)^2$], ϵ is the permittivity of free space (8.854×10^{-14} F/cm), and V is the voltage immediately before leakage current was observed.

Results and Conclusion:

AFM images showed that the films reduced the roughness of ML1 and that Au was rougher than Pt. Original Au ranged 5-20 Å in roughness, while original Pt ranged 3-10 Å. When applying the PMMA film to the Au, roughness decreased to 4-13 Å. Roughness was also further decreased on the Pt to 2-5 Å. The TEOS decreased the roughness to 2-17 Å on the Au, and 1-7 Å on the Pt. These results show that this spin-on application of films helps planarize the devices. Additionally, null ellipsometry proved that consistent nanometer thin films can be achieved using these methods (see table 1).

PMMA device IV and CV measurements did not yield breakdown fields or constant capacitance values. However, these devices did have measurable IV characteristics. Figure 1 shows Y-axis symmetry because both metals were Au, while Figure 2 is asymmetric due to the differences in the work functions between Pt ML1 and Cr/Au ML2. The characteristics of the devices are measurable, even though they are not the desired results.

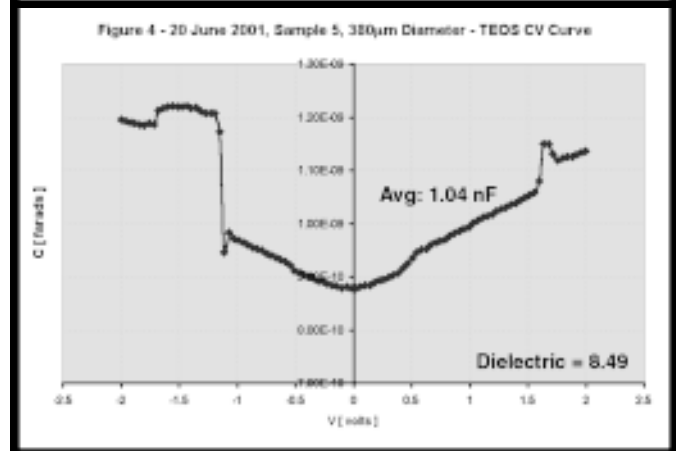
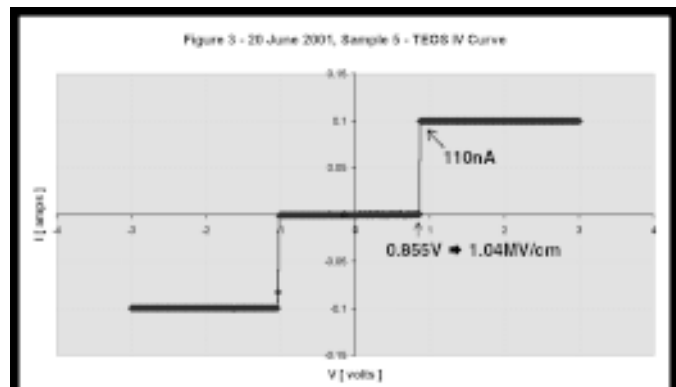
The TEOS devices produced both breakdown and capacitance measurements. The breakdown fields were 1-2 MV/cm. Figure 3 shows a field of 1.04 MV/cm (device thickness: 82 Å) when the current is 110 nA at the point before breakdown. These values are much lower than the actual values, 9-12 MV/cm, for gate-oxide in MOSFETs, but the calculated dielectric values were close to the actual dielectric values of gate oxide — 3.9. Two different dielectric values were found from two different sized devices. Fig. 4 shows a CV curve for a 380 μ m diameter device. Three CV curves were measured on this device, the average capacitance was thus 1.04 nF, which yields a

dielectric constant of 8.49. This value is more than twice the actual value for gate oxide, but on the same order of magnitude. The other device measured was a 625 μ m device. Its measured capacitance was 1.24 nF, which gives a dielectric constant of 3.7. This value is close to and lower than the actual value, but different from the other dielectric constant found.

These errors and problems with shorted devices could be due to errors in the devices and in measurement techniques. Variance in the two dielectric constant values could be due to the use of theoretical measurements of the device area in calculations — the device areas were found using scanning electron microscopy (SEM) on the actual shadow mask and not by measuring the actual devices. The probe touching ML2 might have pushed down on the metal and shorted the devices. The shorts may also be caused by metal spiking through the films. Though the device characteristics measured are varying, the fact that characteristics are measurable and on the same magnitude is helpful in further developing the fabrication processes of these devices. These studies give promise the fabrication and testing of metal-molecule-metal structures in the future.

Acknowledgements:

Thank you to: Tad Daniel for valuable help and training; Prof. Allara, the Allara Group, Lisa Daub, Debbie Boyle, David Conklin, Mark Horn, and everyone else at MRI for their support; Heather Russell, Teresa Bixby, Mike Papiak, and Arthur Carter for keeping me entertained inside and outside MRI.



Fabrication and Superconductivity of Ge/Ag/Ge Nanowires

Heather Russell, Physics, Pacific Lutheran University, russelhl@plu.edu

Principal Investigator(s): Ying Liu, Physics, PSU, liu@phys.psu.edu

Mentor(s): Mari-Anne Rosario, Physics, PSU

Abstract:

Multilayer structures of Ge/Ag/Ge have been previously found to exhibit superconducting precursors at liquid He temperatures. As neither Ge nor Ag is superconducting at atmospheric pressure, any effects of superconductivity must be due to phenomena occurring at the Ag-Ge interface. Such a truly two-dimensional (2D) superconducting system is a unique structure in which to study the nature of the superconducting state in one-dimension (1D).

In this study, structures of Ge/Ag/Ge were fabricated using electron beam lithography, and characterized using atomic force microscopy (AFM). As a comparison, larger 2D Ge/Ag/Ge films were also fabricated simultaneously. Initial electrical transport studies of the larger films indicated that the conductance is dependent on the thickness of the Ag layer. Low temperature electrical transport studies on both nanowires and 2D films are currently under way.

Introduction:

Superconductivity at semiconductor-metal interfaces was theorized in 1973 by Allender, Bray and Bardeen [1] but has never been observed. This study predicts that interface superconductivity will be an exotic type of superconductor arising from exciton excitation rather than the more widely studied phonon excitation. To see this

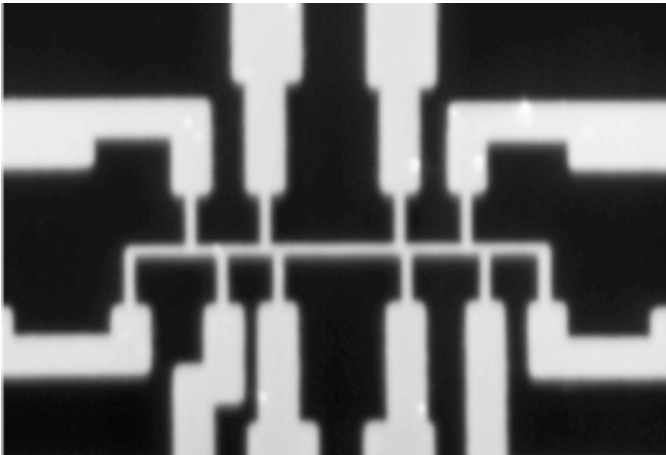


Figure 1. AFM image of dc four-point probe current (I) was run through the wire and voltage (V) was measured through two adjacent leads.

effect, use of a narrow-gap semiconductor is recommended. Ge, a semiconductor, and Ag, a noble metal, are excellent materials for this study. Previous in situ structural measurements of Ge and Ag using low energy electron diffraction (LEED) and Auger electron spectroscopy (AES) do not show any evidence of alloying at room temperature [2, 3]. So, the interfaces in the Ag-Ge sandwich are smooth and distinct. Also, neither Ge nor Ag is superconducting by itself at atmospheric pressure [4]. Therefore any superconductivity that is observed must occur at the Ag-Ge interface. Superconducting fluctuations have been previously seen in Ge/Ag/Ge structures at minimum temperatures of 0.5K, but zero resistance has not been observed [3, 4].

Interface geometry provides us a structure with which to study a genuinely 2D superconducting system. By narrowing the width of the films, 1D can be approached. This study makes use of nanowires to approximate 1D. We hope to look for novel phenomena that may occur as the sample size decreases.

Procedure:

Ge/Ag/Ge nanowires were fabricated using electron beam lithography. The structures were designed to accommodate a dc four-point probe measurement technique with wire lengths of 100 nm to 2 μ m. (Figure 1) A non-conducting substrate of quartz or sapphire was coated with a bilayer resist of MMA-MAA (nominally 420 nm thick) and PMMA (120nm). A conducting surface layer of 100 \AA of Au was evaporated onto the bilayer. This layer is necessary to conduct electrons from the surface during the e-beam exposure. A single pass e-beam write was used to obtain the smallest wire possible. The Au layer was then etched and the resist was developed in MIBK and IPA. Ge/Ag/Ge films were evaporated: Ge was evaporated using an electron gun source and Ag was evaporated thermally. The thickness of the Ge layers was 50 or 100 \AA and the Ag layer was 20, 30, 40, or 50 \AA thick. Acetone was used to liftoff the resist layers and the excess film. Finally, characterization of the samples was done using AFM. The narrowest wire fabricated for this project was \approx 100 nm. For comparison, larger 2D Ge/Ag/Ge films were simultaneously evaporated with the nanowires using a shadow mask technique.

Discussion:

Preliminary results for 2D films suggest that the conductance is highly dependent on the thickness of the Ag layer. (Figure 2) With a 20 Å Ag layer, the resistance vs. temperature curve looks much like we would expect if looking at a structure of only Ge. Thicker Ag layers exhibit characteristics typical of conductors. 30 Å of Ag appears to be the minimum amount of material for the sample to be metallic.

Electrical transport studies of both 2D films and nanowires of Ge/Ag/Ge are ongoing. The samples are currently being cooled in a 3He Cryostat with a base temperature of 0.3K. In the future, 1D effects will be further studied with narrower nanowires and colder temperatures.

Acknowledgements:

I would like to thank Mari-Anne Rosario for her help with this project, Ying Liu for his advice and Beth Hutchinson for collaborating with me on this work. Also, I would like to thank Mike Rogosky, Ed Basgall, Lisa Daub, Debbie Boyle, and all the other REU students for their support.

References:

- [1] D. Allender, J. Bray, and J. Bardeen, Phys. Rev. B 7, 1020 (1973).
- [2] Massalski, T. B., ed. Binary Alloy Phase Diagrams, Second Ed., Vol. 1, 1990, 39-42.
- [3] M. J. Burns, J. R. Lince, R. S. Williams, and P. M. Chaikin, Solid State Commun. 51, 865 (1984).
- [4] Y. Liu, B. Nease, and A. M. Goldman, Phys. Rev. B 45, 10143 (1992).

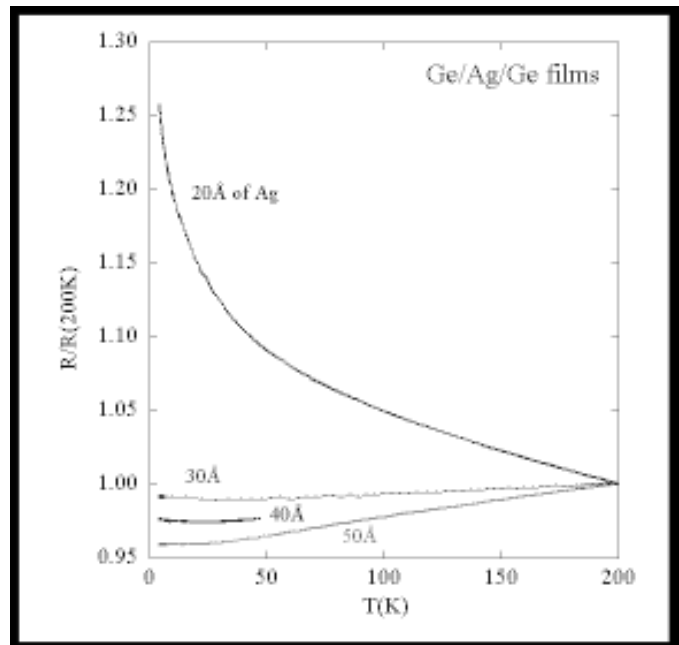


Figure 2. Preliminary electrical transport studies of 2D films with varying Ag thickness.

Nanoscale Patterns and Networks made by Molecular Rulers Grown on Dot Arrays formed by Nanosphere Lithography

Alexander D. Wissner-Gross, Mathematics / Physics / Electrical Engineering,
Massachusetts Institute of Technology, alexwg@mit.edu

Principal Investigator(s): Paul S. Weiss, Dept. of Chemistry,
The Pennsylvania State University, stm@psu.edu

Mentor(s): Guy Lavalley, Anat Hatzor, Penn State Nanofabrication Facility, PSU

Abstract:

The recent development of the molecular ruler nanofabrication process has enabled the creation of very closely spaced metal structures with positional accuracies of 1 nm. This process may be useful for molecular electronic measurements, as it could allow the fabrication of electrodes with spacing that precisely matches the length of a particular functional molecule. We present a new method for creating an array of molecular ruled gaps between Au and Ti particles and a continuous network of metal on a SiO₂ substrate. A hexagonally-packed monolayer of polystyrene nanospheres was used as a mask for metal evaporation onto the substrate. After evaporation, dissolution of the nanospheres left an array of triangular metal particles on the SiO₂, which were then used as a parent structure for the molecular ruler process. This network and isolated pattern array formation has potential applications for the fabrication of large scale molecular electronic devices.

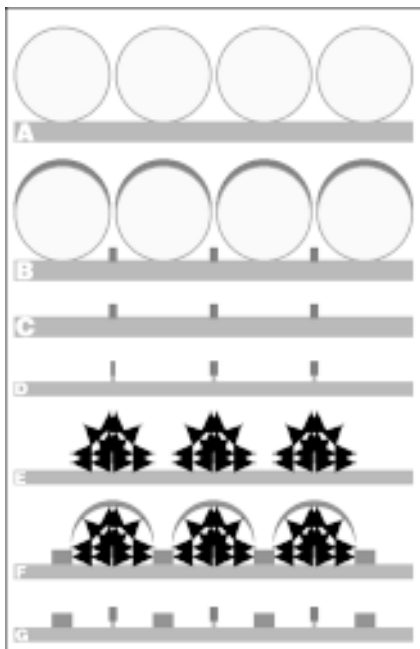


Figure 1: Ruled nanosphere lithography scheme. (A) Nanospheres deposited on SiO₂ surface. (B) Metal evaporation into the layer gaps. (C) Dichloromethane dissolution of nanospheres. (D) Silicon etching to enhance molecular ruler process. (E) Construction of metal-organic multilayer resist. (F) Second metal evaporation. (G) Dissolution of multilayer in HCl/DMF solution.

Introduction:

Fabrication of periodic arrays of sub-100 nm metal structures on surfaces has proven useful in optical filtering [1], magnetic storage [2], biological probes [3], and molecular electronics [4]. Much effort has been directed toward finding methods for creating these structures that combine the resolution of electron-beam lithography with the parallelism of extreme ultraviolet lithography. One particularly inexpensive method is nanosphere lithography (NSL) [5-8], which uses a monolayer or bilayer of spheres as a porous deposition mask for a large set of materials [7]. Although nanosphere lithography has been used to produce several different classes of metal particle patterns, the smallest reproducible gaps [8] between particles has only been 165-nm. The introduction of molecular rulers [9] as a means for constructing fine nanowires by quantitatively scaling down the gap between electron beam-produced electrodes, offers a way to extend the capability range of NSL.

Methodology:

Our method for fabrication of Au particle arrays differs from previous NSL procedures, notably in our use of reactive ion etching. Suspensions of non-functionalized polystyrene sphere of diameters 160 nm and 400 nm were obtained from Bangs Laboratories. The received nanosphere suspensions were diluted by a 1:400 solution of the surfactant Triton X-100 (Sigma-Aldrich) in methanol. In accordance with previous work [8], the respective dilution factors were 1:6 and 1:1. After dilution, the nanosphere suspensions were spin-coated onto isopropanol-cleaned SiO₂ wafers with areas between 0.5- and 2.0-sq-cm. The spin-coater (Headway Research Inc., Model No. CB15) was operated at ~900 rpm for 160 nm spheres and ~500 rpm for 400 nm spheres for 2 minutes to obtain monolayers. Excess fluid at the perimeter of the wafers was removed using LABOX Cleanroom Wipers (Berkshire Corp.). Reactive ion etching was then performed (Plasma-Therm 720 RIE, SLR Series) in order to remove surfactant solution remaining in interstices of monolayer spheres, a step not taken in previous works. The monolayer was used as a mask (Fig. 1), first for electron gun evaporation of a 5 nm Ti underlayer, then for thermal evaporation of a 5nm Ti

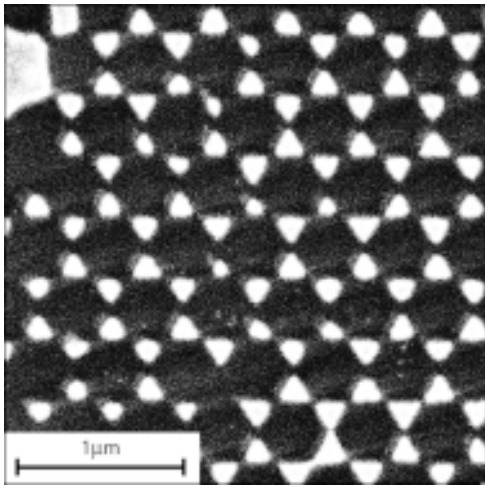


Figure 2: Field-emission SEM image of array of layered Au/Ti particles formed by evaporating the metals through holes in a hexagonally packed 400 nm nanosphere mask. (Performed on a Leica LEO 1530 FESEM)

layer followed by a 30 nm Au layer (Kurt J. Lesker Company E-gun/Thermal Evaporator). Subsequent removal of the nanospheres by sonication in CH_2Cl_2 (J. T. Baker) for 2 minutes left a hexagonal arrangement of ~ 150 nm or ~ 25 nm metal particles on the substrate (Fig. 2). A 1 min CF_4/O_2 RIE plasma step was taken to etch $\sim 400\text{\AA}$ of SiO_2 from the surface. This step was carried out in order to improve the lift off profile for the removal of the organic layers.

Coordinated metal-organic multilayer resists [10] were applied to the metal nanoparticles, by alternate deposition of 2 nm long mercaptoalkanoic acid molecules and Cu^{2+} ions (14). After application of 10 such layers, a second layered metal deposition of 4.5 nm Ti and 4.5 nm Au was performed. Samples were then sonicated in a warm solution of 0.06 M HCl in 75% dimethylformamide to remove both the multilayer and the metal deposited on top of the multilayer.

Results and Future Work:

Preliminary results of the ruler application were encouraging (Fig. 3B). The resists adsorbed onto the substrates conformally beyond 10 layers. Even with 20 layers, while the geometry of the original gold islands becomes obscured, the hexagonal lattice remains. Deposition of the secondary metal also proceeded as expected. However, our first attempt at resist liftoff was unsuccessful, and is the subject of our current work.

Acknowledgments:

The authors are grateful to the PSU Materials Research Institute staff for sharing their equipment and suggestions. We thank Mark Horn for helpful discussions. This work was partially funded by the NSF National Nanofabrication Users Network and Intel Research.

References:

- [1] Flaugh, P. L.; O'Donnell, S. E.; Asher, S. A. *Appl. Spectrosc.* 1984, 38, 847.
- [2] Chou, S. Y. *Proc. IEEE* 1997, 85, 652.
- [3] Baselt, D. R.; Lee, G. U.; Hansen, K. M.; Chrisey, L. A.; Colton, R. J. *Proc. IEEE* 1997, 85, 672.
- [4] Andres, R. P.; Bielefeld, J. D.; Henderson, J. I.; Janes, D. B.; Kolagunta, V. R.; Kubiak, C. P.; Mahoney, W.; Osifchin, R. G. *Science*. 1996, 273, 1690.
- [5] Deckman, H. W.; Dunsmuir, J. H. *Appl. Phys. Lett.* 1982, 41, 377.
- [6] Deckman, H. W.; Dunsmuir, J. H. *J. Vac. Sci. Technol. B.* 1983, 1, 1109.
- [7] Hulteen, J. C.; Van Duyne, R. P. *J. Vac. Sci. Technol. A.* 1995, 13, 1553.
- [8] Hulteen, J.C.; Treichel, D. A.; Smith, M. T.; Duval, M. L.; Jensen, T. R.; Van Duyne, R. P. *J. Phys. Chem. B.* 1999, 103, 3854.
- [9] Hatzor, A.; Weiss, P. S. *Science*. 2001, 291, 1019.
- [10] Evans, S. D.; Ulman, A.; Goppert-Berarducci, K. E.; Gerenser, J. L. *J. Am. Chem. Soc.* 1991, 113, 5866.

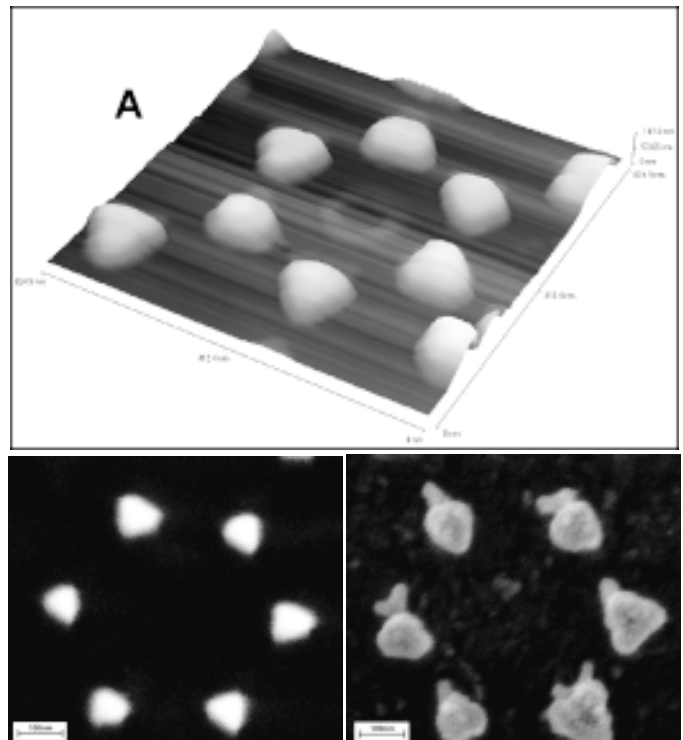


Figure 3: (A) Atomic force micrograph of a single cell in the metal particle array (400nm sphere diameter), before application of molecular ruler process. (B) FESEM image of a single cell after application of 0, 10, and 20 layers of the 20-nm molecular ruler.

**Stanford Nanofabrication Facility
Stanford University, Stanford, CA
<http://www-snf.stanford.edu/>**

2001 REU Interns



REU Intern School Affiliation Principal Investigator

Front Row:

Mr. Noel Jensen Colorado College Peter Griffin

Second Row, L to R:

Mr. Andrew Davenport Washington University, St. Louis Fabian Pease and Dan Pickard

Ms. Sondra Hellstrom Johns Hopkins University Steven Boxer

Ms. Samar Hubbi New Jersey Institute Mary Tang

Ms. Marina Sofos Brown University Bruce Clemens and Mark Phillips

Ms. Kate Klein Trinity College Fabian Pease and Dan Pickard

Mr. Noah Beck Harvey Mudd College Kathryn Mohler

Back Row, L to R:

Dr. Michael Deal Stanford Nanofabrication Facility SNF REU Coordinator

Ms. Linda Ohsie Dartmouth College Mary Tang

Ms. Aileen Chang UC Berkeley Hongjie Dai

Mr. Jonathan Schuller UCSB Peter Griffin

Ms. Natalie Lui Harvard University Blas Cabrera and Paul Brink

Mr. Nathan Morris Messiah College Hongjie Dai

Electron Beam Lithography of Nanoscale Hall Probes for Scanning Microscopy

Noah Beck, Physics, Harvey Mudd College, nbeck@hmc.edu

Principal Investigator(s): Kathryn Moler, Applied Physics,
Stanford University, kmoler@stanford.edu

Mentor(s): Janice Wynn, Physics, Stanford University

Abstract:

The study of magnetism is central to understanding many physical systems. Small, sensitive magnetic probes allow us to study magnetic domains, flux vortices in superconductors, magnetic nanoparticles, and other systems. One non-invasive way of doing so is with a scanning Hall probe, which measures the local magnetic field at many points on the sample surface, producing a magnetic field image. The size of the active region of the Hall probe governs the spatial resolution of the image. We designed and fabricated the smallest working scanning Hall probe possible on a GaAs/AlGaAs two-dimensional electron gas (2-DEG) heterostructure using electron beam lithography. The size of the active region was reduced from its current micron-scale to 200 nm.

Introduction:

One very important part of studying advanced materials is studying their magnetic properties. More specifically, we can learn a lot about a material by mapping its magnetic field as a function of position on the material's surface. One way of creating such a map is with scanning Hall probe microscopy. A Hall probe

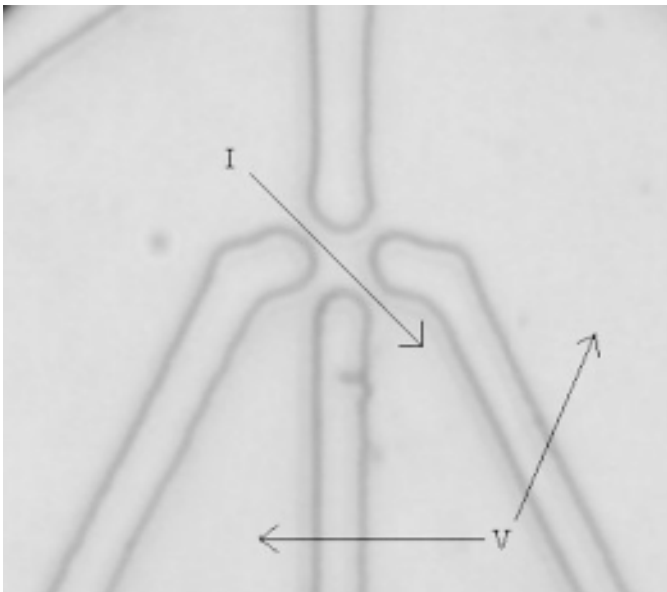


Figure 1: Hall probe: current flows across the active area, and voltage is measured perpendicular to current.

measures the magnitude of the perpendicular component of the magnetic field at a point just above the surface of the material, then proceeds scanning across the material taking measurements until the map is created. It uses a conducting cross made with a two-dimensional electron gas (2-DEG) to measure magnetic field. Figure 1 shows an optical photograph of a two micron Hall probe currently being used by the Moler Group at Stanford University.

As charge carriers move through the magnetic field, they shift to one side of the two-dimensional wire, creating a bias potential across the other two leads, which is directly proportional to the average magnetic field across the active region.

With further research being done in solid state physics and the physics of materials, it is becoming increasingly important to have better spatial and magnetic resolution in measurements of local magnetic fields in order to better scrutinize magnetic phenomena. One way of improving the spatial resolution of a Hall probe is simply to make it smaller. Because it can only measure the average magnetic field across its active area, decreasing the size of the active area not only improves the resolution of the magnetic image obtained, but enables it to see smaller quantities of magnetic flux that would have otherwise been washed out with a larger active region.

Procedure:

Because 2-DEG is very expensive, we used gallium arsenide pieces to perfect the lithography and etching techniques before building the final Hall probes on real 2-DEG, which is formed in a GaAs/AlGaAs heterostructure. ZEP 520-12 positive resist was spun on to the GaAs at 6500 RPM for a thickness of approximately 150 nm and exposed using an electron beam lithography machine. A proximity correction program called Caprox was used to assign different electron doses to different areas of the design based on how the beam exposes the resist in its close proximity.

The distribution of exposure is a double Gaussian function of the distance from the center of the electron beam including the terms: the forward scattering term α ; the backscattering term β ; and η , which relates the forward scattering exposure to the backscattering

exposure [1]. The double Gaussian parameters we found to work most effectively for our resist/substrate/beam voltage combination were $\alpha = 20\text{nm}$ $\beta = 1500\text{nm}$ and $\eta = 0.99$.

The pattern was exposed at a dose of $150\text{mC}/\text{cm}^2$. The sample was then developed for 20 seconds in Xylenes and rinsed with Methyl iso-butyl ketone and isopropyl alcohol mixed 1:2. We permanently etched the pattern into the gallium arsenide using a plasma etch to a depth of approximately 26 nm, deep enough to etch away the top layer of positively doped gallium arsenide required to form the two-dimensional electron gas, thus depleting the area of 2-DEG just beneath the etch. The ZEP resist was removed with N-Methyl-2-Pyrrolidone and the samples were examined using a scanning electron microscope.

Results:

It was found that although minimum beam size of the ebeam machine was 50nm, feature sizes reached a minimum of 200 nm with a minimum interspacing of 200 nm due to the large backscattering coefficient of GaAs. Figure 2 shows a finished Hall cross on a piece of gallium arsenide.

Once the above procedure is performed on the 2-DEG, contact pads will be added to the four leads of the cross to provide contact points on which to solder wires, and a deep mesa etch will cut the probes out of the material. The current Hall probes being used by the Moler group that were made using optical lithography techniques are $2\ \mu\text{m}$ on a side. The new recipe will yield active areas 100 times smaller, dramatically increasing spatial resolution and magnetic accuracy of the scanning Hall probe.

Acknowledgements:

Special thanks to: Kathryn Moler, Janice Wynn, Yu-Ju Lin, David Kisker at IBM, the NNUN, and NSF funding.

References:

- [1] "Proximity Correction for Electron Beam Lithography using a Three-Gaussian Model of the Electron Energy Distribution", S.J. Wind, M.G. Rosenfield, G. Pepper, W.W. Molzen, and P.D. Gerber: J. Vac. Sci. Technol. B 7 (6), Nov/Dec, p1507, 1989.

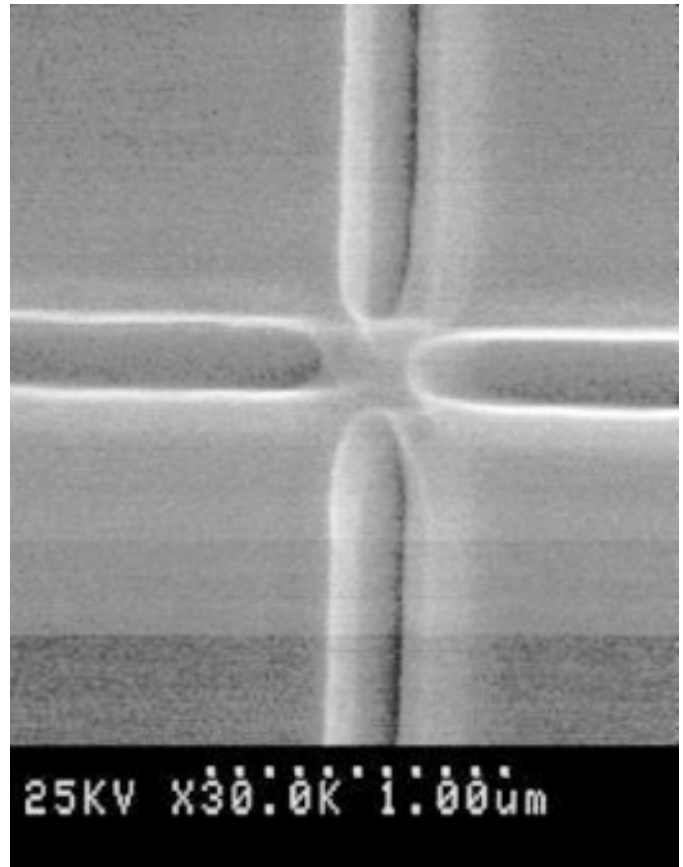


Figure 2: Hall probe with active area of 200nm on a side.

Integration of Nanotubes into Devices

Aileen Chang, Physics, U.C. Berkeley, aileenzzz@hotmail.com

*Principal Investigator(s): Hongjie Dai, Chemistry,
Stanford University, hdai1@Stanford.edu*

*Mentor(s): Yeugang Zhang, Qian Wang, Nathan Franklin,
Chemistry, Stanford University*

Abstract:

Controlled growth of nanotubes is necessary to integrate them into practical devices. We attempted to grow nanotubes into a criss-cross-patterned array, geometrically and functionally similar to current memory arrays. Using chemical vapor deposition (CVD) and an electric field, single-walled nanotubes (SWNTs) were grown from an elevated poly-Si surface onto a quartz surface in an aligned manner. Observations of nanotubes using a scanning electron microscope (SEM) and theoretical calculations have shown that alignment is due to the high polarizability of SWNTs and that an electric field of 1-2 V/ μm is necessary to align suspended nanotubes and overcome randomization from thermal vibrations and gas flow in the CVD process.

Introduction:

Single-walled nanotubes, pure carbon cylinders, are examined because of their unique electrical property of being perfect quantum wires. Because nanotubes are highly polarizable, we used an electric field to align their growth. To justify the use of an electric field, we calculated the various forces that act upon the nanotube in addition to the force due to the electric field, such as gas flow in the CVD chamber and thermal vibrations of the nanotube.

Procedure:

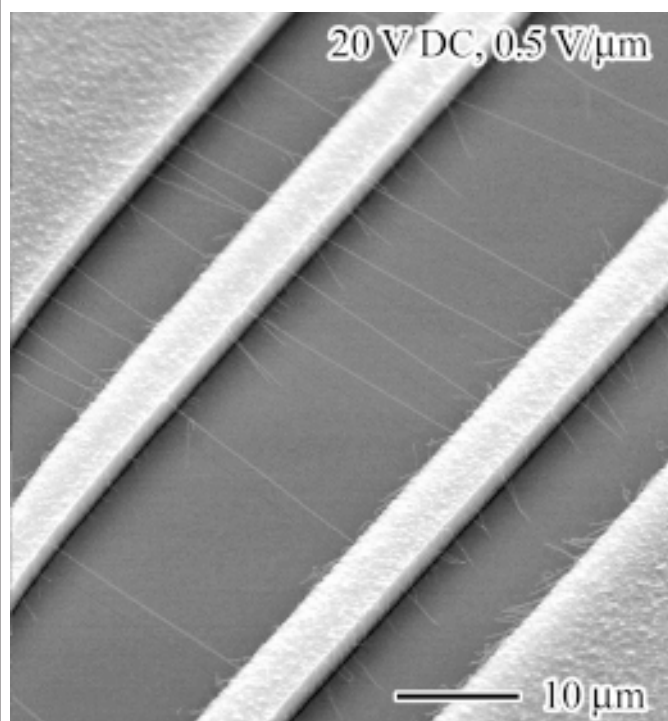
Nanotubes were grown using chemical vapor deposition with methane or ethylene gas. SiO₂/poly-Si wafers were made using standard nanofabrication procedures. The dimensions of an individual chip on the wafer were 7 mm by 7 mm with an X-patterned trench measuring 1 mm in width and 2 μm in depth. An inner square trench measuring 50 μm by 50 μm also had a depth of 2 μm . Hence, each chip was divided into four electrically insulated sections. Electrodes were placed on these sections of poly-Si and the chip was placed in a CVD chamber in which methane gas was flowed at a temperature of 900°C.

To justify the alignment of nanotubes via use of an electric field, we examined the effects on alignment of methane flow and thermal vibrations compared to the effects of the electric field on nanotube growth.

In order to examine the effects of methane flow, we approximate a nanotube with a long rectangle with dimensions $d \times d \times l$ where d is the diameter and l is the length of the nanotube. Assuming that the gas flow is laminar in the CVD chamber, and that all gas flows perpendicular to the nanotubes, we can calculate the force due to methane flow using Newton's equation of motion, $\mathbf{F} = m\mathbf{a} = m(\mathbf{v}/t)$, and the ideal gas law, $PV = nRT$, from which we obtain the density and hence, the mass of the gas. We found that $F = (mP/RT)ldv^2$ where v is the rate of flow of methane.

Another force examined was that due to thermal vibrations in an electric field, which is especially important at the high growth temperature of 900°C. We modeled the nanotube as a flexible, hollow rod of inner radius α and outer radius β with oscillation amplitude σ at which the rod is an angle θ from its rest position.

We then use conservation of energy to deduce $\alpha E^2 + kT/2 = \alpha E^2 \cos^2\theta + (1/2)\sigma_E^2 c$, where α is the polarization of the nanotube, k is Boltzmann's constant, and c is the



SEM image of SWNTs aligned by E-field.

constant of elasticity for the nanotube [1]. Using the approximation $\sin\theta \approx \theta \approx \sigma_e/L$ for small oscillations, we can solve the aforementioned equation for the oscillation amplitude: $\sigma = 1[kt / (2\alpha E^2 + cl^2)]^{1/2}$ where $c = 38.8T(a^4 - b^4) / 16L^3$. Using $F = kT/\sigma$, we can determine the force of thermal vibration on the nanotube in an electric field.

We then examined the strength of force due to the applied electric field. Force due to an E-field is qE and $q = \alpha \cdot E/l$ where $\alpha \cdot E$ is p , polarization. Letting θ be the angle between the nanotube and the applied electric field, we determine the force due to the applied voltage to be $\alpha E^2 \sin\theta \cos\theta$.

Results and Conclusions:

From above, force due to laminar flow is $(mP/RT)ldv^2$, force due to thermal vibrations in the electric field is kT/σ where $\sigma = 1[kt / (2\alpha E^2 + cl^2)]^{1/2}$, and force due to the applied electric field is $\alpha E^2 \sin\theta \cos\theta$. For a nanotube representative of those observed in our experiments with a length of 20 μm and a radius of 1 nm in an electric field of 1V/ μm , $F_{\text{laminar flow}} \approx 10^{-7}\text{nN}$, $F_{\text{thermal}} \approx 10^{-5}\text{nN}$, and $F_{\text{E-field}} \approx 1\text{nN}$. The predicted thermal vibration amplitude is about 0.4 μm . Hence, laminar flow plays a very minor role in influencing the growth of a nanotube.

We were only able to complete the design of the silicon wafer and grow one set of parallel-aligned

nanotubes rather than a completed pattern of crisscrossing nanotubes. However, previous samples of nanotube growth confirmed our prediction that laminar flow has a minimal effect on nanotube growth. Experiments have also shown that to optimize growth, an electric field of 1-2 V/ μm is ideal.

Further factors to be examined include the effect of van der Waal's interactions between nanotubes, and between nanotubes and the growth substrate; possible turbulence in the CVD chamber; as well as effects of the induced voltage from field emission, which have been postulated to cause a much higher external field than that from the applied voltage.

Acknowledgements:

I would like to thank Nathan Morris, fellow SNF REU student, who was essential to the experimental portion of this project, my mentors and Professor Dai for their invaluable advice and support, and the NSF for funding for such an enriching summer experience.

References:

- [1] Krishnan, A., E. DuJardin, T.W. Ebbesen, P.N. Yianilos and M.M.J. Treacy. "Young's Modulus of Singlewalled Nanotubes." *Physical Review B*. November 1998. Vol. 58 No. 20. pp. 140113-14019.

Alignment System of Distributed Axis Multiple Beam Electron Lithography

Andrew Davenport, Mechanical Engineering, Washington University in St. Louis,
aad3@cec.wustl.edu

Principal Investigator(s): Fabian Pease, Electrical Engineering,
Stanford University, pease@cis.stanford.edu

Mentor(s): Dan Pickard, Electrical Engineering, Stanford University

Abstract:

Large parallel arrays of electron beams may provide orders of magnitude faster production than current single beam systems. One of the primary difficulties with such a system is the alignment of the many adjacent beamlets. Each beamlet must be mechanically positioned to within a few microns accuracy to enable finer electronic alignment. Our system will be further complicated by the requirements that all parts must: be non-magnetic to maintain a uniform magnetic field, have no outgassing properties to achieve an ultra high vacuum, and operate in a volume of 27 cubic centimeters. Our goal is to design and integrate a system of commercial piezomotors and drive mechanisms to control the many degrees of freedom required to align the arrays

Introduction:

Optical lithography at high resolution (sub 100 nm) is difficult and entails large risks and costs. Many candidates for overcoming this problem are being investigated including: single shaped electron beams, ion beams, and multiple electron beams [1]. Single electron beam lithography systems are forever fighting the antagonistic effects of writing speed (greater current) and feature resolution (less beam blur). A distributed axis system uses independent parallel beams to write on a sample, much like a dot matrix printer. The system is compact and relatively simple, only using 4 elements to

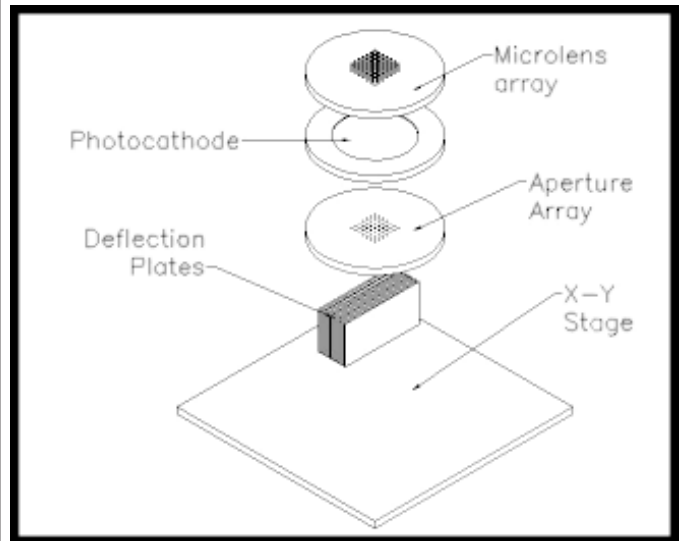


Figure 2. Schematic of multiple beam experiment.

manipulate the beams. If such a system is successful, it will offer the throughput of current optical lithography but with increased resolution and at a fraction of the cost [2, 3].

Theory:

The distributed axis variable shaping system (or DIVA) guides the array of beamlets using a uniform magnetic field parallel to the electron path. The electrons follow a helical path down to the sample, as given by the equation $F=q*v \times B$. This provides a unity focus (1:1) for the beam and axially constrains the electron path. The system is placed inside a vacuum vessel and positioned between two pole pieces, which provide a .33 Tesla uniform magnetic field down through the chamber.

In order to characterize this focusing method, a single electron beam system was constructed. A LaB_6 cathode at 30 kV accelerates electrons down to 50 nm aperture. From the aperture, the electrons are directed using an octopole — an element with 8 electrostatic plates which deflect the beam. The beam then writes on a sample and imaging is done through secondary electron detection using a microchannel plate (above the sample) and transmission electron detection using a standard photodiode (below the sample).

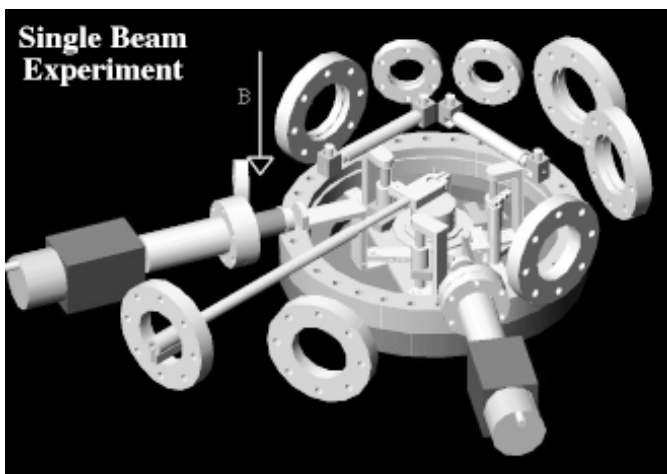


Figure 1. Single beam experiment, chamber omitted for clarity.

Procedure:

Once the single beam system is analyzed and understood, the multiple beam system will be constructed. The multiple beam system has the more stringent requirements of all elements (including the chamber) being UHV compatible (does not outgas) and non-magnetic. In addition, the vertical distance of the elements cannot exceed 90 mm due to the pole piece separation.

A major concern of the multiple beam system is aligning the microlens array with the grid of apertures. Both elements need a number of degrees of freedom. The microlens array is connected to the top of the chamber by metal bellows that allow for a range of motion. The microlens must be mobile in the X, Y, and Z directions. By using three vertical clamps on the perimeter, tilt can be adjusted as well as the Z position. The aperture grid must be mobile in the Z direction and rotate in the X-Y plane.

The necessary mobility for alignment was provided with piezo-electric linear translating motors. These motors are about the size of a matchbox and can operate in steps on the nanometer scale. Each motor has a small projecting finger which is pressed against a ceramic race. By exploiting a disparity in static and dynamic friction the finger “grabs” and “pulls” along the race to produce a one-dimensional motion.

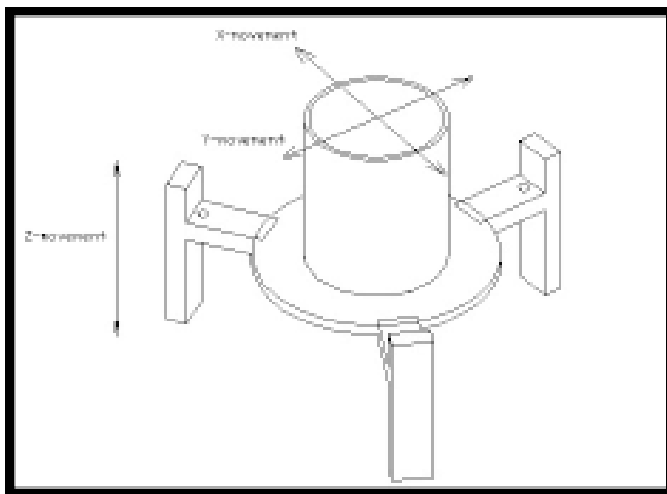
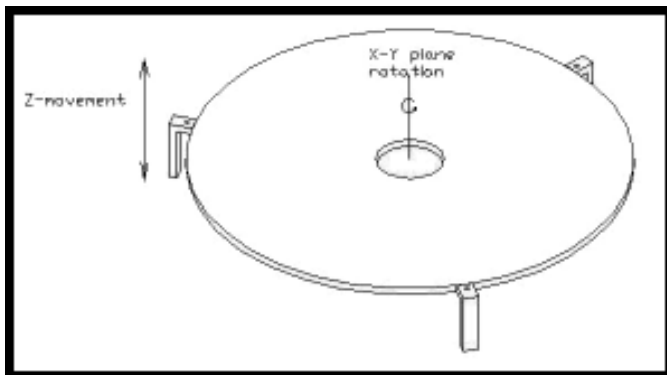


Figure 3, above. Microlens array degrees of freedom.
Figure 4, below. Aperture grid degrees of freedom.



The three types of motion for the microlens were accomplished by nesting three relative reference elements. The entire alignment system moves relative to the chamber in the X direction. Quartz guide rails and Rulon sleeve bearings are used to allow for a one-dimensional motion. Below the top X platform is another parallel Y platform that is translated in the Y direction using the rail-bearing system as before. Piezomotors are fixed to the Y platform and are positioned to raise and lower the three clamps on the microlens array mount thus achieving the Z mobility.

Aperture alignment is done in a similar fashion, using three piezomotors fixed to the bottom of the chamber to raise and lower the aperture platform. A fixed piezomotor mounts on the platform to rotate the aperture holder along its circumference. This motion is allowed by placing the aperture holder within the space between two Rulon sleeve bearings.

Figure 5 illustrates the assembly of the elements. The middle element, the photocathode, mounts on the bottom of the chamber. The beige box is the X-Y sample stage, which also houses the deflector plates.

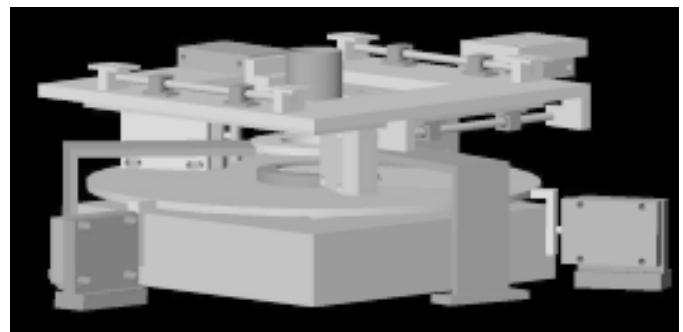


Figure 5. Multiple beam assembly.

Future Work:

After results from the single beam experiment, assembly will begin on the multiple beam system. Using this fully flexible prototype for the alignment system, interferences and assembly issues can be addressed. Future work will need to finish the chamber design and manufacturing. With the alignment system in place, future integration of parts will be easier and a greater overall perspective gained.

Acknowledgements:

I would like to thank my mentor Dan Pickard for his aid and guidance during the project.

References:

- [1] R Pease, L Han, G Winograd, & W Meisburger, “Prospect of Charged Particle Lithography as Manufacturing Technology.” *Microelectronics Engr*, 53, pp. 55-60, 2000.
- [2] TR Groves and RA Kendall, *JVST*, B16, 3168 (1998).
- [3] T.H. Chang, et al, “Multiple Electron-Beam Lithography.” located at: http://www.appliedmaterials.com/products/etec_tp.html.

Development of a Microfluidic System for Separation of Lipids with Various Composition Ratios

Sondra Hellstrom, Electrical Engr and Physics, Johns Hopkins University,
SondraH@jhu.edu

Principal Investigator(s): Dr. Steven G. Boxer,
Department of Chemistry, Stanford University, sboxer@stanford.edu

Mentor(s): Dr. Lance Kam, Department of Chemistry, Stanford University

Abstract:

We are developing electrophoresis-based techniques for microscale separation of membrane-associated biomolecules incorporated into fluid, supported lipid bilayers. Our goal is to separate and manipulate very small quantities of sample. Methods for forming, applying electric fields across, and physically addressing fractional parts of bilayer patches on the order of hundreds of microns need to be developed. Here, we implement microfluidic networks for manipulating such membranes using poly(dimethylsiloxane) (PDMS) elastomer on glass.

Introduction:

Supported lipid bilayers provide a unique system for modeling biological membranes [1, 2]. Recently developed techniques for micropatterning membranes provide a new tool for the study of supported lipid bilayers [3, 4]. A convenient method to separate bilayer components would facilitate their study and provide the foundation for preparative methods. Charge-based separations can be done via electrophoresis, in which electrodes are used to apply an electric field across a

bilayer patch [5] measuring hundreds of microns on a side. Because of the fluidic nature of these systems, electrophoretically induced separations relax relatively quickly, hampering collection of purified membrane components. Permanent separation and collection of various membrane components can theoretically be achieved via laminar flow of a solvent over a bilayer into diverging channels (Figure 1).

The channels exploit the laminar flow characteristic of microfluidics networks. Design components include a central 400- μm space for a bilayer, an inflow channel, two orthogonal channels for voltage application, and five smaller branches for bilayer separation and collection. The entire system is about 11 mm, with each large channel about 400 μm by 54 μm , and each small channel, at its narrowest, 125 μm by 54 μm .

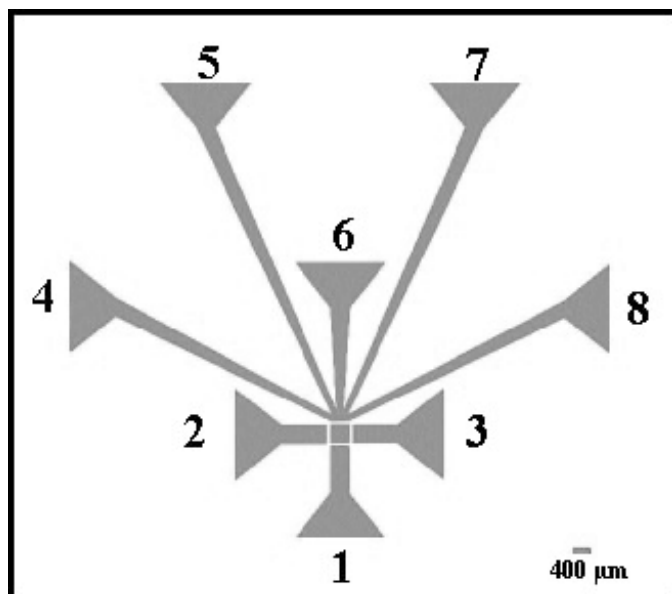


Figure 1: Design of microfluidic network. Channel 1 is for input, 2 and 3 for electrophoresis, and 4-8 for separation and collection.

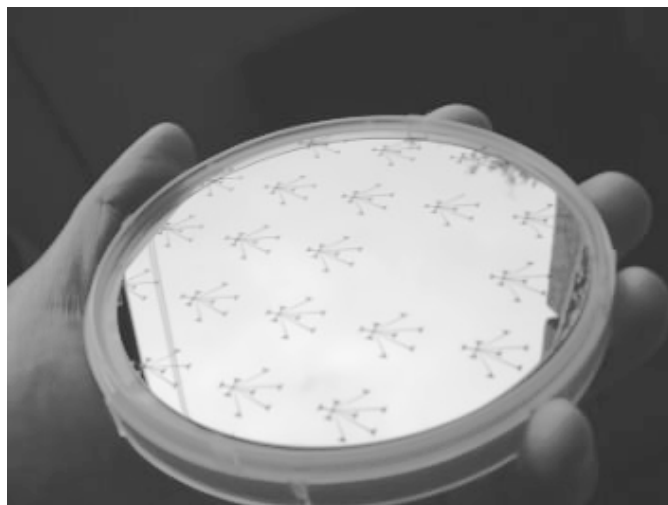


Figure 2: Hard channel mask on silicon.

Materials and Methods — Microfabrication:

Microscale PDMS channels were created using soft lithography techniques. Hard inverse masters of the channel network, shown in Figure 2, were created via standard photolithography. Silicon wafers were primed with hexamethyldisilazane (HMDS), and coated with 54 μm of photoresist in three layers. The wafers were selectively exposed to UV radiation, developed, and coated by vapor deposition with a second layer of HMDS.

PDMS was poured on the mold and cured at 60°C for 90 minutes. Holes were punched into the channel ends for material collection. The PDMS was degreased for thirty minutes in dichloromethane and subsequently heated to about 60°C for an hour. 100 microliters of 100 ml/ml crystallized bovine serum albumin (BSA) solution was deposited onto the channels for ten minutes, rinsed off and dried under nitrogen gas. To control bilayer formation, the inverse of a 400 μm square was stamped onto a glass slide [6]. The stamp was oxidized PDMS treated with dichloromethane and then coated with BSA. The glass was brought into contact with the stamp for 10 minutes under 100g weight, rinsed in deionized water and dried under N_2 . The PDMS channel was cleaned with acetone and methanol, dried under N_2 , and oxidized using an RF generator for 90 seconds. Its center was then aligned with the inverse stamped onto the glass slide. The slide and channels formed a seal.

Materials and Methods — Lipid Vesicles:

Small unilamellar vesicles of 1,2 Diacyl-SN-Glycero-3-Phosphocholine (DLPC; Avanti Polar Lipids, Alabaster, AL) with 1% negatively charged Texas Red-DHPE (Molecular Probes, Eugene OR) were prepared by extrusion. Vesicles at a concentration of 2.5 mg/ml in standard buffer (10 mM Tris and 100 mM NaCl, pH 8), were manually injected into the channels with a pipette, then rinsed extensively with water.

Results and Future Work:

The PDMS channels and the BSA patterning provided control over lipid bilayer deposition. Figure 3 is an example of successful flow control in which vesicles were injected into the uppermost channel and confined to the topmost three. Fluid bilayers formed in the central square region, as evidenced by fluorescence recovery after photobleaching (FRAP) experiments.

Future work concerns bilayer formation control inside the channels, perfection of the electrophoresis application, and introduction of more controlled input/output mechanisms. BSA stamping compromises the ability of the PDMS-glass seal. With no bilayer formation inhibitor, however, bilayers form throughout the network. Experimentation has been done, with some success, with channel blockage as shown in Figure 3, but the most promise seems to be alternate materials that do not impede seal formation. In addition, the practicalities of introducing electric fields for electrophoresis need to be explored. Finally, while manual injection and collection is adequate during the use of the microfluidic network, an automated system with more controlled pressures needs to be implemented.

References:

- [1] Sackmann E. Supported Membranes: Scientific and Practical Applications. *Science* 1996; 271:43-48.
- [2] Watts TH, and McConnell HM. Biophysical Aspects of Antigen Recognition by T Cells. *Ann Rev Immunol* 1987; 5:461-475.
- [3] Groves JT, Ulman N, and Boxer SG. Micropatterning of Fluid Lipid Bilayers on Solid Supports. *Science* 1997; 275:651-653.
- [4] Hovis JS, and Boxer SG. Patterning Barriers to Lateral Diffusion in Supported Lipid Bilayer Membranes by Blotting and Stamping. *Langmuir* 2000; 16:894-897.
- [5] Electric Field-Induced Concentration Gradients in Planar Supported Bilayers”, Jay T. Groves and Steven G. Boxer, *Biophysical Journal*, 69, 1972-1975 (1995).
- [6] “Patterning Hybrid Surfaces of Proteins and Supported Lipid Bilayers”, LA Kung, L Kam, JS Hovis and SG Boxer, *Langmuir*, 16, 6773-76 (2000).

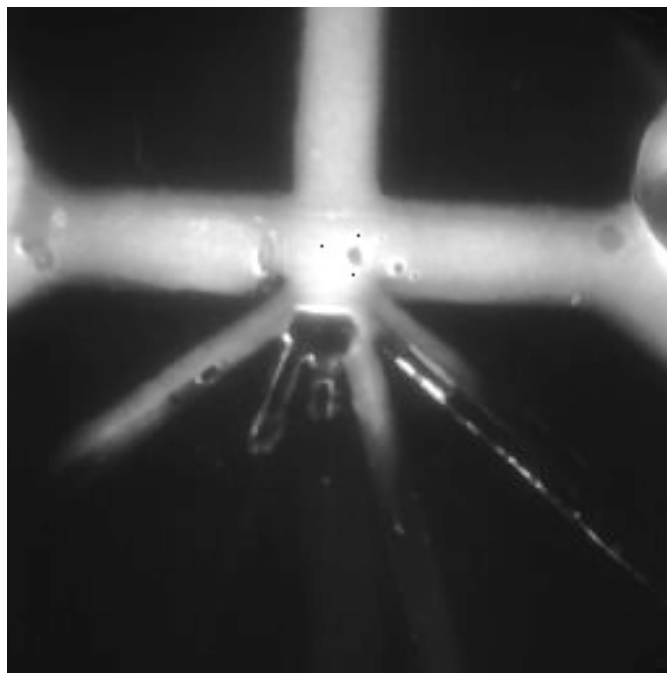


Figure 3: Flow control experiment.

Optimizing DNA “Inks” for Microarrays

Samar Hubbi, Engineering Science, New Jersey Institute of Technology,
sxh0211@njit.edu

Principal Investigator(s): Mary Tang, Electrical Engineering,
Stanford University, mtang@snf.stanford.edu

Abstract:

Long strands of DNA were complexed with cationic compounds in order to decrease solution viscosity and maintain constant surface tension. The cationic compounds (with three or more positive charges) interact electrostatically with negatively charged DNA molecules reducing the solution viscosity. My goal was to study the effect of spermine (with four positive charges) and polylysine (with approximately 200 positive charges) on the surface tension and viscosity of concentrated DNA solutions in various salt solutions.

Introduction:

In DNA microarrays (“gene chips”), tens of thousands of DNA sequences are arrayed on a single chip. Complementary binding of these sequences with cDNA from a biological sample is related to specific genes that are active in the sample. Thus, gene chip technology enables massively parallel acquisition of gene expression data, allowing study of gene function. DNA microarrays are fabricated by several methods. Inkjetting is a much more precise, reproducible method, though is restricted to reagents for DNA synthesis or very short DNA fragments (</=25 bases). Because cDNA molecules are much longer (typically 1-2 kilobases), their solutions are much more

viscous and their behavior is less predictable, making them inappropriate for inkjetting. Inkjetting long strand DNA would provide cheaper, faster and accurate microarrays. While the research focuses on DNA inks, the principle of packaging charged polymers with oppositely charged compounds has enormous implications in different technologies, including inkjetting electroluminescent polymers for light emitting devices and displays as well as therapeutic agents for cystic fibrosis patients.

Experimental Procedure:

In order to understand how a drop of liquid will interact with a solid surface, it is important to understand the surface tension behavior of the liquid. Using the FTA200, we measured the surface tension of different solutions. A drop is dispensed and held on the tip of a syringe needle. The drop shape analysis assumes that the drop is symmetrical along a vertical axis and not in motion; thus only gravity and surface tension influence drop shape. The Young-Laplace equation defines the relationship between interfacial pressure, drop shape and surface tension of the drop.

$$\Delta P = \gamma (1/R_1 + R_2)$$

where ΔP = interfacial pressure difference, γ = interfacial tension, $R_1 + R_2$ = radii of curvature of the drop. Tate’s Law is used to determine the maximum volume or weight of the pendant drop that can be supported on the syringe tip.

$$W = 2 \pi r \gamma$$

where W = weight of drop, R = radius of tip, γ = surface tension.

Viscosity measurements were made using the Ostwald viscometer, in which the flow of a small volume of solution through a narrow capillary tube is timed. In our experiment, we pipetted 10 mL of our solution into the right hand column of the viscometer. Suction was applied to the capillary side (the left hand side) of the viscometer to draw the liquid slightly above the bubble. When the suction was released the liquid was allowed to flow freely down the capillary tube. Time is taken as soon as the liquid passes a designated marker on top of the bubble and ends when the meniscus passes the lower marker.

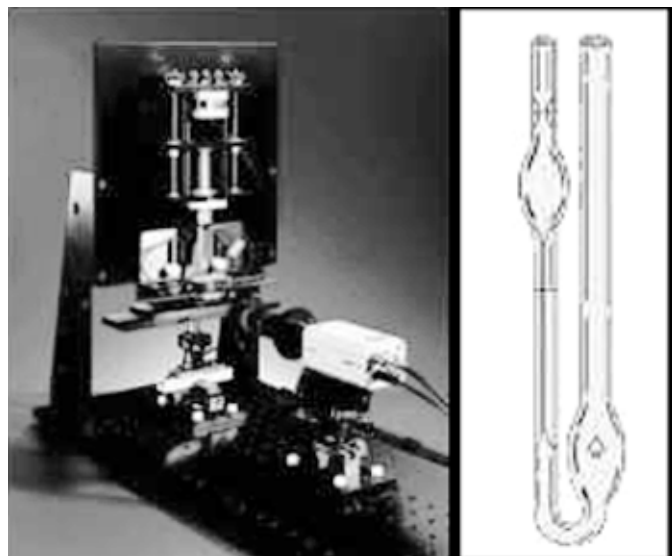


Figure 1, Left: FTA200 Surface Tension Measurement.
Figure 2, Right: Ostwald Viscometer

Results and Discussion:

Chart 1 compares the surface tension of different solutions. This was done to compare the accuracy and reproducibility of our measurements with known measurements. Water has a surface tension of 72.8 dynes/cm. The mean of our measurements was 70.515 dyne/cm with a standard deviation of 0.57. We tested TE Buffer because our DNA solutions were in TE Buffer to preserve solution environment. TE Buffer with 150 mM NaCl was used to compare the effect of salt or other impurities on surface tension and to mimic the salt environment found in lung sputum of cystic fibrosis patients. The data suggests with added impurities, the surface tension decreases, since surface tension can be regarded as the measure of the cohesiveness between the solutions molecules. When impurities are added, such as salt, the attraction between the molecules is disrupted, resulting in lower surface tension.

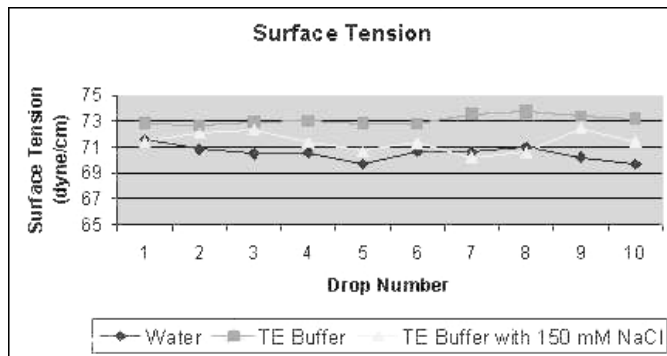


Chart 1

Table 1 shows the surface tension of solutions with different concentrations of DNA. The average values are surprisingly similar, considering the viscosities increase dramatically in this range. The standard deviations, however, increase with DNA concentration, showing that surface tension becomes more uncontrolled.

DNA Concentration (mg/ml)	Surface Tension (dynes/cm)
0.25	73.55 (.36)
0.5	71.37 (.55)
1	72.06 (.68)
5	70.98 (.81)
10	63.62 (3.67)

Table 1

In Chart 2, we added cationic compounds and ran viscosity tests to observe viscosity changes. The mean relative time of DNA in the Ostwald viscometer was 1.04 sec. After complexing the DNA with spermine, the mean time decreased to 0.95 sec. However with polylysine, it stayed relatively the same at 1.05 sec. It is apparent from the graph that DNA with spermine had a relatively decreased and stable viscosity regardless of the increasing concentrations, as compared with uncomplexed DNA which varied according to DNA concentration.

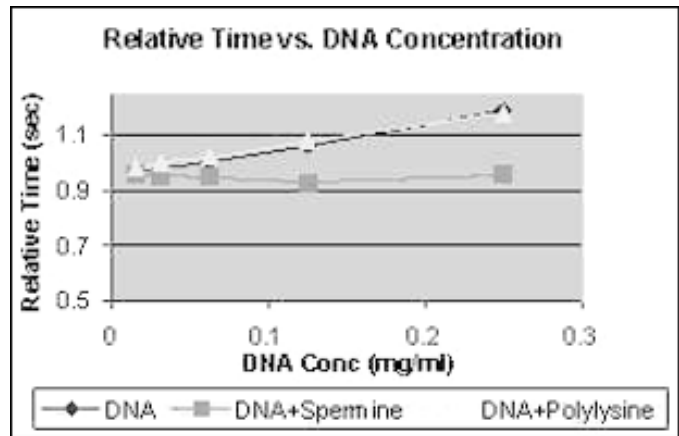


Chart 2

Conclusions:

The static surface tension measurements of solutions with varying concentrations of DNA were very similar. Complexed DNA solutions were not studied. The viscosity measurements of solutions of DNA with spermine decrease dramatically compared with solutions of DNA alone. Polylysine did not have this same effect. One of the reasons polylysine may not have been successful is due to the large number of positive charges. Polylysine has more than 200+ charges, and thus is also a strong polyelectrolyte, like DNA. So any excess polylysine that is not complexed with DNA will have the same effect of increasing solution viscosity.

References:

- [1] Lipschutz, R.J.; Fodor, Stephen; Gingeras, T. R.; and Lockhart D.J. 1999. High Density Synthetic Oligonucleotide Arrays. *Nature Genetics* 21: 20-24.
- [2] Mir, Kalim U.; and Southern, Edwim M. 2000. Sequence Variation in Genes and Genomic DNA: Methods for Large-Scale Analysis. *Annu. Rev. Genomics Hum. Genet.* 1: 329-360.
- [3] Ramsay, Graham. 1998. DNA chips: State-of-the-art. *Nature biotechnology* 16: 40-44.
- [4] Schena, Mark. 1999. *DNA Microarrays: A Practical Approach*. New York: Oxford Univ. Press.

Flow-Through Processing on a Microchip for DNA Pyrosequencing®

Noel Jensen, Physics, Colorado College, nd_jensen@coloradocollege.edu

Principal Investigator(s): Peter Griffin, Dept. of Electrical Engineering, Stanford University, griffin@plumb.stanford.edu

Abstract:

Microchips designed for DNA sequencing on a micron scale offer the possibility of fast, cheap processing far beyond the capabilities of current techniques. One problem with processing on a microchip is the manipulation and localization of the various reagents necessary to the sequencing reaction. Chip prototypes have been fabricated that deal with this issue using a combination of microfluidic sieves, wells, and channels.

Introduction:

Pyrosequencing® is a DNA sequencing technique where a special chemistry is used such that the incorporation of each nucleotide into a single strand of DNA results in the emission of light. Since nucleotides are incorporated linearly along the length of the strand, the sequence may be determined by adding each of the four bases (A, C, T, or G) one at a time. The light emitted by the incorporation of a nucleotide will then correspond to the last base added. Hence sequencing is performed by light detection [1].

In order for pyrosequencing® to be reliable, it is necessary to have some means for the disposal of excess nucleotides. This may be partially accomplished by using an enzyme to continually degrade those nucleotides that are not incorporated into the DNA. However, nucleotide buildup is still observed after twenty to thirty bases have been sequenced. Our approach uses flow-through processing to remove any remaining waste products of the sequencing reaction. This additional step should significantly increase the possible resolution and read-length for pyrosequencing® methods. Microchips were fabricated using current optical photolithography techniques. Consequently, this technology will be compatible with the multitude of other technologies that make use of the same fabrication processes.

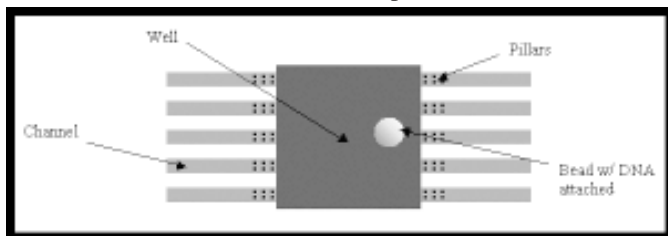


Figure 1: Top view of a single well.

Because the nucleotides and reagents used in the sequencing process are charged species, flow through the channels may be accomplished using electroosmosis [2]. A voltage bias is applied to the channels across a well that serves as a reaction chamber for the sequencing reactions. DNA attached to silicon beads is kept within the well by means of pillars etched in silicon at the well-channel interface. The spacing between the pillars is chosen to be smaller than the diameter of the beads (Figure 1). Thus nucleotides and excess reagents are free to flow out through the channels while the DNA is localized to the well.

Procedure:

Two photolithographic masks were designed for the fabrication of these chips. First, a pattern of channels was etched onto one side of a double-polished silicon wafer. Then a pattern of wells was aligned to the channels and etched completely through the wafer from the opposite side. Finally, the channel-side of the etched silicon wafer was bonded to a glass wafer (Figure 2).

Results and Discussion:

Channels and pillars were etched to a depth of approximately 50 μm . Using the STS Multiplex ICP

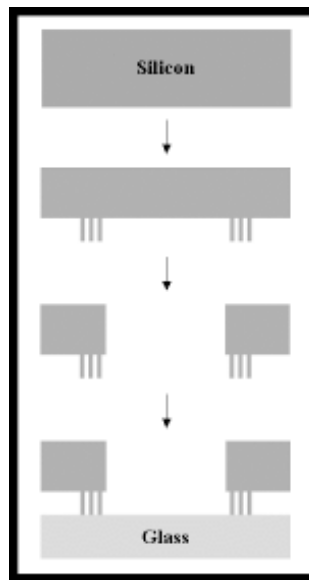


Figure 2: Fabrication Process.

Deep Reactive Ion Etcher, we were able to obtain near vertical etch profiles for the channel walls and pillars (shown in Figure 3). Several different well sizes ranging in dimension from 50 μm to 2 mm were fabricated in order to determine the optimal dimensions for future microchips.

A few elements of the chip design warrant discussion. We chose to use multiple channels to interface with a single well because electroosmotic flow is known to occur along the surface of a channel [3]. By

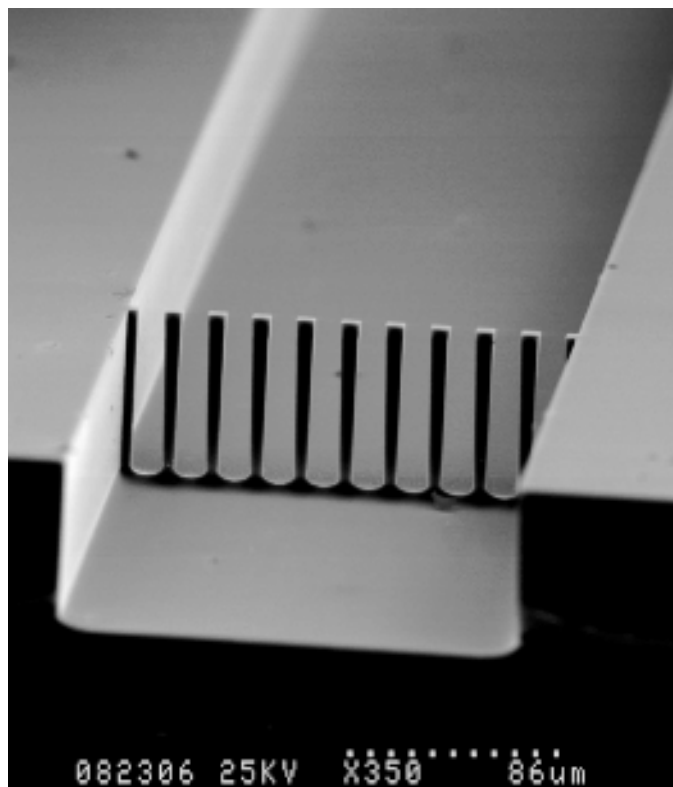


Figure 3: SEM micrograph of pillars etched in a channel.

using multiple channels we were able to increase the surface area available for flow. Glass was the substrate chosen to cap the channels for two reasons. First, it bonds well with silicon. Second, it is transparent and allows DNA, nucleotides, and the various other enzymes necessary to pyrosequencing® to be added from above while the reaction is imaged from below (Figure 4). Multiple sets of pillars were included in the design because of the uncertainties associated with the alignment of the wells with the channels. They were also included to compensate for the fact that STS etch profiles are not entirely vertical.

Summary:

Several microchips have been fabricated. Testing needs to be done to determine the effectiveness of using electroosmotic flow to remove excess nucleotides from the reaction area. Also, an optimal well size must be established. Once this has been done, investigations should be made into the possibility of parallel processing in multiple wells onto a single chip.

Acknowledgements:

Thanks to Peter Griffin for his guidance. My partners in crime were Jon Schuller and Ravi Sarin. Also, thanks to Reza Kasnavi and Mostafa Ronaghi for their advice and support. This wouldn't have gone smoothly without Mike Deal, Jane Edwards, Melanie-Claire Mallison, and the SNF Staff. Thanks to NSF and NNUN for the opportunity.

References:

- [1] "Real-Time DNA Sequencing Using Detection of Pyrophosphate Release", M. Ronaghi, S.Karamohamed, B. Pettersson, M. Uhlen, and P. Nyren, *Analytical Biochemistry*, vol. 242, pp. 84-89, 1996.
- [2] "Electroosmotic Pumping and Electrophoretic Separations for Miniaturized Chemical Analysis Systems", A. Manz, C. S. Effenhauser, N. Buggraf, D. J. Harrison, K. Seiler, and K. Fluri, *J. Micromech. Microeng.*, vol. 4, pp. 257-265, 1994.
- [3] "Numerical Simulation of Electroosmotic Flow", N. A. Partankar, and H. H. Hu, *Anal. Chem.*, vol. 70, pp. 1870-1881, 1998.
- [4] "Integrated System for Rapid PCR-Based DNA Analysis in Microfluidic Devices", J. Khandurina, T. E. McKnight, S. C. Jacobson, L. C. Waters, Robert S. Foote, and J. M. Ramsey, *Anal.Chem.*, vol. 72, pp. 2995-3000, 2000.
- [5] "An Integrated Nanoliter DNA Analysis Device", M. A. Burns, B. N. Johnson, S. N. Brahmasandra, K. Handique, J. R. Webster, M. Krishnan, T. S. Sammarco, P. M. Man, D. Jones, D. Heldsinger, C. H. Mastrangelo, and D. T. Burke, *Science*, vol. 282, pp. 484-487, 1998.

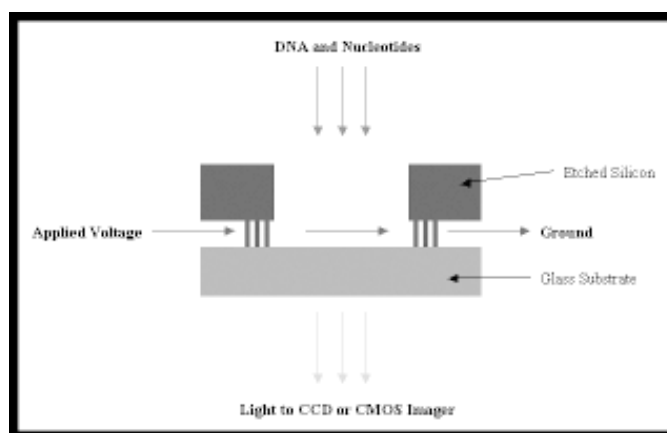


Figure 4: Sequencing Flow Diagram.

Analysis of Electron Emission from Diamond using an E-Beam Micro-Column

Kate Klein, Mechanical Engineering, Trinity College, Kate.Klein@mail.trincoll.edu

Principal Investigator(s): Prof. Fabian Pease, Electrical Engineering Dept, Stanford University, pease@cis.stanford.edu

Mentor(s): Dan Pickard, Electrical Engineering Department, Stanford University

Abstract:

Due to its unique properties, diamond has many potential applications in the electronics industry. The applications range from high temperature transistors to low dark current photo-emitters. In this study, the properties of large bandgap materials such as diamond, cubic boron nitride, and aluminum nitride will be investigated. The electron loss mechanisms within the thin films of these materials can be measured in order to gain insight into the physical properties of semiconductors. The experimental apparatus for these measurements is a modified scanning auger electron microscope, with the major modification being the addition of a second, miniature electron column. This micro-column will focus an electron beam onto the back surface of the sample, transmitting electrons, which can then be measured with a hemispherical energy analyzer. From the energy loss spectra, conclusions can be drawn about the physical mechanisms and properties of diamond and other large bandgap materials.

Introduction: an Experimental Theory:

Increasingly there has been a need for wide bandgap materials reliable at temperatures greater than 125°C, for such high temperature applications as automotive and aerospace engine control units. The currently used semiconductors are Si and GaAs, however new materials including Silicon Carbide, III-nitrides, n-alloys, and

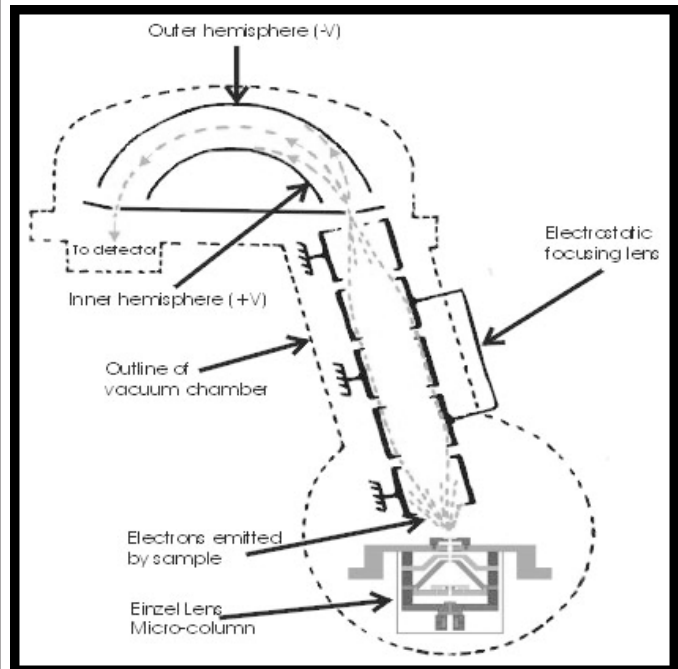


Figure 2: Hemispherical Energy Analyzer

diamond are being researched. Diamond is an ideal candidate because of its negative electron affinity (NEA), high thermal conductivity, low resistivity, radiation hardness, and chemical inertness. In addition, diamond has a high breakdown field ideal for high speed, high power devices.

In order to evaluate the electron emission from thin-film diamond and other semiconductors, an apparatus was required. Therefore, a scanning auger electron microscope was modified for the purpose of this experiment. The old sample stage had to be replaced by a new stage containing a small micro-column. Instead of the incident beam coming from a large gun above, a smaller beam would be emitted from the micro-column beneath the sample. Theoretically, if the film were thinned to an optimal thickness, a portion of the incident beam would be transmitted through the sample; in addition, some secondary electrons would also be emitted (see figure 1). These secondary electrons would have relatively low energy and could be easily collected by a detector above the sample. This detector, which normally receives auger electrons, could instead collect the

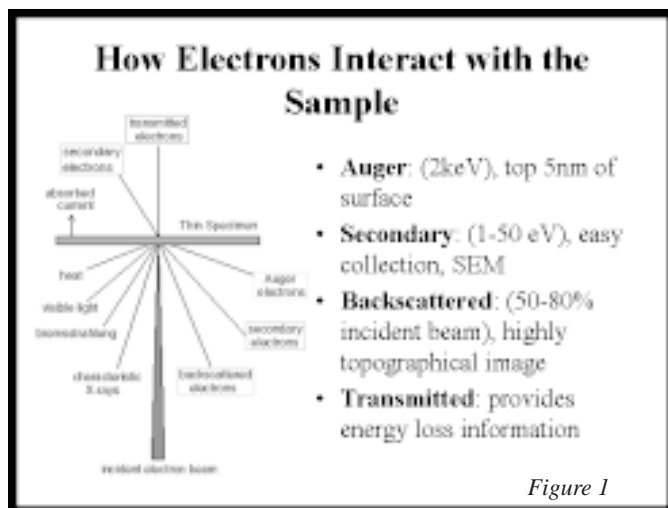


Figure 1

transmitted secondary electrons and send them to the hemispherical energy analyzer to be measured (see figure 2).

The hemispherical energy analyzer works by applying a negative potential to the curved outer plate and a positive potential to the curved inner plate. As the collected electrons enter the hemispherical chamber and travel around the arc, the higher energy electrons strike the outer plate and the lower energy electrons strike the inner plate. However, electrons with energy equal to the “pass-energy” of the analyzer will exit the slit at the end of the arc, where the signal is then amplified. By sweeping the voltages applied to the inner and outer plates an energy spread spectra will result.

Procedure:

After the old system was brought up to air, measurements of the stage were taken and numerous seals, filaments, and pump parts were replaced. Then the system was cleaned and reassembled. After baking at 150°C for three days, ultra high vacuum of 10^{-11} torr was achieved. It was now possible to achieve beam and run the microscope in SEM imaging mode. Since the old Digital Computer System was outdated and not functioning, the next step was to upgrade the analyzer controls, with the installation of a new computer, hardware and software.

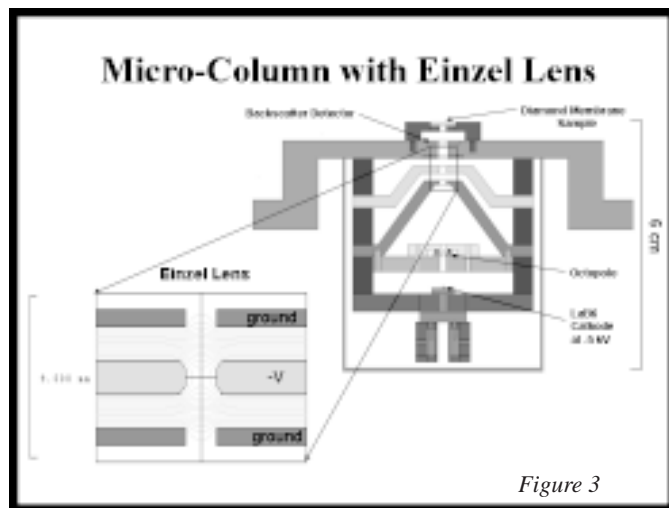


Figure 3

The next major obstacle was designing the micro-column stage and sample mount (see figure 3). The new stage could not be more than 6 cm tall; therefore, there were material and size constraints to consider. The micro-column was to contain a LaB₆ cathode (for beam source), octopole (for rastering beam), einzel lens (for focusing beam), backscatter detector (for aligning beam) and a removable sample mount. The einzel lens, a uni-potential electrostatic lens, focuses and de-magnifies the electron beam onto the back of the diamond sample. Depending on the distance between the electrodes, the distance from the center of the lens to the sample, the size and shape of the electrodes, and the voltages applied to

the electrodes, varying spot sizes, astigmatisms, distortions, and aberrations can occur. In order to minimize these effects, the Munro particle optics simulation program was used to model the column and optimize the parameters.

After the micro-column design is finalized, the parts can then be machined, assembled and the new stage installed. The final step will be to prepare thin film diamond samples and obtain energy spread measurements for EBS (electron bombardment source) using the new system.

Future Work:

There still remains a lot of work to do on this project. The micro-column stage is awaiting manufacture, and the new analyzer control software needs to be optimized for the system. Once that is done, energy loss data for diamond and other semiconductor samples can be collected. The result of the energy spread measurement will provide information about the internal mechanisms, physical properties, effects of doping, and relationship of sample thickness vs. emission. Hopefully, after the completion of this experiment, there can be conclusions drawn about the emission properties of diamond as compared to other wide bandgap materials.

Acknowledgements:

Thanks to SRC and Darpa, the NSF REU Program, Stanford University Center for Integrated Systems facility, P.I. Fabian Pease and Mentor Dan Pickard for all your help and support.

Minimum Line-Width Features for Cryogenic Optical Photon Detectors

Natalie Lui, Physics, Harvard University, lui@fas.harvard.edu

*Principal Investigator(s): Blas Cabrera, Physics,
Stanford University, cabrera@stanford.edu*

Mentor(s): Paul Brink, Physics, Stanford University, pbrink@hep.stanford.edu

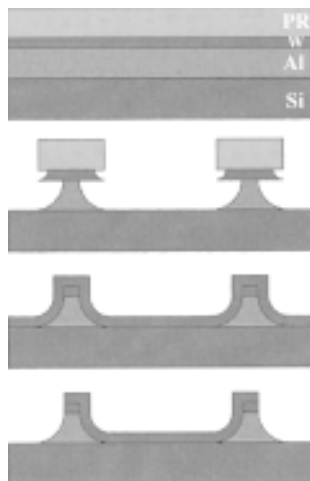
Abstract:

New optical-photon detectors using transition-edge sensors have been developed by the Cabrera group at Stanford University. Low temperature superconducting tungsten and aluminum films, deposited on silicon substrates, are patterned into an array of individual sensors using standard semiconductor manufacturing equipment. The primary application is to determine the energy and time of arrival of each optical photon from sources in space, such as the Crab pulsar.

The instrumentation of a multi-pixel imaging detector array requires ultra-thin read-out lines to maximize detection area and minimize rail events. By using the Hitachi E-Beam Lithography machine, optical photon detectors with more pixels and thinner read-out lines can be produced. Improved optical photon detectors will have higher count rates and better point spread functions, and can be used in many new experiments in cosmology and astronomy.

Introduction:

From the eye to the Photo-Multiplier Tube (PMT) to the CCD camera, many different types of photon detectors are used every day throughout the world. The Cabrera group at Stanford University has recently developed photon detectors using transition-edge sensors (TES). For each individual optical photon detected, it can resolve the energy to within 10% and determine the arrival time to within a microsecond. Such a detector is of interest in astronomy and other 'photon starved' applications. The pixels and wires of a TES are made using optical photolithography with standard semiconductor manufacturing equipment. As shown in Figure 1, the process involves two separate exposures to form a tungsten pixel attached to silicon.



The wires are connected to an electronic circuit containing

Figure 1: Photolithography process for producing a TES detector.

a Superconducting QUantum Interference Device (SQUID), which measures the change in current when the photons hit the pixel. The detector can thus determine the time of arrival, energy, and phase of each incoming photon. Pixel arrays are placed inside telescopes to observe light sources in space. At the McDonald Observatory in Texas, the Cabrera group collaborated with the Romani astrophysics group from Stanford University to study the Crab Pulsar. They plan to study the faint Geminga Pulsar in the future.

Mask Design:

With standard optical photolithography, the Cabrera group designed arrays of 23 μm square pixels and 1 μm wires with 1 μm spacing. Unfortunately, information is lost whenever a photon hits the wires instead of the pixels, so smaller wires increase the count rate and improve the point spread function. My project for the summer was to explore the use of e-beam lithography to fabricate the wiring for the pixel array. I designed an 8 by 8 array of 20 μm square pixels with 200 nm wires spaced 200 nm apart. Because 200 nm wires are vulnerable to damage on the wafer, they connect to larger 1.4 μm wires immediately outside the pixel array.

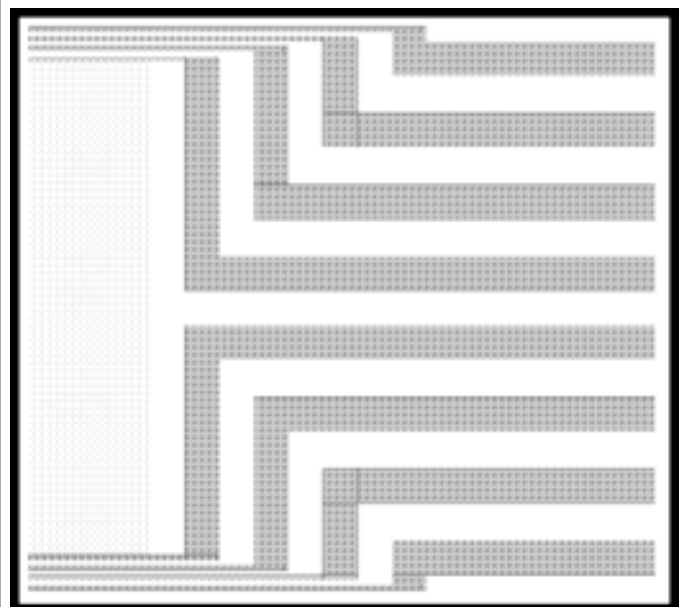


Figure 2: Close-up of wiring for a pixel at the end of a row.

Eventually, the wires will need to increase in size to connect to 50-100 μm bonding pads, to hook them up to an electronic circuit. Figure 2 shows a close-up of the wiring for one pixel.

Lithography:

Our first step was to pattern the wiring layer onto a wafer coated with 200 nm of aluminum and 500 nm of UV5-0.6 photoresist. We looked at the results after exposing the wafer using the Hitachi HL-700F Electron Beam Lithography Machine and developing the photoresist. The pixel array, as well as a piece of dust that must have contaminated the chip during dicing, is shown in Figure 3a, a scanning electron microscope (SEM) picture of the chip. Figure 3b shows straight and evenly spaced 200 nm wires, a promising result. Unfortunately, there were also wires that turned out broader with less spacing in between, as in Figure 4a. They probably occur because the e-beam machine uses the same exposure dosage for large and small features. This example of the 'proximity effect' problem is often associated with e-beam electron scattering in the vicinity of the design features. To correct the problem, we added some 200 nm wires parallel to these isolated ones just for show, imitating the rows of wires among the pixels. As shown in Figure 4b, the wires turned out well after changing the mask design.

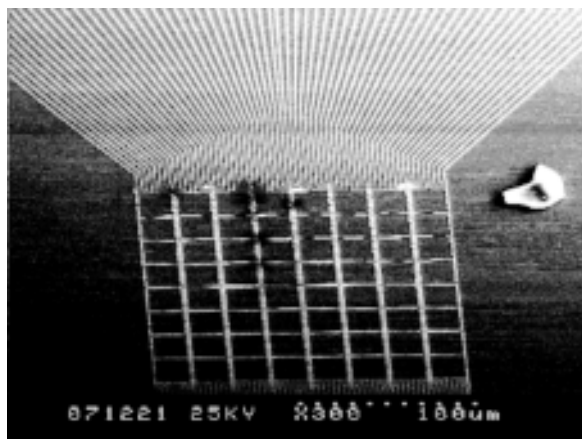


Figure 3a: SEM photo of lithography on aluminum and photoresist.

Etching:

Once we knew the lithography results were reproducible, we investigated etching wafers with 200 nm of aluminum and 100 nm of tungsten. We tried dry plasma etching in order to avoid the undercutting and overhangs portrayed in Figure 1. The tungsten layer was etched with the Drytek Plasma Etcher, and the aluminum layer was etched with the Applied Materials Precision 5000 Etcher. Unfortunately, none of the wafers looked good, despite trying many different processes and varying the etch rates.

Conclusions:

Although exposing the pattern using the e-beam machine went smoothly, etching through an aluminum-tungsten bilayer proved more difficult than expected. In the future, we could try liftoff, a process where the metal layer is placed on top of the developed photoresist pattern.

Acknowledgments:

Many thanks to my mentor Paul Brink, who woke up at 4 a.m. to use the e-beam machine with me. Also thanks to Pat Castle, for his help on the SEM and in the lab. And of course thanks to Michele Cash, Jen Burney, and Lindsay Moore, for making my summer lots of fun.

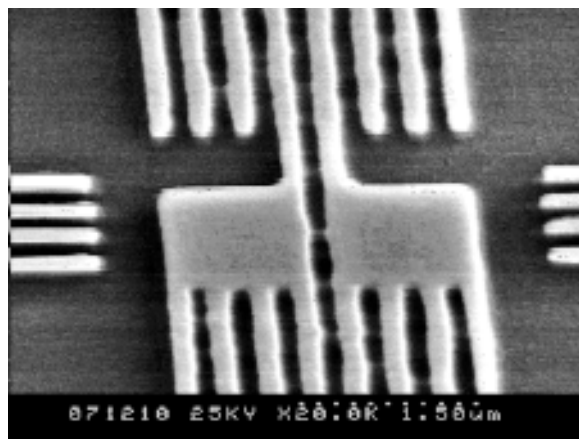


Figure 3b: Close-up of 3a.

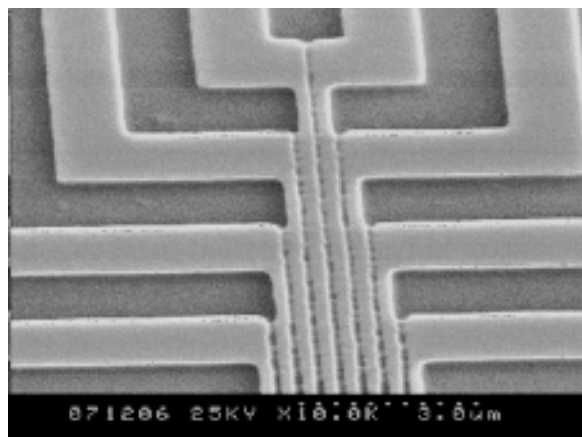


Figure 4a: Smudged wires.

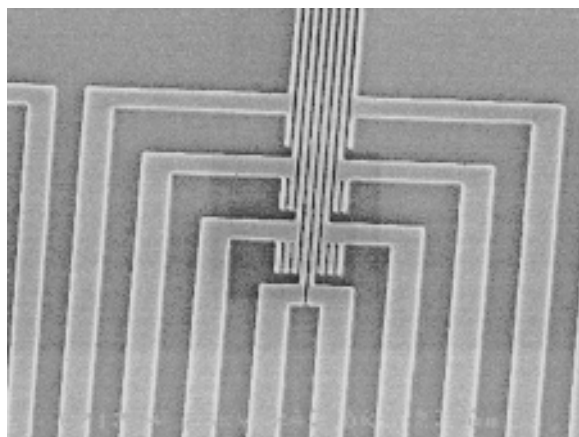


Figure 4b: Clean wires with new design.

The Integration of Carbon Nanotubes into Electronic Devices

Nathan Morris, Chemistry, University of California, Berkeley, nsm1161@yahoo.com

Principal Investigator(s): Hongjie Dai, Chemistry, Stanford University, hdai1@stanford.edu

Mentor(s): Nathan Franklin, Chemistry, Stanford University, nfrankli@stanford.edu

Abstract:

There has been much excitement in the potential use of carbon nanotubes in integrated circuits. With an average radius of 2-3 nm and unique electrical properties, single wall carbon nanotubes (SWNTs) represent one of the most promising materials for construction of molecular electronics. Controlled growth of SWNTs into arrays, highly oriented interlaced patterns, is however, a challenge to their future use in integrated circuitry. We have achieved production of aligned SWNTs using chemical vapor deposition (CVD) coupled with the application of an electric field. Using the induced dipole-dipole interactions produced by the application of an electric field, we will now attempt to grow aligned carbon nanotubes into interlaced arrays on silicon substrates. Such arrays will mark the first step in the production of circuitry using carbon nanotubes.

Introduction:

A single-walled carbon nanotube is a single sheet of graphite rolled into itself. SWNTs are ideal for use in the electronics industry because of their small size (average radius of 1-3 nm), and their ability to act as conductors or semi-conductors depending on chirality. Our goal is to make an ordered array or criss-crossing grid of SWNTs (figure 1). Controlled growth of carbon nanotubes is the

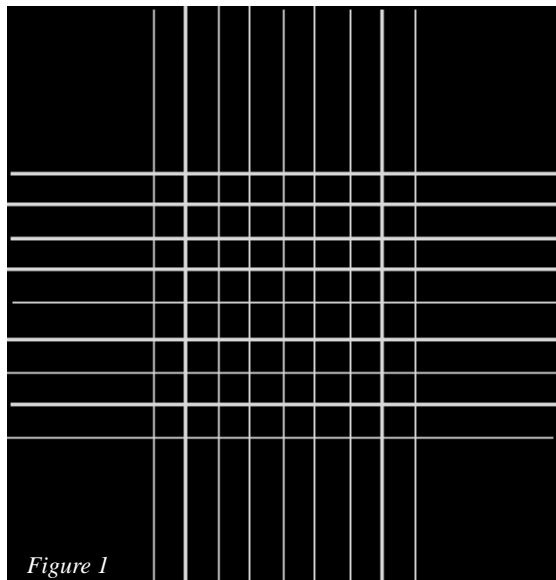
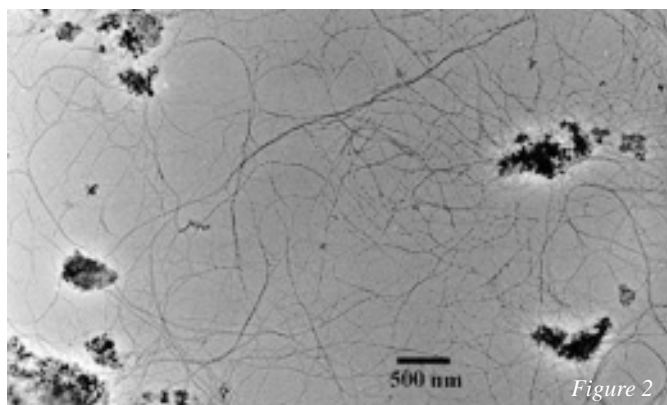


Figure 1

first step in the integration of SWNTs into functional memory arrays and other electronic components for the future [1]. The primary obstruction to fabrication of ordered arrays of SWNTs is the inability to control growth. Figure 2 shows normal random growth.



Carbon nanotube manipulation and control has been achieved on a small scale using AFM. However, this method is impractical when dealing with the large number of carbon nanotubes that would be required to build functional memory arrays. We have previously developed a method of growth and alignment that functions in tandem to produce regularly aligned nanotubes. SWNTs are grown using chemical vapor deposition (CVD) and alignment is achieved by inducing a dipole on the carbon nanotubes. A dipole is induced on the nanotube by applying a voltage at opposite ends of the silicon trench (figure 3).

As the tube grows out from the side of the trench during CVD, it is aligned due to the dipole-dipole interactions that occur between the silicon surface and the SWNTs.

$$p = q \times d$$

where q is the charge on the nanotube, d is the length of the nanotube, and p is the dipole induced on the nanotube. We have attempted to use this previously developed method of controlled growth and alignment in the fabrication of ordered arrays of SWNTs.

Procedure:

Standard 4 cm quartz wafers were used in fabrication.

A 2 μm layer of polysilicon was deposited on the quartz surface followed by deposition of 100 μm layer of oxide on the silicon surface. Using photolithography and chemical etching, a square of silicon oxide 100 μm long and 50 μm deep was etched. Using the same technique, four 20 μm wide channels at each corner of the square were also etched. The channels extend to the outside edge of each chip. The channels ensure that there is no current flow from one side of the chip to the other. Two μm 's of PMMA (polymethylmethacrylate) were deposited on the chip. E-beam was used to remove 2 μm wide squares on each edge of the large main square that was etched out of the chip. The 1 μm wide squares were spaced two μm s apart to achieve better control over growth. A solution of Fe/Mo/ Al_2O_3 which is a catalyst for SWNT growth was pipetted onto the surface of the chip, and the wafers were baked at 170°C for 5 minutes. The PMMA was removed with DCE (dichloroethane) and thoroughly dried.

Two Tungsten electrodes were then attached to each side of the chip. Tungsten electrodes were selected because they do not oxidize at the high temperatures (900°C) required for CVD growth of SWNTs. Two lines were connected to the electrodes and the wafer was attached to a ceramic holder. The sample was placed in the CVD furnace and heated to 900°C in the presence of H_2 to prevent oxidization of the metal wires and tungsten electrodes. Voltages between 50 to 100 volts DC were applied to the electrodes. A mixture of CH_4 and H_2 , gases used for nanotube growth, was pumped into the chamber. Varying flow rates were attempted, but the highest yields were obtained using a rate of 0.5 standard liters per minute (SLM) of CH_4 and 200 standard cubic centimeters per minute (SCCM) H_2 . The gas was flown for four minutes before the temperature was turned down. Gas was continuously flown in until the temperature in the chamber fell below 200°C.

Results and Conclusions:

Experimental results were problematic, but showed promise for future improvement. The use of e-beam on quartz wafers proved especially difficult due to the charge build up on the quartz surface. This created problems in chip fabrication that can possibly be corrected with the use of alternate materials. Nanotube yield in the final results was lower than expected. Continued experimentation is required on the method of catalyst deposition, in order to improve the yield of SWNTs. Future work is also required to determine ideal voltages applied to induce the dipole. These results are preliminary and show potential for further research.

References:

- [1] T. Rueckes, K. Kim, E. Joselevich, G. Y. Tseng, C.-L. Cheung, C. M. Lieber, "Carbon Nanotube-Based Nonvolatile Random Access Memory for Molecular Computing" (2000) *Science* 289, 5476, 94-97.

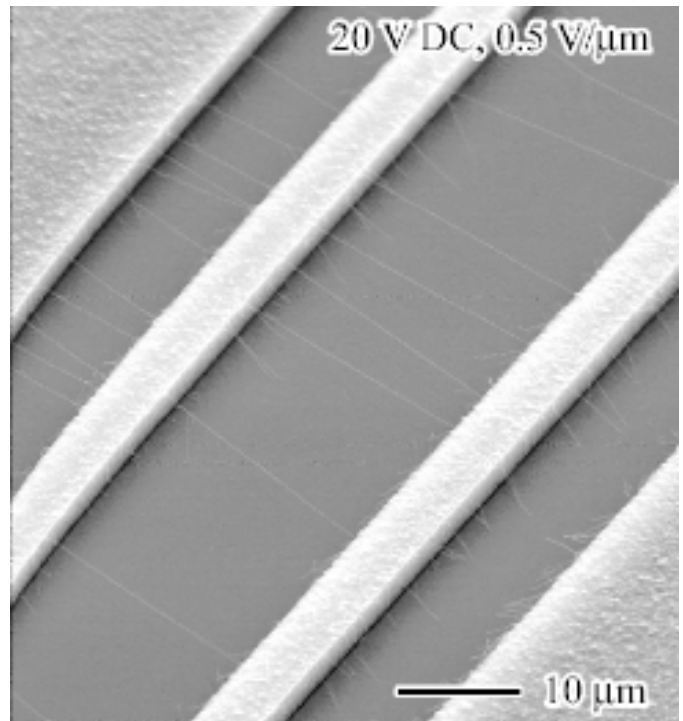


Figure 3: Aligned growth.

Characterizing the Viscosity of Concentrated Solutions of DNA with Cationic Agents

Linda H. Ohsie, Biochemistry and Molecular Biology, Dartmouth College,
Linda.Ohsie@Dartmouth.edu

Principal Investigator(s): Mary Tang, Electrical Engineering,
Stanford University, mtang@snf.stanford.edu

Abstract:

Concentrated solutions of free DNA are extremely viscous and can have unpredictable surface tension. Although not much is currently known about the fluid properties of concentrated DNA solutions, they have many important implications. For example, in the fabrication of DNA microarrays, inkjetting cDNA is unreliable because the unusual fluid behavior greatly limits the capacity of the inkjets to dispense concentrated DNA solutions. In the clinical field, the high viscosity of DNA-containing fluid in the lungs is responsible for many pulmonary dysfunction complications in patients with cystic fibrosis.

Multivalent cationic compounds ($\geq +3$ charges) are known to complex electrostatically with negatively charged DNA. In our experiments, we observed that the viscosity of concentrated DNA solutions decreased dramatically upon complexation. The surface tension in dilute DNA solutions was also characterized.

Introduction:

The human genome contains approximately three billion base pairs and when stretched out, it extends to an astounding length of two meters per cell. However, the diameter of a typical eukaryotic cell nucleus is only 5-10 μm . It is clear then, that DNA must be stored in a rather compact form. In the cell nucleus, the negatively

charged DNA is complexed in an orderly, hierarchical fashion around positively charged histone proteins to form nucleosomes [1]. Outside the cell, in the absence of the complex mechanisms necessary to maintain the integrity of the nucleosomes, DNA is found free of histones. At high concentrations, free DNA solutions are extremely viscous and surface tension is unpredictable. Applications as diverse as inkjetting technologies and lung dysfunction in cystic fibrosis are strongly dependent upon the fluid behavior of concentrated DNA solutions.

The goal of our experiments was to study the surface tension and viscosity of concentrated solutions of free DNA and DNA in complexes with cationic agents. Surface tension is defined as the energy required to increase the surface area of a liquid by a unit amount (dy/cm). And viscosity is the resistance of liquid to flow (kg/m sec or poise). Based on the behavior of DNA observed in the cell nucleus in the presence of cationic histones, we hoped to see the free DNA in solution form complexes with cationic agents introduced into the solutions. We proposed that the solution viscosity would significantly be reduced and predictability of surface tension would be improved.

Procedure:

The DNA used in our experiments was salmon sperm DNA. The DNA was suspended in 10 mM Tris/1mM

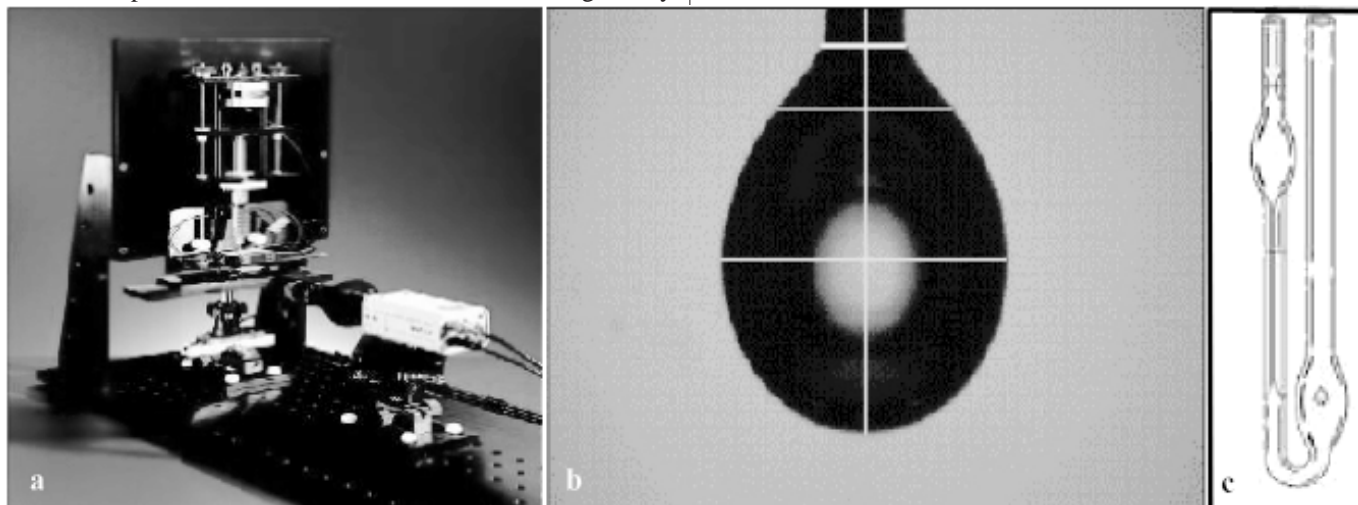


Figure 1: a) FTÅ200 Dynamic contact Angle/Surface Tension Analyzer. Surface tension was measured using the pendant drop method. b) Image analysis performed on a drop [4]. c) Ostwald Viscometer. Measures the relative viscosity of liquids [5].

EDTA to prepare a stock solution with a concentration of 20 mg/mL. From this stock solution, we prepared solutions with various concentrations of DNA, with and without 150 mM NaCl (to approximate the physiological environment), and with and without cationic agents (spermine and polylysine).

Surface tension measurements were made on DNA solutions (without cationic agent) using the FTÅ200 Dynamic contact Angle/Surface Tension Analyzer (Figure 1a). To measure solution viscosity, we performed a dilution series using an Ostwald Viscometer (Figure 1c).

Results and Conclusions:

Table 1 shows the surface tension of various DNA solutions. Although the average values are reasonably similar, the surface tension becomes less predictable with increasing DNA concentration, as shown by the increasing standard deviation.

DNA Concentration, in mg/ml	Surface Tension, in dy/cm (std dev)
0.25	73.55 (.36)
0.5	71.37 (.55)
1	72.06 (.68)
5	70.98 (.81)
10	63.62 (3.67)

Table 1: Surface tension for TE solutions containing varying concentrations of DNA.

Figure 2 shows the relative viscosities of DNA solutions with and without cationic agents. Spermine (+4) was more effective in reducing viscosity of this DNA solution than polylysine (> +200), although polylysine should complex with the DNA more effectively due to its greater charge. Since polylysine, like DNA, is a long, highly charged polymer, in free form, it will increase viscosity when in solution. Thus, it is suspected that excess, uncomplexed polylysine may actually affect the viscosity. Further experiments would be needed to optimize the relative concentrations of polylysine and DNA to obtain lowest viscosity.

We hope that the results of our research can lead to improvements in inkjetting technology in the fabrication of DNA microarray assays. Developing the capability to reduce the viscosity of concentrated solutions of DNA would allow cDNA to be inkjetted, improving throughput and robustness of inkjetting technology [2]. Improving predictability of surface tension of concentrated solutions of DNA would allow the production of better quality, highly dense arrays. Studying the fluid behavior of concentrated solutions of DNA can also aid in the development of a therapeutic treatment for cystic fibrosis patients. In cystic fibrosis patients, the characteristic and unusually thick mucus in the lungs is largely composed of free DNA. Normal sputum has a DNA concentration of 2-4 µg/mL. Sputum DNA content in CF patients can range from 2.4-19.4 mg/mL [3]. Significantly reducing the viscosity of the thick mucus in the lungs of cystic fibrosis patients will help patients breathe easier, reduce

recurring bacterial infections, reduce scarring, and improve overall lung function.

Acknowledgments:

National Science Foundation, NNUN REU Program, Stanford Nanofabrication Facility, Mary Tang, Samar Hubbi, Michael Deal, and Jane Edwards.

References:

- [1] Lewin, Benjamin. Genes VII. New York: Oxford University Press, 2000.
- [2] Schena M, Heller RA, Theriault TP, Konrad K, Lachenmeier E, Davis RW. 1998. Microarrays: biotechnology's discovery platform for functional genomics. Trends Biotechnol 1998 Jul;16(7):301-306.
- [3] Puchelle E, Zahm JM, de Bentzmann S, et al. Effects of rhDNase on purulent airway secretions in chronic bronchitis. Eur Respir J. 1996;9:765-9.
- [4] Woodward, Roger. Surface Tension Measurements Using the Drop Shape Method. First Ten Angstroms. Accessed: 25 Sept 2001.
<http://www.firsttenangstroms.com/assets/pdfdocs/STPaper.pdf>
- [5] <http://www.aceglass.com/html/products/7985.html>

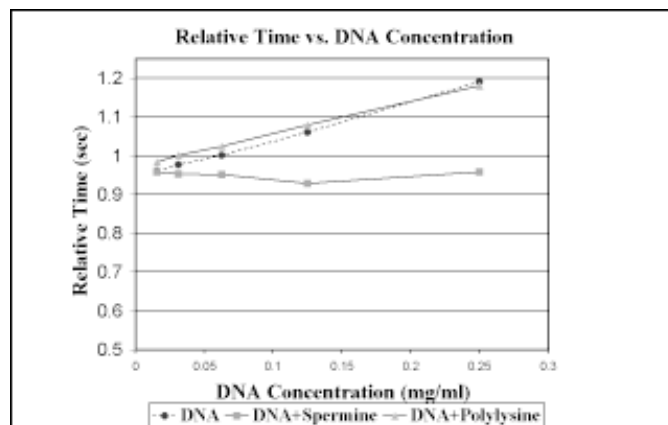


Figure 2: Graph of relative viscosity measurements made using an Ostwald Viscometer (Figure 1c).

Microfluidics for DNA Pyrosequencing

Jon Schuller, Physics, UC Santa Barbara, schuller@umail.ucsb.edu

Principal Investigator(s): Peter Griffin, Department of Electrical Engineering, Stanford University, Griffin@stanford.edu

Abstract:

Due to the cost of manufacturing biological chemicals, pyrosequencing is an expensive procedure. Miniaturizing the process could decrease the cost and timescale of gene sequencing. At present, accurate sequencing on microchips is limited to short DNA molecules (approx. 40 base pairs) because of enzymatic buildup. Microchannels and microsieves were designed to contain DNA molecules while allowing buffer solution to flow through a microchip. We hope to present a novel method for printing DNA samples into a microarray, as well as increase the length of accurately sequenced DNA molecules by an order of magnitude or more. This method has the potential to make gene sequencing and identification quicker, more accurate, and less costly.

Introduction:

Pyrosequencing has proven to be a cheap, simple, and accurate method of DNA sequencing. In a simple overview, pyrosequencing process is basically a multi-step process. First, a single strand of DNA is immobilized on a substrate. The DNA sample is then immersed in a buffer solution containing various enzymes. Next, a particular nucleotide, or DNA base, is added to the buffer solution. If the base is attached to the DNA sample, the reaction produces a flash of light that is recorded by a photodetector. If the reaction does not produce a flash of light, another one of the four bases

(A,C,G,T) is added until a flash of light is produced. The flash of light thus indicates which base is incorporated and gives the sequence of bases in the DNA. Finally, the excess nucleotides and reagents are cleared out, and the process is repeated until the entire DNA sample has been sequenced [1].

This study focused on improving the pyrosequencing process in three different areas: cost, accuracy, and time. The largest contributor to the cost of pyrosequencing is the amount of reagents necessary to ensure that added bases are quickly and accurately incorporated in the DNA sample. Miniaturizing pyrosequencing onto a scale compatible with microfabrication techniques reduces the quantity, and thus cost, of the nucleotides and reagents used in the process. Once miniaturized, the process can be made less costly again, by increasing the density of DNA samples that are processed on a single chip. Finally, the process can be made more accurate for long sequences of DNA by improving the removal of excess nucleotides and reagents. A chip was designed to improve the pyrosequencing process by targeting the above areas.

Design and Operation:

The chip design consisted of an array of several DNA reaction targets, and incorporated microfluidic channels as the primary method for introducing nucleotides and buffer solution as well as introducing DNA into the array. Electrokinetic flow has been demonstrated in other micro-scale DNA sequencing platforms [2] and was chosen as our method of controlling flow within the channels. Sieve-structures were designed to contain DNA samples attached to large silicon beads, while allowing buffer solution containing the pyrosequencing reagents to flow freely past the DNA samples.

To produce an array, a DNA sample is attached to a streptavidin coated silicon bead and placed in a buffer solution. The solution is pipetted into the main-line channel, via the main well. Electrodes are attached to the main well and one of the outflow wells. A bias is applied between the two wells, and the electrokinetic flow carries DNA coated bead towards the outflow well. The bead is too large to fit through the sieve and is trapped at the reaction target. The process is repeated until all reaction targets contain DNA coated beads.

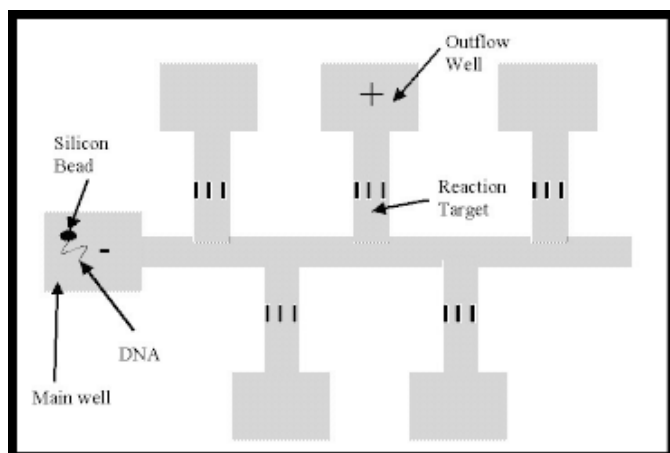


Figure 1: Demonstration of DNA introduction technique on the chip design.

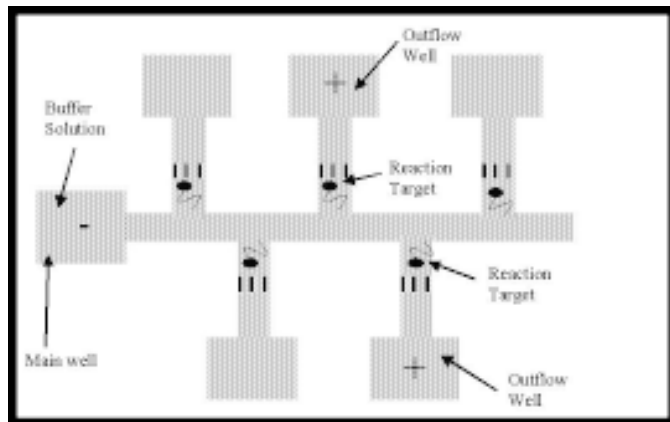


Figure 2: Demonstration of sequencing technique on the chip design.

To sequence on the chip, a buffer solution containing all the necessary nucleotides, enzymes, and reagents is pipetted into the main well. A bias is applied between the main well and any combination of outflow wells. Because the flow is laminar [3], the buffer solution can only access reaction targets where a bias has been applied. A CCD camera records any light from nucleotide incorporations. The buffer solution continues to flow to the outflow well where it no longer interferes with subsequent sequencing reactions. In this manner, any combination of DNA samples can be sequenced in parallel.

Experimental Procedure:

The chip design was dry-etched (to maintain the fine features of the sieve at depth) into a silicon wafer. One-millimeter holes, corresponding to the large wells in the silicon, were drilled into a glass wafer. The glass wafer was then bonded anodically to the top of the silicon wafer.

Conclusion and Future Work:

The most notable features on the chip are the sieve structures, which allow for a novel chip operation. The DNA is contained behind the structures while excess nucleotides and reaction products are removed to the outflow wells. The sieves also allow a method of introducing DNA to an array density that is not limited by current spotting or inkjet technologies. The first step in the testing process is to demonstrate successful electrokinetic flow and DNA introduction on beads. In the future, we would like to characterize how varying channel widths and driving voltages affect the accuracy and speed of the pyrosequencing process.

Acknowledgements:

The author would like to thank Peter Griffin and Reza Kasnavi for guidance and supervision in research. The author would also like to thank Mostafa Ronaghi for his expertise in pyrosequencing, as well as Noel Jensen and

Ravi Sarin for their assistance in microfabrication. Finally, the author would like to acknowledge SNF program coordinators Michael Deal and Jane Edwards for their support. This research has been funded by the National Science Foundation and the National Nanofabrication Users Network.

References:

- [1] Ronaghi, Mostafa. "Pyrosequencing Sheds Light on DNA Sequencing" <www.genome.org/cgi/doi/10.1101/gr.150601>, 2001.
- [2] J. Khandurina, T.E. McKnight, S.C. Jacobson, L.C. Waters, R.S. Foote, and J. Ramsey. *Analytical Chemistry*. 2000, 72, 2995-3000.
- [3] P. Gravesen, J. Branebjerg, and O.S. Jensen. *Journal of Micromechanics and Microengineering*. 1993, 3, 168-182.

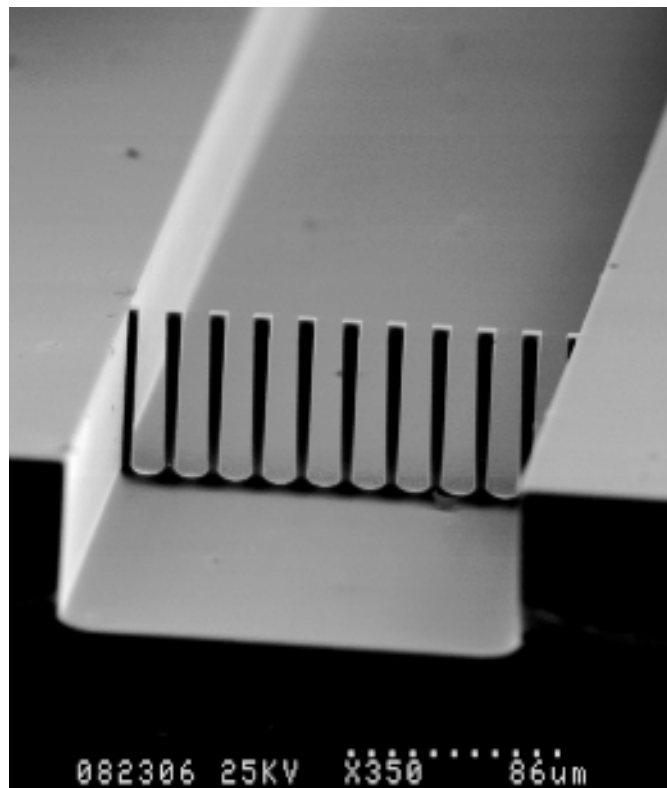


Figure 3: SEM image of a sieve and channel.

Magnetostrictive Thin Films for MEMS Applications

Marina Sofos, Materials Science and Engineering, Brown University,
Marina_Sofos@brown.edu

Principal Investigator(s): Bruce M. Clemens, Department of Materials Science
and Engineering, Stanford University, clemens@soe.stanford.edu

Mentor(s): Mark Phillips, Department of Materials Science
and Engineering, Stanford University

Abstract:

Magnetostrictive thin films offer an attractive approach for remote actuation of micro-electro-mechanical systems (MEMS) devices. Among the candidate materials are amorphous Tb-Fe alloys, which can exhibit large magnetostrictive effects. In thin film form, however, their magnetostrictive and mechanical properties are a function of deposition conditions and can differ significantly from bulk values. We investigated the magnetostrictive performance of amorphous Tb_xFe_{1-x} ($x \sim 0.33$) thin films sputter-deposited onto freestanding silicon nitride micro-cantilever beams with dimensions optimized for magnetostrictive actuation. The coercive fields, magnetization and magnetic anisotropy of the Tb_xFe_{1-x} thin films were determined by vibrating sample magnetometry as a function of film thickness, composition, and deposition parameters. The magnetostrictive actuation can now be measured by optical microscopy in the presence of a magnetic field. This approach can be used to rapidly explore new material systems for magnetostrictive MEMS.

Introduction:

Micro-electro-mechanical systems (MEMS), as their name implies, combine mechanical and electrical functions to create miniaturized devices. Magnetostriction, the deformation of an object due to an applied external magnetic field, can be used to create a remote actuator system by converting an electrical, (in our case magnetic) input signal, into a mechanical output.

Rare-earth/transition-metal binary alloys, such as Tb_xFe_{1-x} are particularly attractive for such applications due to their large magnetostriction. These compounds exhibit perpendicular magnetic anisotropy, resulting in an easy axis of magnetization perpendicular to the film plane, as well as high coercive values. The coefficient for magnetostriction is positive for Tb_xFe_{1-x} between $0.22 < x < 0.5$, reaching zero at each end, with a maximum at $x = 0.4$ of $\lambda_s = 285 \times 10^{-6}$. Because thin films differ significantly from their bulk counterparts, we are interested in the magnetostrictive qualities of Tb_xFe_{1-x} as a function of film thickness, composition, and deposition parameters.

In order to optimize our beam dimensions for appropriate actuation, from Tam and Schroeder, we calculate deflection, d , as:

$$(1) \quad d = \frac{3t_f l^2 \epsilon}{t_s^3} \lambda$$

where l = length, t_f = film thickness, t_s = substrate thickness, and,

$$(2) \quad \epsilon = \frac{E_f(1-\nu_f)}{E_s(1+\nu_f)}$$

where E = elastic modulus, ν = poisson's ratio, and,

$$(3) \quad \lambda = -\frac{3}{2} \lambda_s$$

Deflection increases with the length of the beam and thickness of the film, but decreases as a function of the substrate thickness (Table 1).

	Siliconnitride(a)	TbFe(b)	$t_s(\mu m)$	0.3	1.2	1.2	1.2	0.3
E (GPa)	230	65	$t_f(\mu m)$	0.1	0.1	0.5	0.5	0.5
ν	0.38	0.3	$l(\mu m)$	300	300	300	300	300
λ	0	$2.70E-04$	$w(\mu m)$	30	30	30	30	30
			$d(\mu m)$	0.09	0.08	0.38	2.28	13.9

Table 1. (a) Constant values. b) Theoretical deflection results.

Experimental Procedure:

We grew 0.3 and 1.2 μm of low-stress silicon nitride onto both sides of 4-inch (100) silicon wafers in a Tylan furnace. Beams with varied widths (50, 30, 20 μm) and lengths (300, 200, 100, 50 μm) were patterned onto the polished front side by photolithography using 1.65 μm of 3612 Shipley Positive Resist (Figure 1a). A Freon-13B1 (CF_3Br : 33 sccm) and sulfur hexafluoride (SF_6 : 50 sccm) plasma etch at 200 mTorr and 83 W was used to remove the nitride layer unprotected by photo resist on the top side (Figure 1b). The wafers were placed front side

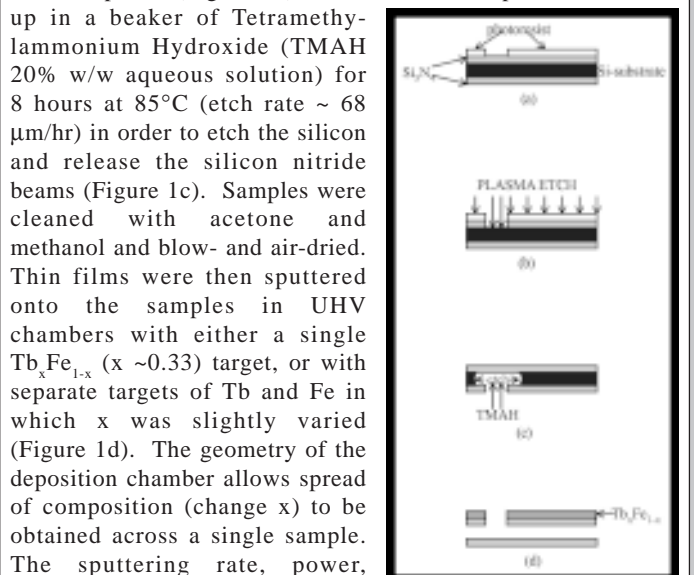


Figure 1. (a-d) Cross-section view of beam creation.

Samples were cut into smaller pieces and hysteresis loops were obtained through vibrating sample magnetometry (VSM). A magnetic field was applied to the beams under an optical microscope and deflections were observed.

Results and Discussion:

Freestanding silicon nitride beams were successfully constructed and recovered (Figure 2a). Beams with widths of $0.3 \mu\text{m}$ did not always survive sample cutting and cleaning. Consequently, greater deflections must be sacrificed for actual beam stability and recovery. A small degree of unavoidable undercutting of the Si substrate resulted from the wet etch (Figure 2b). The beams also deflected slightly due to the residual stress in the metal film after deposition (Figure 2c). TbFe_2 samples grown on Si show an increase in magnetic strength and permanence with rising sputtering pressure (Figure 3). Consequently, the ease of magnetization will become more difficult as the magnetic strength of the film increases.

When films were grown with separate Tb and Fe targets, a difference in composition and magnetization along a sample was obtained. We find that at $x \sim 0.4$, the beams will reach higher saturation values, while remanence and coercivity will be fairly similar to $x \sim 0.3$ samples (Figure 4).

Conclusions:

We successfully constructed freestanding silicon nitride micro-cantilever beams with $\text{Tb}_x\text{Fe}_{1-x}$. A spread in x indicates a variance in the magnetization and magnetic anisotropy of the films. Small deflections have been observed in an optical microscope set up over a magnet. At this time, these deflections have not been measured but work is continuing in building a laser-based apparatus to accurately measure deflections.

Acknowledgements:

I would like to thank my principal investigator Dr. Bruce Clemens, my mentor Mark Phillips, Rajesh Kelekar, as well as the rest of the Clemens research group for their guidance and assistance. I would also like to thank Dr. Michael Deal, Jane Edwards, the SNF Staff, NNUN, and the National Science Foundation.

References:

- [1] Forester, D.W., Vittoria, C., Schelleng, J., and Lubitz, P., "Magnetostriction of Amorphous $\text{Tb}_x\text{Fe}_{1-x}$ Thin Films," J. Appl. Phys., 49(3), p. 1966-1968.
- [2] Hufnagel, T.C., "Structural and Magnetic Anisotropy in Amorphous Terbium-Iron Thin Films," PhD thesis, Stanford University, 1995.
- [3] Tam, A.C., Schroeder, H., "Precise measurements of magnetostriction coefficient of a thin soft-magnetic film deposited on a substrate," J. Appl. Phys., 64(10), p. 5422-5424.

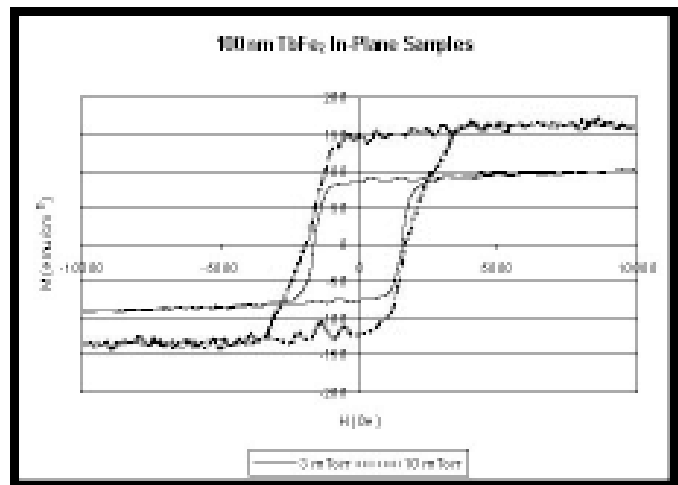


Figure 3: Hysteresis loops as a function of sputtering pressure.
Figure 4: Hysteresis loops as a function of composition.

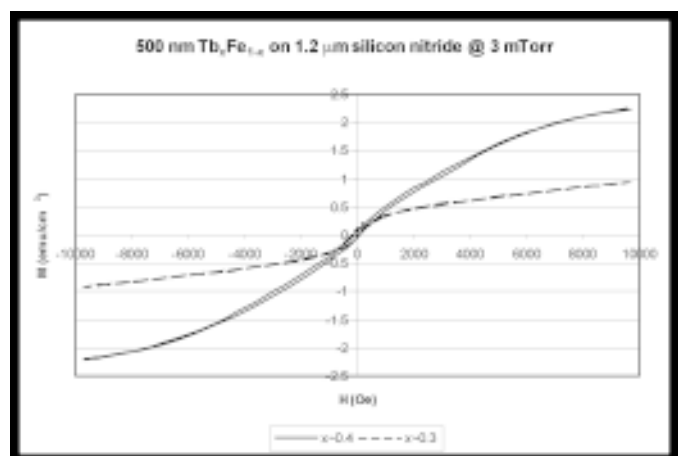
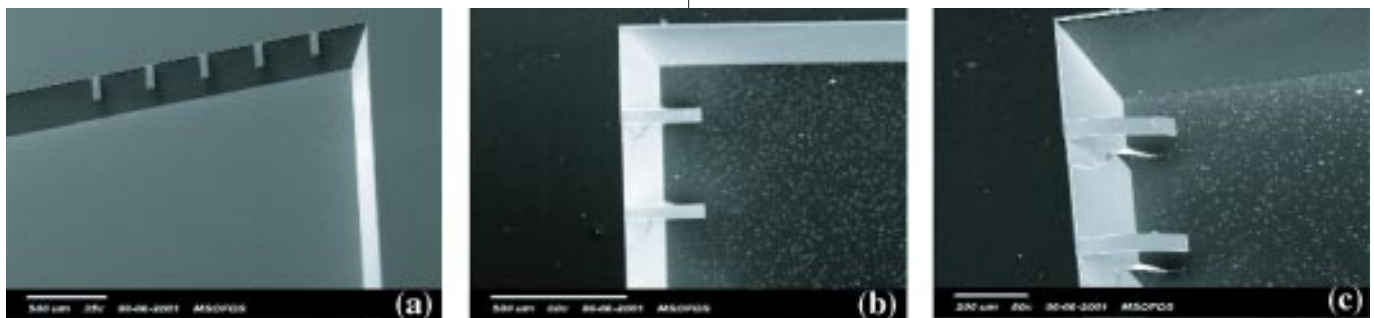


Figure 2, below. (a-c) SEM top-view images of beams.



UCSB Nanofabrication Facility
University of California at Santa Barbara, Santa Barbara CA
<http://www.nanotech.ucsb.edu/>

2001 REU Interns



REU Intern School Affiliation Principal Investigator

Front Row, L to R:

Ms. Hayley Lam	UC Berkeley	Kim Turner
Ms. Nitasha Bakhru	Rensselaer Polytech Inst	Samir Mitragotri
Ms. Linh My Tran	UCLA	Jacob Israelachvili

Second Row, L to R:

Ms. Sara Alvarez	UCSB	Dan Morse
Mr. Lukmaan Bawazer	The Ohio State University	Steve DenBaars
Mr. Peter Ercius	Cornell University	Jacob Israelachvili

Third Row, L to R:

Mr. Chau Tang	University of Southern Mississippi	Guillermo Bazan
Ms. Mary Brickey	University of IL at Chicago	Samir Mitragotri
Mr. Damon Hebert	Macalester College	Pierre Petroff
Mr. Matthew Kittle	University of Michigan	Helen Hansma

Back Row, L to R:

Mr. Albert Flink	UCSB	REU Program Mentor
Ms. Kathleen Schaefer	University of Pittsburgh	Ed Kramer
Mr. Metages Sisay	Santa Clara University	Vojislav Srdanov

Engineering Protein Molecules for the Ordered Structuring of Silica

Sara Alvarez, Microbiology, University of California, Santa Barbara,
saraa@umail.ucsb.edu

Principal Investigator(s): Daniel E. Morse, Molecular, Cellular, and Developmental Biology, University of California, Santa Barbara, d_morse@lifesci.ucsb.edu

Mentor(s): Jan Sumerel, Marine Science Institute, UCSB

Abstract:

The nanofabrication control of biosilica structures, in many instances, exceeds the present capabilities of material engineering. Analysis of occluded proteins from the biosilica spicules produced by the marine sponge, *Tethya aurantia*, has revealed that these proteins act catalytically in directing the condensation of polysiloxanes from silicon alkoxides under mild physiological conditions. This contrasts the chemical synthesis of silicon-containing materials which requires acid or base catalysis or extreme temperature and pressure. Silicatein α has been isolated from the protein axial filament of the sponge spicule, and its respective cDNA has been cloned.

Professor Morse and his lab members have shown that recombinant silicatein α catalyzes the hydrolysis of tetraethoxysilane (TEOS) to form $(\text{SiO}_2)_n$ at neutral pH *in vitro*. Investigations are underway to mimic the silicateins for silica deposition control on the nanoscale. This report discusses making a chimera between silicatein α and green fluorescent protein (GFP) to allow the silicatein to have a fluorescent component during lithography. After generating the chimera, bacterial cells were transfected with the plasmids and clones were screened for proper orientation using restriction analysis. A chimera was found; however, the GFP is in the noncoding direction. Future work includes generating properly oriented clones.

Introduction:

Living systems produce a remarkably diverse representation of exquisite silica structures, as seen in diatoms, sponges, and plants. Architectural control of these glass structures, in some instances, is directed at the molecular level by proteins present in the organism. For example, in the marine sponge, *Tethya aurantia*, 75% of the organism's dry weight consists of silica spicules that enclose a macroscopic proteinaceous axial filament. The filament is composed primarily of two protein subunits, and the cDNAs of these proteins have been cloned [1]. These proteins, silicateins α and β , are highly homologous to members of the Cathepsin L protease family. The high degree of similarity and amino acid conservation at critical positions in the molecule, taken

together with the structural information of Cathepsin L family members, suggest a tertiary structure for silicateins α and β [1].

Professor Morse's group has shown that the silicatein filaments and their respective subunits catalyze the *in vitro* polymerization of silica and silsesquioxanes from tetraethoxysilane and silicon triethoxides, respectively, at neutral pH and ambient temperature and pressure [2]. This physiological route for polysiloxane synthesis offers new approaches for environmentally favorable manufacturing of novel silicon materials, creating applications in siloxane-based semiconductors, glasses, optical fibers, and additional silicon-based materials.

Using the lessons learned from silicatein α , a goal of the laboratory is to modify silicatein α for improved structural control, in order to direct synthesis of highly ordered silicon-containing materials. To monitor silicatein α coupled to a surface, a fluorescently labeled silicatein is required. A fusion was made between silicatein α and green fluorescent protein (GFP) using genetic engineering techniques. This fluorescent molecule will assist in the investigation of the structure-directing properties of silicatein α during synthesis-directed activities.

Experimental Procedure:

To create a silicatein α /GFP chimeric protein, a fusion was made between their corresponding DNAs (cDNAs). A Hind III restriction site exists at the 3' end of the silicatein α cDNA. Therefore, in order to fuse the GFP cDNA at the 3' end of silicatein α , Hind III restriction sites were engineered at each end of the GFP cDNA. A Hind III restriction site at the 3' end was generated using the Polymerase Chain Reaction with appropriate primers that amplify the DNA while simultaneously generating a Hind III site.

The modified GFP fragment was used in an *in vitro* ligation reaction with a silicatein α plasmid that had also been linearized with Hind III. This cloning was nondirectional; the GFP fragment had Hind III sites at each end. Therefore, once transformed into bacterial cells for propagation followed by selection, three types of colonies would arise: no GFP insert, GFP inserted in the noncoding direction leading to no GFP expression, and

GFP inserted in the proper direction necessary for correct protein expression.

Sixty-four colonies were selected and screened. The plasmids with the different insert combinations were genetically mapped by restriction analysis using restriction enzymes, Bst^{II} and Hpa^I (Figure 1). The plasmid with correct directionality would release a 1,080 base pair fragment. The plasmid with incorrect directionality would release a 760 base pair fragment. One clone, #7 S.A., was found with the incorrect silicatein α /GFP conformation but, otherwise, was genetically correct (Figure 1, Lane 4). Further restriction analysis was performed to correctly map the plasmid by using combinations of enzymes Bst^{II}, Hpa^I, and Hind^{III} (Figure 2).

Results and Conclusions:

Restriction analysis on #7 S.A. mapped and confirmed the sequence of this chimera. Because all the other genetic components of this plasmid are correct, further work will include isolating the GFP fragment and reintroducing it into the silicatein α vector to obtain proper GFP orientation. Once correctly oriented, clones will be isolated, chimeric proteins will be synthesized in the bacteria and then purified. The resulting fluorescent proteins will be linked to thin films in ordered microarrays to study silica deposition and control.

References:

- [1] Shimizu, K., Cha, J., Stucky, G. D. & Morse, D. E. (1998) Proc. Natl. Acad. Sci. USA 95, 6234-6238.
- [2] Cha, J., Shimizu, K., Zhou, Y., Christiansen, S. C., Chmelka, B. F., Stucky, G. D. & Morse, D. E. (1999) Proc. Natl. Acad. Sci. USA 96, 361-365.

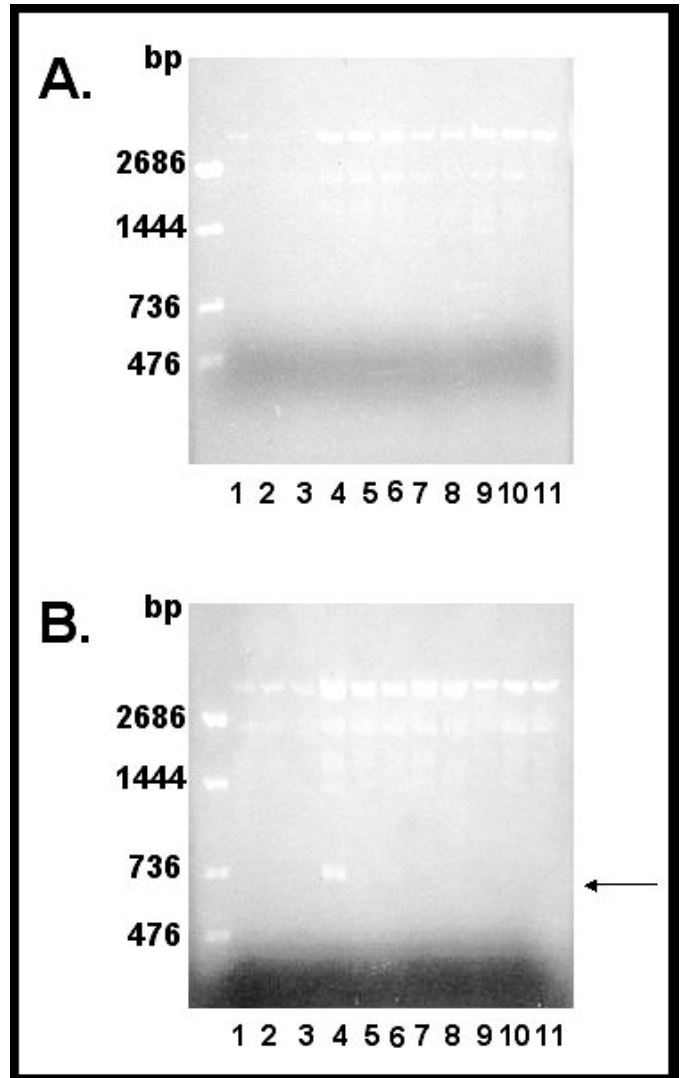


Figure 1, above: Ethidium bromide staining after DNA gel electrophoresis. Plasmid DNA was purified from bacterial cells and subjected to enzyme digestion with Hpa^I and Bst^{II}. Resulting digests were electrophorised on a 1.2% agarose gel and stained with ethidium bromide. The DNA fragment size marker is in the first lane of each gel. Gel A, Lanes 1-11: No inserts of the correct size. Gel B, Lanes 1-3: No inserts of the correct size. Lane 4: Correct size fragment (see arrow). Lanes 5-11: No inserts of the correct size.

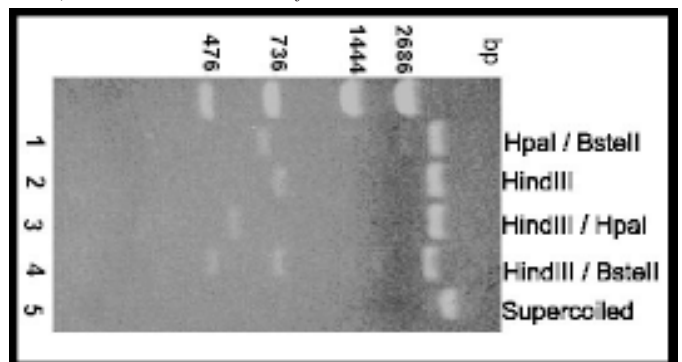


Figure 2, above: Restriction analysis and mapping of potential clone, SA#7. Ethidium bromide staining after DNA gel electrophoresis. Plasmid DNA was purified from bacterial cells and subjected to enzyme digestion with Hpa^I and Bst^{II} and Hind^{III}. Resulting digests were electrophorised on a 1.2% agarose gel and stained with ethidium bromide. The DNA fragment size marker is in the first lane. Lane 1: SA#7 digested with restriction enzymes Hpa^I and Bst^{II}. Lane 2: Hind^{III}. Lane 3: Hind^{III} and Hpa^I. Lane 4: Hind^{III} and Bst^{II}. Lane 5: Undigested.

The Effects of Penetration Point on Quantitative Drug Delivery by Jet Injection

Nitasha Bakhru, Biological Sciences, Rensselaer Polytechnic Institute,
bakhnr@rpi.edu

Principal Investigator(s): Samir Mitragotri, Dept. of Chemical
Engineering, UCSB, samir@engineering.ucsb.edu

Mentor(s): Joy Schramm, Chemical Engineering, UCSB

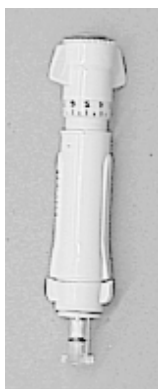
Abstract:

Though modern medicine has rapidly improved throughout the years, we are still challenged by one of the most fundamental applications, that involving the delivery of drugs to patients. Jet injectors propose an alternative to the use of needles to deliver macromolecular drugs through the use of a high velocity jet that can penetrate the skin. This research, focused on observing penetration point and fluid dispersion in skin, is being undertaken to understand the fundamental mechanisms of jet injection.

A Franz diffusion cell was used to test the conductivity changes in porcine skin at room temperature. The conductivity changes were caused by penetrating the skin with needles of diameters ranging from 0.45 to 1.27 mm. It was observed that conductivity linearly escalated with increasing needle area. Fluid dispersion through skin was also observed by injecting a dye into the dermis. By slicing the skin and imaging it, it was noticed that fluid dispersed more significantly in the horizontal direction. In fact, the width of the delivered fluid in skin was approximately 2.5 times greater than the depth. When a jet injector was used to deliver the fluid, the width/depth aspect ratio remained nearly the same. However, it could be seen that the fluid dispersed more evenly in skin when injected via a jet injector than through a needle. Further investigations into the mechanics of the penetration point of injection will hopefully aid in gaining more knowledge about quantitative drug delivery and the eventual development of an improved painless, needleless jet injector.

Introduction:

Research in the field of drug delivery is especially pertinent in the lives of diabetic people. Diabetics must inject themselves with insulin on a daily basis which can become very painful and difficult for the patient. Therefore, other methods of drug delivery have been looked upon with hopes of providing a less painful form of delivery. However, most of these methods have encountered some form of a barrier. For example, oral delivery has been difficult due to first-pass metabolism caused by the poor stability of macromolecular drugs such as insulin in the gastrointestinal tract. Mucosal



delivery has met the barrier of the mucous membranes. Transdermal delivery has been hindered by the stratum corneum's impermeability to macromolecules. Since the invention of jet injectors in 1947, they have been hoped to traverse the border of patient compliance and efficiency. It is our focus to understand the fundamental mechanisms of jet injection in hopes of developing an improved device. (Fig. 1)

Figure 1: Image of a commercial jet injector.

Experimental Procedure:

The research focused on examining the penetration point size of injection and fluid dispersion through skin. The size of the penetration point was measured by penetrating skin with differing needle gauges. Conductivity through the penetrated skin was then measured and correlated with the area of the needle used. Needles ranged in size from 18-26 gauge. A Franz diffusion cell was used for the conductivity measurements. A piece of skin that was penetrated with a specific needle gauge was placed between the two chambers. Voltage was applied across the chambers containing electrodes and the current was measured. The conductivity change was then plotted with needle area.

Fluid dispersion through skin was also observed. Skin was injected by needles attached to a syringe pump which kept the speed of injection constant. After injection, the skin was sliced in half at the penetration point and a picture of it was taken. The picture was then processed in Adobe Photoshop. Different concentration thresholds

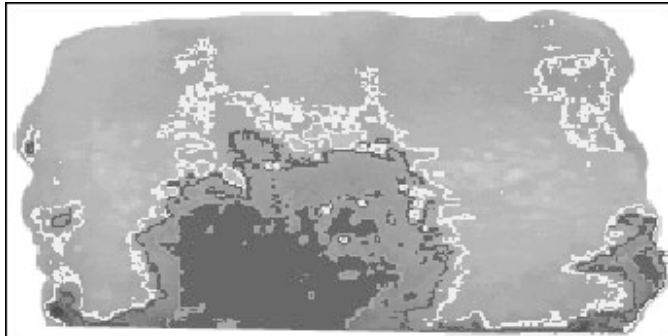


Figure 2: Skin sample processed in Photoshop showing different threshold intensities.

within the skin were examined by measuring the width and depth of each. The aspect ratio of the width/depth was then plotted as well as the depth vs. threshold intensity. (Figure 2)

Results And Conclusions:

It was observed that the conductivity change through skin (kOhm)-1 was linearly related to increasing needle gauge size. It linearly escalated through the equation $y = .429x + .1097$. The experimental values matched the theoretical calculations with a difference in slopes of 11% and a shift of intersection point by 0.11. (Figure 4) The theoretical line is a model of the conductivity of a column of PBS at a given height and cross-sectional area of the needle. Examining penetration point size of a needle by observing conductivity change provides a promising method for measuring penetration point size by jet injection. Fluid dispersion through skin was also observed. There appears to be a horizontal directionality to the skin. By injecting fluid from different directions, an approximately constant width/depth aspect ratio of 2.5 was observed. Measurement of the fluid dispersion in response to changing flow rates was originally attempted. However, results showing a range of flow rates that yielded significantly different values were not achieved. It could also be noted that the dispersion depth was non-linearly related to the threshold intensities. (Figure 3)

Future Work:

Future work must be done to visually confirm the size of the injection point made by the jet injector. This can be accomplished through gathering data on the conductivity change through skin after penetration by the injector.

Future work concerning the study of fluid dispersion can be done as well. The effects of differing delivery forces can also be studied to more fully understand the dispersion mechanism. The closure of the penetration hole as time elapses may also be studied.

Acknowledgements:

Thanks to my mentor, Joy Schramm, for all her patience and help; Samir Mitragotri for his aid; the National Science Foundation and the National Nanofabrication Users Network; and the UCSB crew of interns.

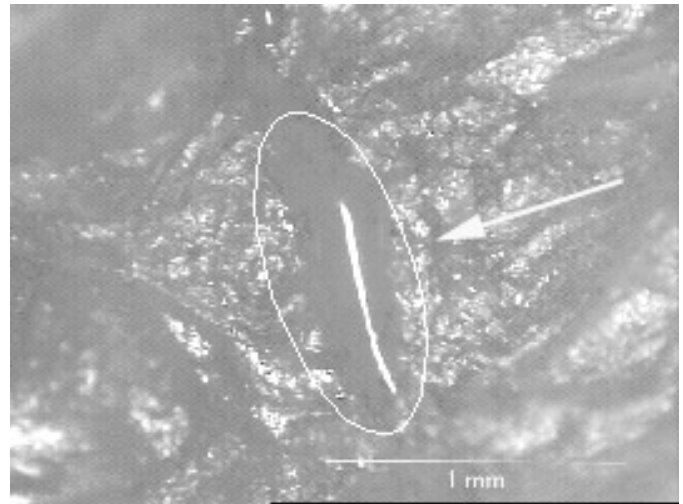
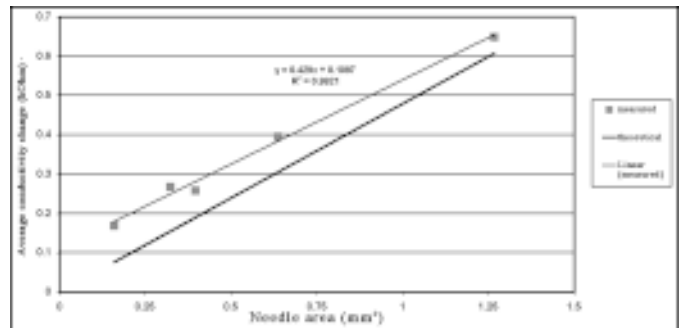


Figure 3, above: Magnified image of hole created by injector.
Figure 4, below: Graph showing how conductivity linearly escalates with increasing needle area of penetration.



Evaluation of Novel Growth Techniques for Dislocation Reduction in Gallium Nitride

Lukmaan Bawazer, Materials Science and Engineering, Ohio State University,
lbawazer@hotmail.com

Principal Investigator(s): Steven DenBaars,
Materials Department, UCSB, denbaars@engineering.ucsb.edu

Mentor(s): Thomas Katona, Electrical and Computer Engineering Department, UCSB

Abstract:

We characterized gallium nitride (GaN) thin films grown on Si(111) substrates via the cantilever epitaxy (CE) technique to determine the relationship between wing aspect ratio and crystallographic tilt. The CE technique involves growing GaN by metalorganic chemical vapor deposition (MOCVD) on substrates patterned with periodic grooves. X-ray diffraction was used to measure crystallographic tilt of the wings from the mesa regions. Scanning electron microscopy (SEM) was used to characterize the wing aspect ratios. It was determined that a linear relationship exists between the wing aspect ratio and wing tilt, but this relationship only holds if the lateral growth rate is held constant during growth.

Introduction:

Gallium nitride is a wide band-gap (3.4 eV) semiconductor that has important applications for optoelectronic devices, such as blue LEDs, laser-diodes, and UV photodetectors. Threading dislocations (TDs) have adverse effects on the electronic properties of these vertically conducting devices [1]. TDs are formed in GaN due to differences in lattice constants and coefficients of thermal expansion between GaN and its substrates, typically sapphire, SiC, and Si(111). The dislocations originate at the GaN-substrate interface. Novel, selective-area growth techniques have been employed to reduce these defects in areas of GaN thin films.

Lateral epitaxial overgrowth (LEO) is a technique where growth is performed on a partially masked GaN seed layer [2, 3]. GaN grows vertically through the windows in the mask and then laterally over the masked area. The mask prevents TDs from propagating vertically into the lateral overgrowth regions.

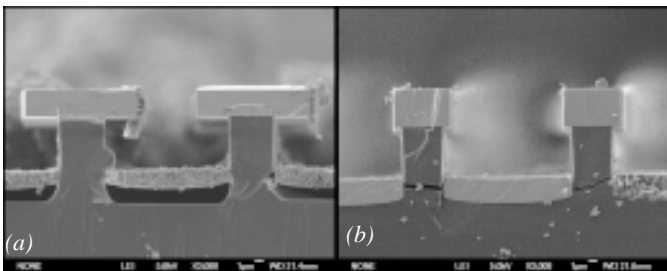


Figure 1: Cross-sectional SEM photos of Cantilever Epitaxy GaN on Si(111). a) Growth E from CE Group 2 b) Growth D from CE Group 2.

One problem that has been observed in LEO is crystallographic tilting of the wings (the laterally grown regions) away from the window regions. When adjacent wings with crystallographic tilt coalesce, arrays of dislocations form at the wing-wing interface. The origin of this wing tilt is unknown, but some evidence points to interfacial forces between the mask and GaN [3]. It has been shown that crystallographic tilt is related to the geometrical aspect ratio of the wings [3]. Cantilever epitaxy (CE) yields low-defect GaN similar to that grown by LEO, but requires only one MOCVD growth [4]. CE also has no wing-mask interface and it was thought this might eliminate wing tilt.

In CE, GaN begins growing vertically on the mesas of a stripe-patterned substrate and then laterally over the trenches (see Figure 1). The wings show similar defect reduction to that seen in LEO wings. Although CE GaN has no wing-mask interface, recently wing tilt has been observed [5]. In the present study, various ammonia flow rates were used to produce CE samples on Si(111) substrates with a range of width to height (w/h) wing aspect ratios. The samples were characterized by x-ray diffraction and SEM. The relationship between the w/h ratio and wing tilt was examined. These results were compared with similar a study on LEO material.

Experimental Procedure:

Reactive ion etching (RIE) was used to pattern the substrates with alternating mesas and trenches. Trimethylgallium (TMGa) was used as the gallium gas source and ammonia was used as the nitrogen gas source. The MOCVD growth conditions for the samples are presented in Table I. After the growths, the samples were cleaved perpendicular to the stripe direction, and a JEOL 6340 SEM was used to obtain cross-sectional micrographs of the GaN thin films. These micrographs were used to measure the w/h of the samples. To measure wing tilt, x-ray rocking curves of the GaN 0002 peak were recorded using Ge(220)-monochromated Cu k- α radiation in a four-circle diffractometer operating in receiving slit mode, with a 1.2mm slit on the detector arm. Rocking curves were recorded with the scattering plane perpendicular to the stripe direction.

Results and Conclusions:

Figure 2 presents wing tilt plotted against w/h for the CE growths Group 1 and Group 2 of this study, as well as for a similar study on LEO material by P. Fini et al [3]. CE-Group 1 and the LEO study exhibit a linear relationship between w/h and wing tilt, both relationships having a similar slope. CE-Group 2 does not follow this linear relationship.

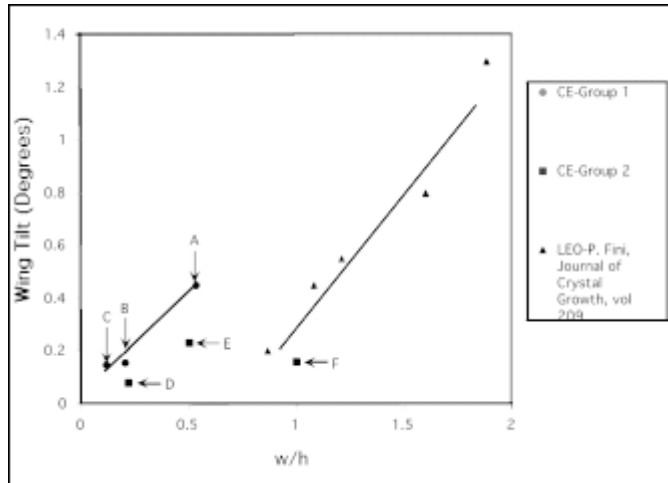


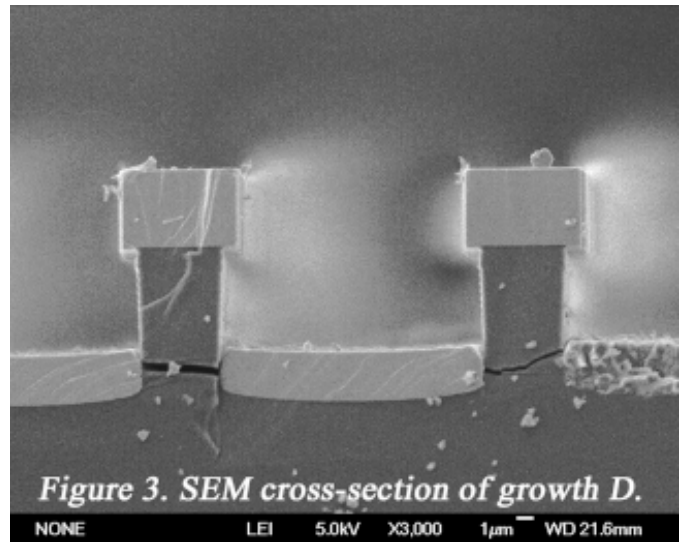
Figure 2: Effect of wing geometry on tilt.

As ammonia flow increases, the extent of lateral growth also increases, yielding a higher w/h ratio. For each growth of CE-Group 1 and the LEO study, the ammonia flow rate, and thus the lateral growth rate, was held constant throughout the lateral growth step. In CE-Group 2, growths D and E had the same growth conditions during the first 30 minutes of growth. The increased ammonia flow for growth E during the second 30 minutes of growth led to a relatively large increase in lateral growth, as can be seen by comparing growth E in Figure 1 to growth D in Figure 3.

While growth E has a much larger w/h ratio than growth D, the corresponding increase in wing tilt of growth E is much less than that predicted by the slope established by CE-Group 1 and the LEO study. That is, the second growth step significantly affected the w/h of growth E, but did not significantly affect wing tilt. It is thus concluded that the wing aspect ratio does affect wing tilt, but the initial lateral growth rate sets a relative magnitude for the tilt. If lateral growth rates are changed later in the growth the effect on tilt is not as drastic.

References:

- [1] G. Parish, S. Keller, P. Kozodoy, J.P. Ibbetson, H. Marchand, P.T. Fini, S.B. Fleischer, S.P. DenBaars, U.K. Mishra, E.J. Tarsa, *Appl. Phys. Lett.* 75 (1999) 247.
- [2] A. Usui, H. Sunakawa, A. Sakai, A.A. Yamaguchi, *Jpn. J. Appl. Phys.* 36 (1997) L899.
- [3] P. Fini, H. Marchand, J.P. Ibbetson, S.P. DenBaars, U.K. Mishra, J.S. Speck, *Journal of Crystal Growth* 209 (2000).
- [4] C.I. Ashby, C.C. Mitchell, J. Han, N.A. Missert, P.P. Provencio, D.M. Follstaedt, G.M. Peake, L. Griego, *Appl. Phys. Lett.* 77 (2000).
- [5] T.M. Katona, M.D. Craven, P.T. Fini, J.S. Speck, S.P. DenBaars, *Appl. Phys. Lett.*, to be published 10/29/2001.



Cavitation Surface Effects of Low Frequency Ultrasound

Mary C. Brickey, Biochemistry, University of Illinois at Chicago,
marybrickey@hotmail.com

*Principal Investigator(s): Dr. Samir Mitragotri, Chemical Engineering,
University of California Santa Barbara, samir@engineering.ucsb.edu*

Mentor(s): Ahmet Tezel, Chemical Engineering, University of California Santa Barbara

Abstract:

In order to discover the mechanism by which transient cavitation increases skin permeability and deforms surfaces, deformations were observed on aluminum foil after exposure to various intensities of low frequency ultrasound. A threshold intensity was required for pits to form on the foil, above which, the amount of pitting increased, in general, with intensity. Decreases in the number of pits suggested the occurrence of acoustic decoupling. The pit size was 45 times larger than the average microjet size at similar conditions, indicating the large force of the bubbles and possible cumulative interactions between them. Data produced will allow for the calculation of the energy imparted on the surface by transient cavitation.

Introduction:

Low frequency ultrasound has potential as an agent for transdermal drug delivery of high molecular weight drugs, such as insulin. Low frequency ultrasound, around 20-40 kHz, has been shown to increase the permeability of skin to insulin by 400 times [2]. At this frequency, ultrasound application visibly deforms the surface to which it is exposed. Both of these effects are due to transient cavitation [6]. Transient cavitation is the oscillation of size and spontaneous collapse of gas bubbles in the liquid medium, due to the passing of pressure waves. Collapse near a surface causes the formation of a microjet. It was hypothesized that these microjets supplied the force driving large molecules across the surface of the skin, as well as causing pits seen on aluminum foil. A major purpose of this work was to provide data that will later allow the calculation of this force.

Procedure:

A foil of medium strength, brand name: American Fare, was carefully cut into squares of approximately 9 cm². The dull side of the foil was placed upward in a standard Franz diffusion cell with Phosphate Buffered Saline below and above the foil. A rubber washer, with a thickness of about 3.4 mm, was placed directly above the foil to reduce cavitation effects at the junction of the glass cell and aluminum foil. Ultrasound was applied

using custom-built transducers. The signal was produced by a signal generator and an amplifier. An inductor was connected in parallel. Power, current, and voltage were measured with a wattmeter.

A transducer with an operating frequency of 77.2 kHz was placed 5 mm above the foil. Ultrasound was applied for 2 minutes at power ranging from 0.1 to 2.6 Watts. Trials were performed at intervals of 0.1 Watts until four resulting foils with countable results were obtained at each interval. Intensity (I) was calculated using the formula:

$$I = \text{Power}/(\text{cross sectional area of transducer})$$

These pieces of foil were viewed with a 5x objective. Pit radius was measured with a scaled retical.

Results and Discussion:

Amount of Pitting - No pitting occurred below the intensity of 2.42 W/cm². Above this threshold, the number of pits increased with increasing intensity. This was most likely due to an increase in the number of cavitation bubbles collapsing near the surface. Beyond 2.93 W/cm², large holes were made in the foil, which prevented the measurement of surface effects at these high intensities.

A local maximum of pitting was observed at 2.68 W/cm². This is emphasized in Graph 1, which illustrates the relationship between the number of pits made and intensity of ultrasound. The immediate decrease in pitting after this peak is most likely due to a decrease in the number of bubbles reaching the surface. This phenomenon has been observed previously as a decrease in the conductivity enhancement of skin exposed to ultrasound. Termed "acoustic decoupling", this effect is due to the presence of many cavitation bubbles directly under the transducer, which prevents the propagation of the ultrasound wave through the medium [4]. At intensities higher than 2.93 W/cm², the increasing trend resumed.

Size of Pits - The average radii of the pits formed did not vary as obviously as the number of pits. This can be seen by comparing Graph 1 and Graph 2, which illustrates the relationship between pit radii and intensity. Pit radius did maximize slightly at 2.68 W/cm², just like the amount of pitting. It is unlikely that this reflects an increase in

the size of cavitation bubbles because oscillations of size are dependent only on the frequency of ultrasound, which remained constant in these experiments. But according to acoustic decoupling, a maximum amount of bubbles reached the surface at this intensity. It follows that bubbles would have been closer to one another. Therefore, the larger pit radius may have been caused by the cumulative microjet force of multiple bubbles in close proximity to one another. This is a plausible explanation, considering the relatively small size of the microjets compared to the pit radii. Average pit radii ranged from 85 to 92 micrometers. This is nearly 45 times larger than individual microjets created at 77 kHz, which have radii of 2 to 3 micrometers [4].

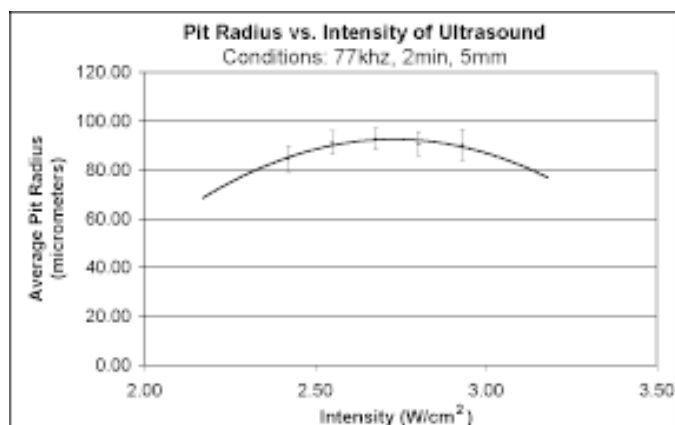
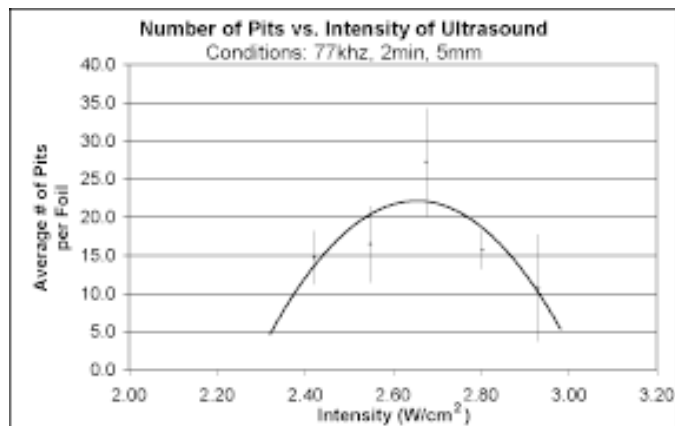
The data collected should be used in conjunction with the known mechanical properties of aluminum foil. Potentially, the energy expenditure of cavitation on the surface of foil can be calculated and compared to energy required in the deformation of actual skin.

Acknowledgments:

This research was funded by The Juvenile Diabetes Foundation and The Center for Disease Control and Prevention. This internship was provided by National Nanofabrication Users Network, supported by The National Science Foundation. Also, Dr. Samir Mitragotri, Ahmet Tezel, and Ashley Sens of the University of California Santa Barbara graciously lent a significant amount of time and expertise to this project.

References:

- [1] Kost, J., Pliquett, U., Mitragotri, S., Yamamoto, A., Langer, R., Weaver, J, "Synergistic Effect of Electric Field and Ultrasound on Transdermal Transport", *Pharm. Res.*, 13:4, 633-638, 1996.
- [2] Mitragotri, S, Kost, J., and Langer, R., "Non-Invasive Drug Deliver and Diagnostics Using Low-Frequency Sonophoresis", *Recent Advances and Research Updates*, 1:43-48, 2000.
- [3] Mitragotri, S., Ray, D., Farrell, J., Tang, H., Yu, B., Kost, J., Blankschtein, D., and Langer, R., "Synergistic Effect of Ultrasound and Sodium Lauryl Sulfate on Transdermal Transport", *J.Pharm.Sci.* In Press.
- [4] Suslick, K.S. 1989. *Ultrasound: Its Chemical, Physical, and Biological Effects*, VCH Publishers.
- [5] Tezel A, Sens A, Mitragotri S. 2001 "Investigations of the Role of Cavitation in Low-Frequency Sonophoresis using Acoustic Spectroscopy", Submitted.
- [6] Tezel A, Sens A, Tuchscherer J, Mitragotri S. 2001 "Frequency Dependence of Sonophoresis", Submitted.



Development of a C++ Program to Study Five-Layer, Thin-Film Systems using Multiple Beam Interferometry

Peter Ercius, Applied and Engr Physics, Cornell University, ercius@cornell.edu

Linh My Tran, Chemical Engineering, UC Los Angeles, linh@seas.ucla.edu

Principal Investigator(s): Jacob Israelachvili, Chemical Engineering, University of California, Santa Barbara, jacob@engineering.ucsb.edu

Mentor(s): Nianhuan Chen, ChemEng, Rafael Tadmor, Materials Research Lab, UCSB

Abstract:

Our project involves using fringes resulting from constructive interference in an interferometer to measure the thicknesses of a symmetric, five-layer system. Our five-layer system is comprised of one layer of polydimethylsiloxane (PDMS) between two layers of polybutadiene (PBD), which are coated on cylindrical mica substrates. We wrote a C++ program that solves the five-layer interferometry equations to give the thickness of both interstitial liquid layers using Newton method, a numerical method that finds roots of equations.

The program requires input of the wavelength of two successive fringes, three refractive indices (for mica, PBD, and PDMS), and the wavelength corresponding to the single layer mica interferometer. The five-layer equations have multiple solutions; therefore, the program selects the probable answer by comparing the answers to a previous known thickness set. Our program compensates for refractive index dispersion (wavelength dependence of refractive indices) since the solutions are very sensitive to small changes in these values.

Introduction:

Five-layer interferometry is used to study the coalescence of thin films at the molecular level. Understanding liquid-liquid interactions could be helpful in improving applications such as liquid-liquid extractions, emulsification, and polymer blending processes.

The interferometer consists of two cylindrical sheets of mica silvered on the back and arranged in crossed cylinder geometry with three layers of liquids sandwiched between. Each mica surface is coated with a layer of polybutadiene (PBD), and polydimethylsiloxane (PDMS) fills the space between the PBD layers. White light is passed through the mica sheets, which produces an interference pattern of fringes of equal chromatic order (FECO).

This technique can resolve the thicknesses of thin liquid layers with a high degree of accuracy, ideally $\pm 1 \text{ \AA}$ [1]. Analyzing these fringes requires solving the FECO equation for a five-layer interferometer [1]. Since this equation is trigonometric, it is difficult to solve even when using a computer program such as Mathematica.

The process for finding roots of the equation and then selecting the correct root is tedious. The goal of our project was to construct a C++ program solve the five-layer interferometry equation quickly and efficiently. C++ was a better choice than Mathematica because it allowed for greater flexibility in programming and allowed the process to be much more autonomous.

Discussion:

Data from the FECO fringes is taken by first video taping the fringes (Figure 1). The tapes are then analyzed using a video micrometer that can identify the location of a variable line with respect to a reference line. With two lines of known, constant wavelength and their arbitrary positions, we can convert the locations of two successive fringes into a difference in wavelength that is used to calculate the thicknesses of the liquids from the FECO equation.

Figure 1. Inverted image of fringe pattern.

To solve the FECO equation, our program implements the Newton numerical method [2]. The method is modified to avoid diversion and to ensure all solutions are found. To find all the solutions, the program starts with an arbitrary interval with a lower bound of 5 \AA and an upper bound of 5 \AA . If the iterations place the root outside of the bracketed interval, the program stops iterating and moves to the next interval, 0 to 10 \AA .

Excessive iterations in each interval ensure that no solutions near the upper or lower bounds are skipped over. Also, the bracketed interval avoids any diversions that might occur during the process. The final interval varies and is a function of the total calculated thickness of all three interstitial liquid layers.

Since the five-layer equation is trigonometric, it is sometimes necessary to add pi to arrive at the correct thickness. The range of a computer's arc tangent function lies in the first and fourth quadrants only. The fourth quadrant consists of negative angles, which are not reasonable for describing real situations. It is therefore necessary to add pi to these negative angles to convert them into positive values.

A second condition for adding pi also arises when the thicknesses of the liquids becomes large. The arc tangent cycles to zero every pi radians and causes the calculated thickness to be too small. A pi must be added to the arc tangent for every cycle that it repeats. The program tests for this situation by finding the ratio of the distance the fringe has moved and its original position. The integer value of this ratio corresponds to the number of pi's to be added.

Finally, the program accounts for the wavelength dependence of the refractive indices of mica and the two liquids. This dependence follows the function

$$U(L) = A + B / L^2 \quad [1]$$

where U is the refractive index, L is the wavelength, and A and B are constants unique to a substance.

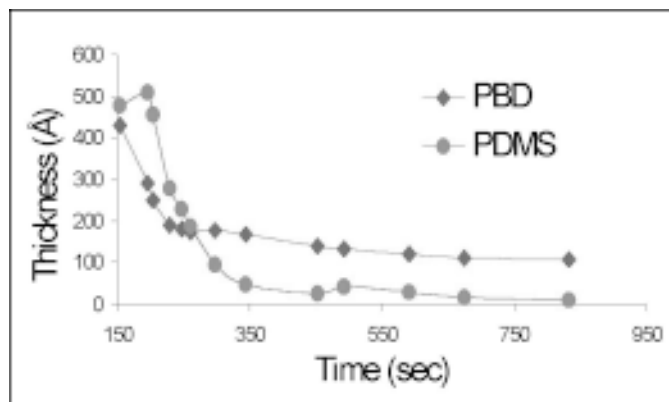


Figure 2. Drainage of PDMS as two surfaces approach at about 300 Å/sec.

Results and Conclusions:

Figure 2 shows a graph of data obtained from the five-layer program. This experiment involved two mica surfaces approaching one another. The PBD and PDMS liquids decrease in thickness initially. The PBD layer remains constant after reaching a critical thickness because it is more viscous than PDMS, and it wets the mica surface. At the end of the graph, the PDMS layer is almost completely drained and only PBD is left between the mica surfaces.

References:

- [1] Israelachvili, Jacob. Thin Film Studies Using Multiple Beam Interferometry. J Colloid Interface Sci. Vol. 44, No. 2, pp. 259-272. (1973)
- [2] Press, William, Teukolsky, Saul, Vetterling, William, Flannery, Brian. Numerical Recipes in C. Cambridge: Cambridge University Press; 1992.

Photoluminescence and AFM on Strain-Coupled, Self-Assembled InAs Quantum Dots and Quantum Rings

Damon N. Hebert, Department of Physics, Macalester College,
dhebert@macalester.edu

Principal Investigator(s): Dr. Pierre M. Petroff,
Materials Department, UCSB, petroff@engineering.ucsb.edu

Mentor(s): Brian Gerardot, Materials Department, UCSB

Abstract:

We characterize the physical and optical properties of self-assembled InAs quantum dots. Two closely spaced layers (45Å-120Å) of quantum dots are grown using molecular beam epitaxy (MBE). We control the electronic energies of the quantum dots using partially capped islands (PCI) whereby the physical dimensions of the quantum dots are controlled by changing growth parameters. In this way, we are able to tune the energies of adjacent strain-coupled layers of quantum dots. We study the size and shape distribution of uncapped InAs islands using the atomic force microscope (AFM). Statistics on quantum dot density, distribution, size, and PCI ratio are recorded. We also measure the optical properties of strain-coupled quantum dots. The goal of this research is to attain control over the MBE growth parameters of self-assembled quantum dots and investigate the electronic coupling of adjacent quantum dots. This research has several possible applications including quantum computation and memory bits.

Introduction:

Recently, work in the field of semiconductor nanostructure fabrication has reached a new dimension. We are able to achieve confinement of carriers in three dimensions with the use of self-assembled semiconductor quantum dots (QDs). Any bound carrier in the QD exhibits discrete energy levels due to the spatial confinement, resembling the properties of an electron in an atom. This technology hopes to contribute to the

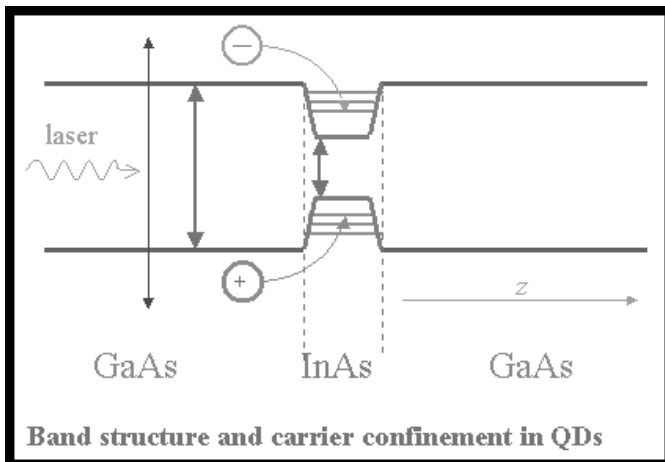
exciting and emerging field of quantum computation in which information is stored and processed using QDs and the spin of a carrier. QDs have also been attractive because their atom-like properties allow the study of fundamental physics of carrier confinement.

Experiment:

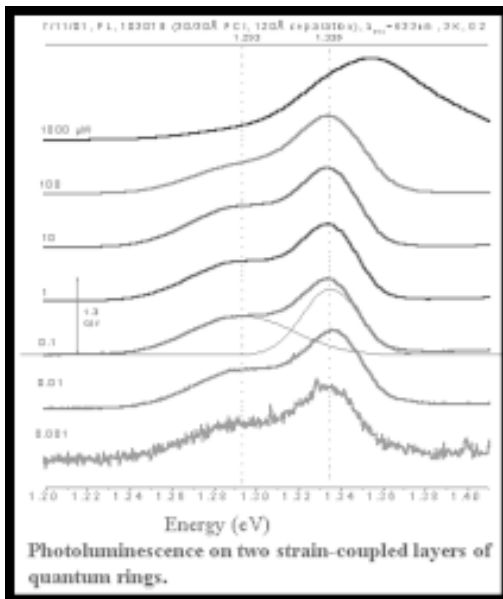
A quantum dot is a region of a semiconductor material embedded in a different surrounding semiconductor matrix that allows the three-dimensional, spatial confinement of carriers. The focus of this research is on InAs QDs embedded in GaAs, which has a larger bandgap energy than InAs. This bandgap energy difference is what allows for the confinement of carriers within a QD. The samples studied were grown using molecular beam epitaxy (MBE). MBE allows for the growth of high purity materials and precise control of layer thicknesses. To fabricate our QDs, a strained layer of InAs is deposited on a GaAs substrate. The lattice mismatch of these two semiconductors is 7%. After 1.65 monolayers, coherent lens shaped islands of InAs form to relieve strain energy. They are nucleated randomly and in a gaussian distribution of sizes. The InAs layer is capped by a layer of GaAs to complete the growth.

This research analyzes strain-coupled QDs. If a closely spaced layer of QDs is grown above another layer, the QDs will preferentially nucleate above one another due to the presence of the strain field that permeates the GaAs capping layer at small spacing ($< 200\text{\AA}$). We operate in the $> 95\%$ pairing probability regime, in which nearly every QD from the first layer is paired with a QD above.

One technique used to alter the properties of the QDs is partially capped islands (PCI). This method increases the spatial confinement in the growth direction, thus increasing the ground state energy of the structure. Instead of fully capping the QDs with GaAs, a thin layer of GaAs is grown whose height (partial capping thickness) is less than the island height. When the GaAs and InAs are allowed to anneal, the QDs form ring shaped structures—quantum rings. These rings have higher energies than normally grown QDs. This technique is useful in this research because it allows tuning of the



Band structure and carrier confinement in QDs



QDs, luminescence energy.

One element of this research was concerned with the optical properties of the different QDs grown. In different samples, we vary the PCI layer thickness and the interlayer spacing (adjusting the strain-coupling). To analyze the optical properties we use photoluminescence (PL). A HeNe laser excites carriers from the bulk GaAs. In hundreds of picoseconds, they find the QD (where they are spatially confined) and settle into the lowest available energy state. In nanoseconds, they recombine and emit a photon of light whose energy is that of the level occupied by the carriers. We detect the energy of this light and are provided with information on the discrete energy levels within the dots. PL has a laser spot diameter of 100 μm and excites millions of QDs simultaneously.

The second component of this research was to look at a layer of uncapped islands using the atomic force microscope (AFM). Statistics were taken at different densities on both a single and a double layer sample. The goal was to characterize each island looked at as a quantum dot or a quantum ring.

Results and Conclusions:

We first examine the results on PL of two strain-coupled, PCI layers. We see two superimposed peaks because two layers of strain-coupled quantum dots luminesce at significantly different energies. Different sized quantum dots in a layer luminesce at slightly different energies. The PL spectrum shows the superposition of all dots, luminescence in a layer, referred to as inhomogeneous broadening. Further results point towards an optimum PCI thickness that allows the two layers to luminesce at the same energy. We also see spectra shift to higher energies at higher powers because carriers enter excited states in quantum dots because ground states are already filled.

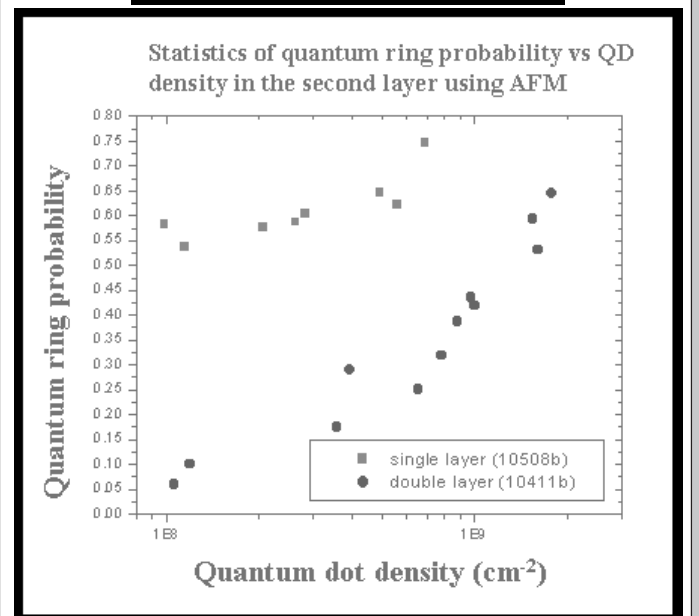
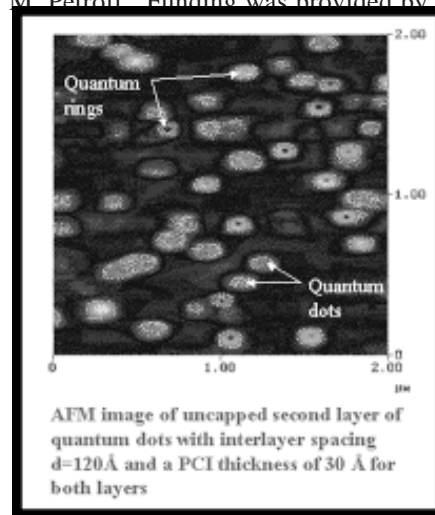
When we examine the AFM results, we find something

rather unexpected. In the single layer sample, we find that for all densities there is a relatively constant quantum ring probability (percent of all islands that are rings), at about 60%. However, for the double layer sample, quantum ring probability drops dramatically as we go to lower density. At high density, 65% of islands are rings, but at low density, a mere 5% are rings. This is unexpected because during the MBE growth process, the PCI layer is applied uniformly over the islands. The best hypothesis is that this is an effect of the strain field, but more research must be done on the subject.

In the future, our group plans to continue to study controlling MBE growth conditions of self-assembled quantum dots. We also plan experiments investigating the electronic coupling of two quantum dots, and analyzing the effects of an applied electric field on a system of closely spaced quantum dots.

Acknowledgements:

Special thanks to the UC Santa Barbara Materials Department especially Brian Gerardot, Itay Shtrichman, and Dr. Pierre M. Petroff. Funding was provided by NNUN and NSF.



AFM Image De-Convolution on Synthetic Spider Silk Protein Fiber

Matthew Kittle, Chemical and Materials Engineering, University of Michigan,
mkittle@engin.umich.edu

*Principal Investigator(s): Dr. Helen Hansma, Physics,
UCSB, hhansma@physics.ucsb.edu*

Mentor(s): Dr. Emin Oroudjev, Physics, UCSB

Abstract:

Atomic Force Microscopy (AFM) techniques can add size and shape to imaged specimens because of tip convolution. This is a problem for biologists who need to know the exact specimen size and shape in order to determine internal structure. We investigated Synthetic Spider Silk Protein Fibers in an effort to solve AFM convolution. Colloidal gold particles as well as DNA plasmid were used as a standard to de-convolute the image of the fibers. Based on the de-convolution, the spider silk protein fiber was determined to be 10nm wide.

Introduction:

The actual image generated by AFM technique is a convolution of the tip's shape and the feature imaged. The tip can add both size and different shape to the specimen. This is still a partially unsolved problem with the AFM, but has been tackled by others [1]. In the course of our research, we attempted other de-convolution methods such as software that used surface imperfections to correct the image, but these were found to be inaccurate. Etched silicon calibration gratings were also considered, but were too large to offer accurate calibration. The height of an etched silicon spike was approximately 4 micrometers whereas the height of a typical spider silk protein fiber was around 2 nm.

We needed a different standard to de-convolute the image. We tested two different calibration methods. In the first method, we used DNA plasmid which has a known diameter of 2nm. In the second, we worked with manufactured gold particles, seen in figure 1, that had a size range between 5 nm and 30 nm. Manufactured gold particles have been used before as method of probe reconstruction [1]. Between the two methods, the gold particles have an advantage because they are incompressible and can be simultaneously co-adsorbed with biomolecules. They also have a known size and shape with documented size distributions, and are relatively inexpensive.

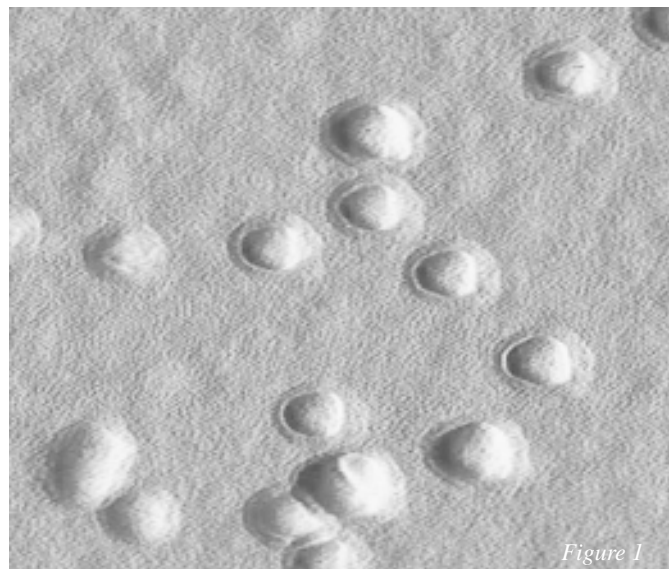
As mentioned earlier, the biomolecules we are imaging are synthetic spider silk proteins. Spider Silk is an amazing material. Even though it is spun at near ambient pressures and temperatures, it has excellent mechanical properties. It is as strong as steel but 6 times

less dense and can stretch between 30 to 200% of its own length. This unique combination makes spider silk mechanically superior to any other natural or man-made material [2]. My mentor has been attempting to elucidate the structure of synthetic dragline spider silk protein, specifically the proteins and arrangements in each fiber segment. The segmented structure can be seen in figure 3.

Experimental Procedure:

We used a pS(4+1) modular recombinant protein. For AFM work on the spider silk protein fiber, we first diluted a stock solution to the desired level. It was then deposited on a newly cleaved mica disk. The solution was incubated on the slide for 3-5 min to give the proteins time to bind to the mica. The sample was then rinsed using MilliQ grade distilled water, and dried under a stream of air purified through a 0.22 μm filter. AFM imaging was done using tapping mode on Multimode AFM using E scanner and Nanoscope III electronics (Digital Instruments, Santa Barbara). All cantilevers for AFM imaging were obtained from Digital Instruments as well. The software used was Nanoscope III versions 4.42r4 and 4.43r8 (Digital Instruments).

To image the gold particles, 20 μL of L-Lysine was deposited on a freshly cleaved mica surface. This was allowed to incubate for 1 min, and then rinsed with the



same MilliQ water as above. Next, the proper size and solution of gold particles were deposited. The solution depended on the size of the particle. The gold particle layer was incubated for 5 min to let the particles adhere. It was then rinsed as above and dried with air.

To find the approximate width of the spider silk protein fiber, the width of a fiber segment was measured. Next using the same tip, images of the gold particles were collected using a 500nm window.

After about 50-60 particles were collected, measurements were taken of height and width. The width measurement was taken in two directions that were perpendicular to each other. The major axis was considered the axis where the tip added some width to the particle. After the average size was determined, it was calculated how much width the tip added. Next this width was subtracted from the measured width of the protein fiber.

Further experiments were done to test the idea of characterizing the tip for possible software aided de-convolution. For this, the widths and heights of three different particle sizes were measured (5 nm, 15 nm and 30 nm), all using the same tip. The width was then graphed vs. the height for the three sizes in one combined series. This was done to test the idea that the tip's shape could be characterized by scanning different sized gold particles. Results can be seen in figure 2.

Results and Conclusions:

After the average gold particle size was determined, it could be deduced that the tip added 16 nm to the width of the fiber. Based on other measurements taken of the spider silk protein fibers, the width was determined to be 10-20nm. This allowed my mentor to calculate the volume of one segment. By knowing the volume of the segment and the density and composition of a single protein module, it could be determined how many modular proteins are in one segment. It was determined to be approximately 16.

Based on the graph in figure 2, a definite non-linear trend is noticeable. This led us to believe we are looking at the shape of the tip. This is only a preliminary conclusion because time ran out for further testing. Viewing the results in figure 2, there seems to be a good basis for using gold particles as a way to de-convolute the image. A mixed gold particle sample with a variety of sizes could be scanned and then computer software could calibrate the tip. When it comes time to image the sample, the software can automatically de-convolute the image. The Hansma lab has the resources to develop this technique and software and most likely will.

In conclusion, gold particles appear to be a quick and inexpensive way to determine the size of biomolecules. Further research needs to be done on the accuracy and reproducibility.

References:

- [1] "Three-dimensional probe reconstruction for atomic force microscopy", J. Vesenka, R. Miller, E. Henderson, Rev. Sci. Instrum. 65(7), July 1994.
- [2] "Liquid crystalline spinning of spider silk", F. Vollrath, D.P. Knight, Nature, vol. 410, pp. 541-548, March 29, 2001.

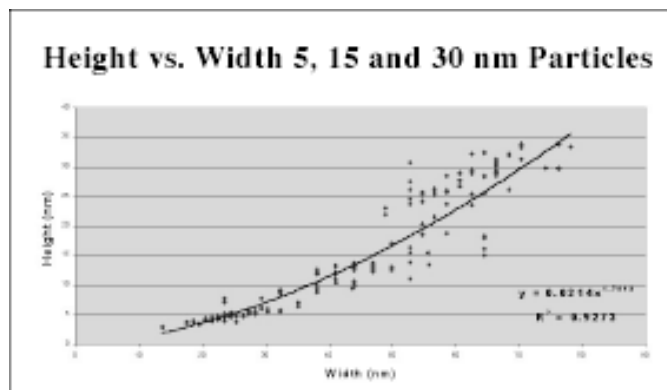


Figure 2. Synthetic Spider Silk Protein Fiber showing each segment.

MicroElectroMechanical Chemical Sensors

Hayley Lam, Bioengineering, University of California, Berkeley,
hayley74@uclink4.berkeley.edu

Principal Investigator(s): Kimberly L. Turner, Mechanical Engineering,
University of California, Santa Barbara, turner@engineering.ucsb.edu

Mentor(s): Rajashree Baskaran, Mechanical Engineering, UCSB

Abstract:

The potential for MicroElectroMechanical Systems (MEMS) in sensor applications has long been recognized. We attempt to build an improved resonant chemical sensor with MEMS by modifying the surface of the device. Specifically, basic electrochemical techniques are used to form a porous silicon (PS) layer on mobile parts of the device, creating a greater binding area, followed by activation of the PS surface with various molecules. The device can then be used as a sensor of molecules that bind to the activated PS surface by observing the change in the frequency response of the device with laser vibrometry.

Introduction:

MEMS is a broad term used to encompass many different kinds of devices fabricated on the micron scale, such as sensors, actuators, and instruments [1]. These devices are usually fabricated with integrated circuit technology on a silicon substrate.

MEMS as microsensors are a very practical idea, since the size of the device would be advantageous, and the ease of integration with standard IC technology would facilitate manufacturing. Currently, there is a large amount of research devoted to the biosensor applications of MEMS due to the potential for biological applications. The type of sensor we hope to build would be a more generic type of sensor of various inorganic chemicals, and not involve many of the complications associated with compatibility in a biological environment, such as the human body. In addition, much of the current research on sensors has involved simple MEMS structures, such as cantilevers. The type of MEMS device we would like to use is a much more complex system that can act as both a sensor or actuator — that is, the device can be used to sense displacements or induce motion.

The device, as shown in Figure 1, has several interesting characteristics. The device is a torsional oscillator that moves out of plane due to an asymmetric electric field generated by an applied voltage [1]. The torsional motion of the device can be modeled using a damped Mathieu equation, and this allows us to predict the unstable regions of motion. The importance of the unstable resonance of the device is illustrated in Figure 2. At a very specific frequency, the system will change from

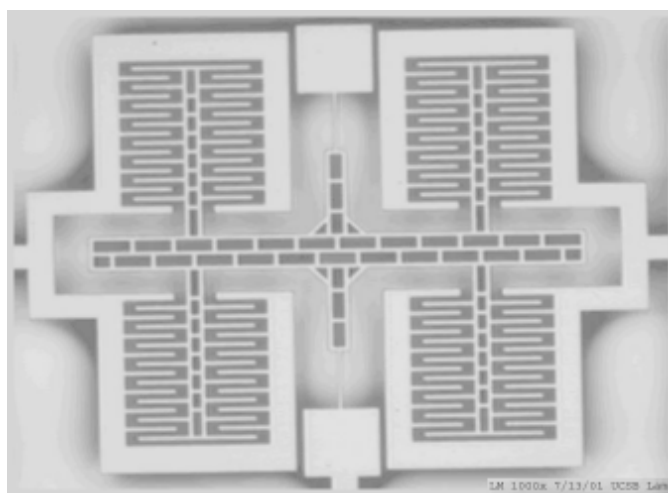


Figure 1: Torsional Oscillator

stable to unstable motion. The large change in the amplitude of motion is useful as a predictable switch, which is useful for integration in IC technology where a defined on/off signal is essential for accurate performance.

The unique response of the system can be used in sensor applications, with a few modifications. A porous silicon (PS) layer is selectively etched on the movable part of the device to increase the surface area, and thus, the sensitivity, of the device. Then, the device will be activated by binding a chemical sensing molecule to the PS. This modified device should have a predictable resonance that will change when the specific chemical the device is sensing comes in contact with the activated device. Connected circuitry with the device can use the change in the response of the device as a signal that there is sensing of the chemical.

There are two main components to the functionality of sensor. First, the original device must function predictably over time given a certain environment. Second, we must be able to modify the device by forming the PS layer and activate the surface in a reliable and consistent fashion. This project focused on developing the PS layer.

Procedure:

Porous silicon (PS) was fabricated with a Teflon

electrochemical cell as shown in Figure 3. P-type (100) silicon wafers were cleaned, and a small amount of palladium was added to the unpolished side of the wafer to increase conductivity. Silicon, acting as the cathode, was etched in ambient conditions in hydrofluoric acid with platinum as the inert anode. Varying current densities were applied to the cell for various amounts of time to optimize the formation of the PS. Samples were examined under Scanning Electron Microscope (SEM).

Results:

We were unable to consistently form a porous silicon layer on wafers. Although basic techniques were similar to those in the literature, SEM pictures do not show uniform pores under any of the different etching conditions. A definite layer is formed on the upper surface of the wafer, but the layer is not identifiably porous throughout. Pores are formed on the edges of etched columns, but not in the bulk. Polishing the surface of one of the wafers shows pores, however, the pores are only located in certain areas and are not uniform. Work is continuing in this area to create repeatable samples.

Conclusions:

Further testing of the device to better define the characteristics of the system, and to determine reliability are necessary. In addition, changes need to be made in our attempts to form the PS; current methods have not been entirely successful. We have been unable to determine a definite cause for the inconsistencies of PS formation. However, since PS has been fabricated previously, the processing of a new type of chemical sensor is very much in the making.

Acknowledgements:

Thanks to Rajashree Baskaran and Kimberly Turner for their inspiration, knowledge and support this summer, and to the rest of the Turner lab. Special thanks to Mark Cornish and Martin Vandenbroek. Funded by the National Science Foundation (NSF) and Defense Advanced Research Projects Agency (DARPA).

References:

[1] Turner, K. L., et al., Five parametric resonances in a microelectromechanical system. *Nature* 396, 149-152 (1998).

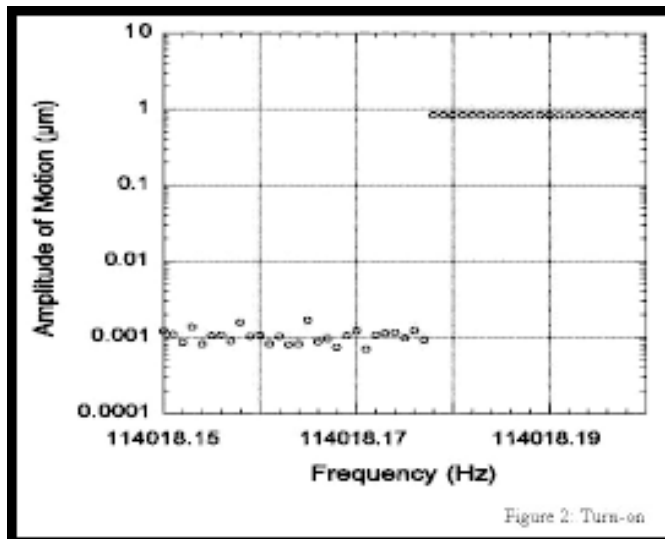


Figure 2: Turn-on

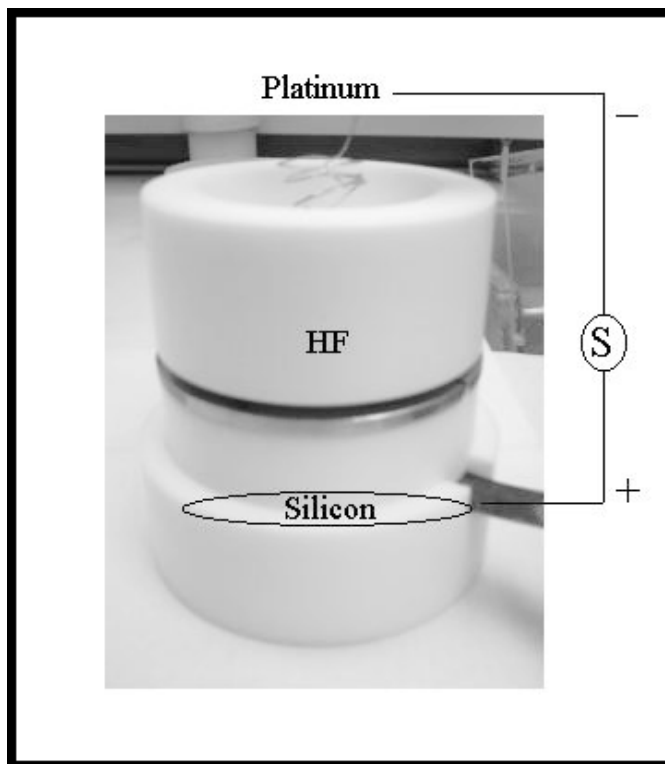


Figure 3: Electrochemical Cell.

Asymmetric Diblock Copolymer Films for Nanopatterning

Kathleen E. Schaefer, Chemistry, University of Pittsburgh, kesst42@pitt.edu

Principal Investigator(s): Edward J. Kramer, Materials Science and Engineering Department, University of California at Santa Barbara, edkramer@mrl.ucsb.edu

Mentor(s): Rachel Segalman, Chemical Engineering Department, University of California at Santa Barbara

Abstract:

Two techniques, dynamic secondary ion mass spectrometry (SIMS) and optical microscopy on a heat stage, were used to investigate the process of self-assembly of poly(styrene-*b*-2vinylpyridine) (PS-PVP). PS-PVP of specific block lengths forms arrays of spheres 30nm in diameter when annealed under vacuum; SIMS depth profiles of samples annealed under various conditions were analyzed to optimize annealing to produce the highest degree of order perpendicular to a substrate. Optical microscopy of films on patterned substrates provides a more detailed picture of the mobility of the polymers and how they reach an ordered state, allowing for a greater degree of control over the ordering process.

Introduction:

Through the process of self-assembly, block copolymers can be used to produce various morphologies on a size scale unachievable through conventional patterning techniques. By controlling the chemical composition of these polymers, structures such as nano-scale lamellae and arrays of cylinders or spheres can be produced [1]. Although the ordering process is relatively well understood for lamellar and cylindrical morphologies, the factors that affect ordering of spherical

domain block copolymers have been less extensively studied. Through a detailed understanding of how these polymers reach an ordered state, we will be better able to control long-range patterning and generate specifically designed structures.

SIMS depth profiling provides a chemical picture of the composition of a sample as a function of distance perpendicular to the sample surface. The chemical difference between polystyrene and polyvinylpyridine thus generates signal oscillations in the SIMS depth profile corresponding to successive layers of polyvinylpyridine cores within a polystyrene matrix. Ordering is induced by the substrate and vacuum surfaces of a PS-PVP film, so depth profile signal oscillations will persist deeper into the film as annealing conditions improve. By analyzing films prepared under various conditions, annealing can be optimized to produce the highest degree of order.

Control in the direction parallel to the substrate, in contrast, can be achieved through topographical patterning of the substrate [2]; when films of incommensurate thickness (non-integer multiples of the diameter of a single sphere) are cast on patterned substrates, islands and holes form from excesses or deficiencies of material. Changes in the size of these islands and holes over time can be monitored through optical microscopy with a heat stage to allow for the calculation of the diffusion coefficient of the polymer, providing insight into the nature of mobility of PS-PVP. With a detailed understanding of the mechanism of ordering of PS-PVP, controlled patterning on the nanometer scale will become a simple task; arrays of nanometer sized ordered spheres could be produced quickly and easily, ultimately proving useful in numerous applications such as nanolithographic templating and the fabrication of membranes [3].

Experimental Procedure:

Samples for SIMS depth analysis were prepared by spin casting films at least 1mm thick onto SiO₂ coated silicon wafers. Films consisted of blends of PS-PVP block copolymer and polystyrene (PS) homopolymer ranging from 0 to 50% PS. Samples were annealed under high vacuum (10⁻⁶ Torr) at temperatures ranging from

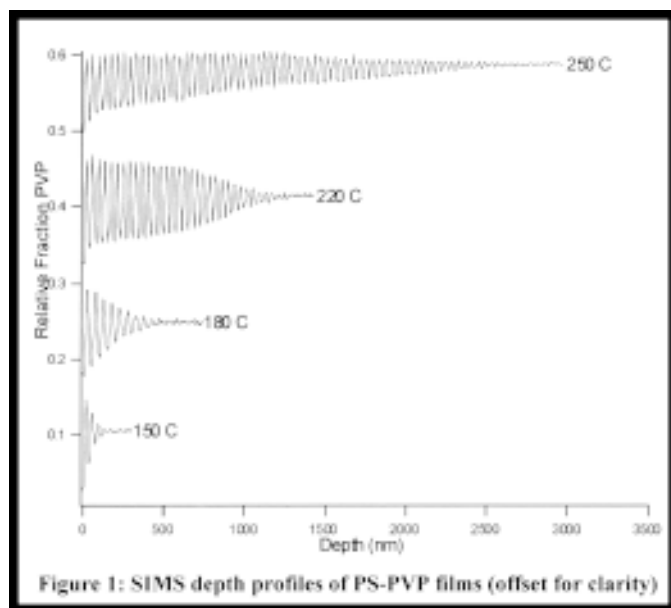


Figure 1: SIMS depth profiles of PS-PVP films (offset for clarity)

150°C to 250°C for 24 or 72 hours. To provide depth calibration in the SIMS, a sacrificial layer of deuterated polystyrene (dPS) of known thickness was floated onto each sample after removal from the oven.

In a separate experiment, the kinetics of nanodomain ordering was observed via optical microscopy of surface topography evolution on a heat stage. Topographically patterned substrates were obtained from Rachel Segalman. Films of various thicknesses of PS-PVP were floated onto the substrates; evolution of the film was observed through time-lapse photography over the course of approximately five days at a temperature of 180°C.

Results and Conclusions:

Through SIMS depth analysis, order perpendicular to the substrate was found to vary as a function of both temperature and fraction of PS homopolymer present in the blend; the greater the fraction of PS and the higher the annealing temperature, the farther ordering persisted into the film (see figure 1). The trend observed through addition of homopolymer could be explained by an increase in the mobility of the diblock chains; increasing the concentration of homopolymer essentially decreased the molecular weight of the matrix through which the chains moved.

A series of photographs was also taken demonstrating the formation and evolution of islands and holes on a topographically patterned substrate (see figure 2a-d). From these images, it can be concluded that the surface topographies coarsen as a function of time by the movement of material from the raised mesas (dark stripes) to fill the wells (light stripes). Furthermore, this movement is accomplished solely by the shrinkage of each individual island; no island is observed to migrate

across the surface. This indicates that diffusion is accomplished entirely by the movement of individual chains from one region to the next. The diffusion coefficient of the polymer will be calculated by measuring the change in area of individual islands as a function of time. This two-dimensional diffusion coefficient will be compared to that already reported in three dimensions. Atomic force microscopy pictures will also be taken to verify the topography within the islands and holes of the film.

From these two pieces of information, the optimal annealing conditions and the behavior of the polymer on topographically patterned substrates, mechanisms of nanodomain ordering will be further elucidated, eventually providing more precise control over the ordering process, allowing for films to be formed that exhibit long-range order and can prove useful for patterning and fabrication applications.

Acknowledgements:

Many thanks to Rachel Segalman, Prof. Ed Kramer, Alex Hexemer, and Tom Mates for their help and support. This project was funded by the NSF DMR Polymers program and NNUN, and made use of the Materials Research Laboratory at UCSB.

References:

- [1] Bates, F.S., Fredrickson, G.H. *Physics Today* 52 (2): 32-38, 1999.
- [2] Segalman RA, Yokoyama H, Kramer EJ, *Advanced Materials* 13 (15): 1152-1155, 2001.
- [3] Park M, Harrison C, Chaikin PM, et al. *Science* 276 (5317): 1401-1404, 1997.

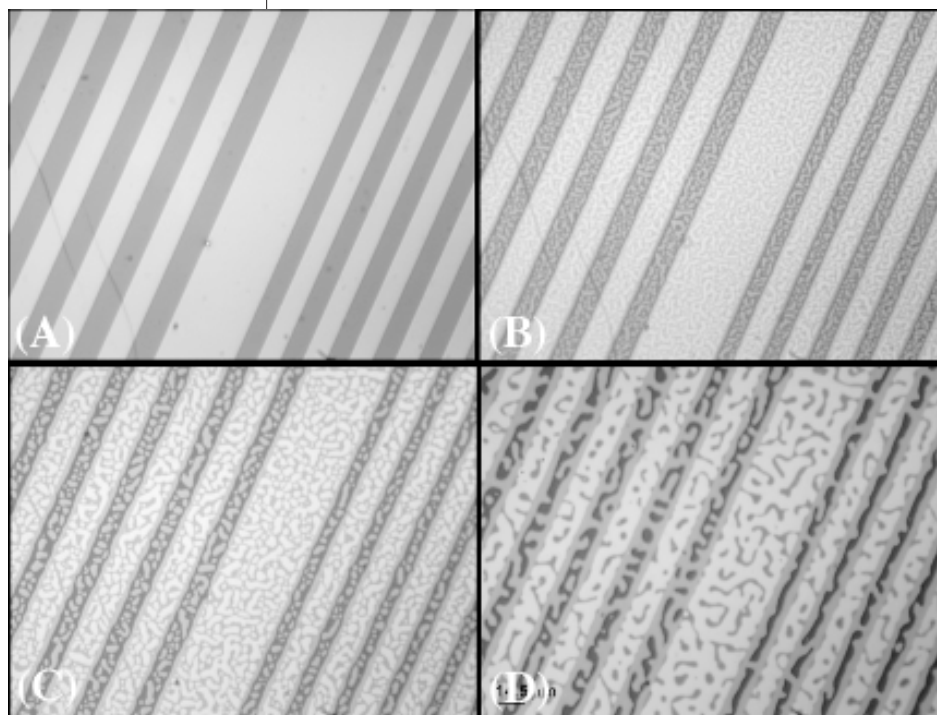


Figure 2:

- (A) 0 mins.
- (B) 204 mins.
- (C) 940 mins.
- (D) 7102 mins.

Spectroscopy of the Ir³⁺ Organo-Metallic Complexes

Metages Sisay, Engineering Physics, Santa Clara University, msisay@scu.edu

Principal Investigator(s): Vojislav Srdanov, Center for Polymers and Organic Solids, UC Santa Barbara, srdanov@chem.ucsb.edu

Abstract:

We present a basic spectroscopy study of three organo-metallic complexes containing phenyl-pyridine ligands with a varying number of phenyl groups attached. Such compounds are known to be potent electro-luminescent materials used in organic light emitting diodes (OLEDs). There are two important excitations which determine the electro-luminescent spectrum of these complexes: the first excitation involves only the organic part of the complex while the other involves metal-to-ligand energy transfer. To this point, we collected absorption, emission and photoluminescence (PL) spectra of the three Iridium complexes in solution and solid thin films at 77 and 300K. The following are the observations we gathered so far:

- 1] We observe a red-shift of the absorption and emission bands with the increase of the ligand conjugation length.
- 2] The most red-emitting complex (the one with the longest ligands) is sensitive to photo-oxidation while the others are not.
- 3] The PL spectra of Ir³⁺ complexes shift to the red at lower temperatures.
- 4] There are two types of emission bands that can be distinguished by their emission life-times: the weak ones which have the life-time of about 530 ns and the strong ones which last for about 1.5 μ s.

Introduction:

Everyone is familiar with polymers as flexible yet mechanically strong materials. Less well known is the fact that some polymers can also conduct electricity and emit light. These semi-conducting polymers, which have been intriguing researchers for the past 20 years, are now poised to enter the market place.

Efficient light emitting diodes (LEDs) can be made from very simple structures. The first one was made

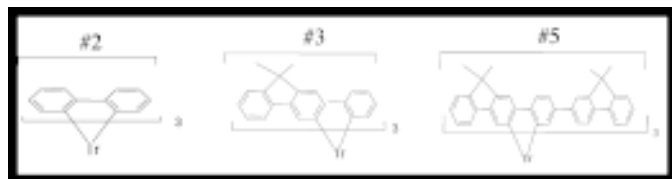


Figure 1: The three iridium complexes.

around 1990 by Richard Friend and Jeremy Burroughes. They used a thin layer of polymer sandwiched between a pair of electrodes. The negative electrode injects electrons while the positive electrode injects holes in the polymer. When holes capture electrons neutral excitons are formed, which decay by emitting photons. For this process to work, the negative electrode must have low work-function while the positive one has high work-function so that electrons and holes are injected easily. Most of the time, the hole electrode is made out of indium-tin oxide, which is optically transparent thus allowing the emitted light to leave the device.

LEDs made with just a polymer film and the electrodes have broad PL and relatively low quantum efficiency, which means the number of the electron-hole pairs injected by far exceeds the number of photons emitted. This limitation is related to the selection rule forbidding singlet-triplet emission in the light atoms and/or molecules. This rule is broken, however, if a few percent of some heavy metal is blended into the polymer. This project focuses on photochemistry of several organometallic Iridium complexes mixed with conjugated polymers in order to increase their quantum efficiency.

Experimental Procedure:

The absorption spectra of the three Iridium complexes (see Figure 1) dissolved in dichloromethane were recorded using a HP-8452A Diode-Array Spectrophotometer, while their emission and excitation spectra were recorded with a PTI fluorimeter. The same measurements were performed on the thin films of these compounds spin-coated on a glass substrate but this time, we also measured the PL lifetime. The PL spectra were excited by an Ar⁺ laser operating at 457 nm and 488 nm while the lifetime measurements were performed with pulsed Nd-YAG laser operating at 355 nm. The emitted light was focused onto a 1/2 m monochromator (Acton Research

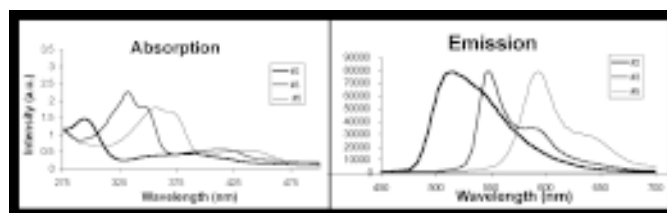


Figure 2: Red-shift in absorption and emission spectra.

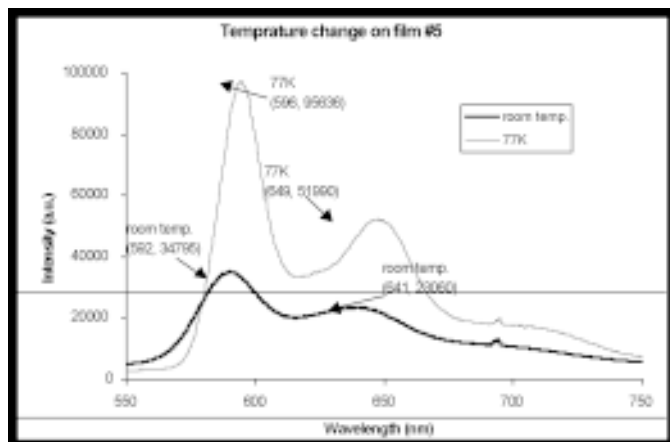


Figure 3: PL spectra of #5 at different temp.

500-Pro) whereas for the lifetimes, we used a 400 MHz Tektronix oscilloscope (model 2467 B) equipped with a digital video camera (model C1001). The PL lifetime was measured at both room temperature and 77 K.

Results:

As shown in Figure 2, the emission and absorption spectra shift towards the longer wavelengths (the red shift) with an increase of the number of conjugated phenyl rings in the Iridium complex. This shift can be explained by the quantum-mechanical “Particle in the box” model which states that: “the longer the size of the conjugated molecule (the box length) the smaller is the spacing between the energy levels.”

We also found that the PL intensity increases at lower temperatures (see Figure 3), which is to be expected since the probability of nonradiative decay processes (phonon quenching) goes down. A small red shift is also noticeable at lower temperatures, but we don’t have a clear explanation for this shift at this point.

Figure 4 is the lifetime of #5 at room temperature and 77K. As it is shown, there are two different components of lifetime when you go to low temperature. The PL spectrum also depends on the environment.

When you take a PL spectrum of a solid and compare it to a thin film as shown in Figure 5, there is an appearance, or intensity change, of a new band. This might be due to the energy states of the complexes.

The lifetime measurements indicate a presence of two different excited electronic states; one with the long lifetime (1.5 ms) and one with a short lifetime (~500 ns). The interesting thing is that PL quantum efficiency for the two states changes differently with temperature, indicating different type of relaxation processes.

Another interesting result is that the most red-emitting complex, #5, is sensitive to photo-oxidation while the others are not.

Conclusion:

This work is in the initial stage of a study aimed towards better understanding of the energy transfer processes in the organometallic complexes and the way they should be used to enhance the performance of the polymer-based LEDs.

Acknowledgements:

Vojislav Srdanov
Jacek Ostrowski
ONR, NNUN, NSF

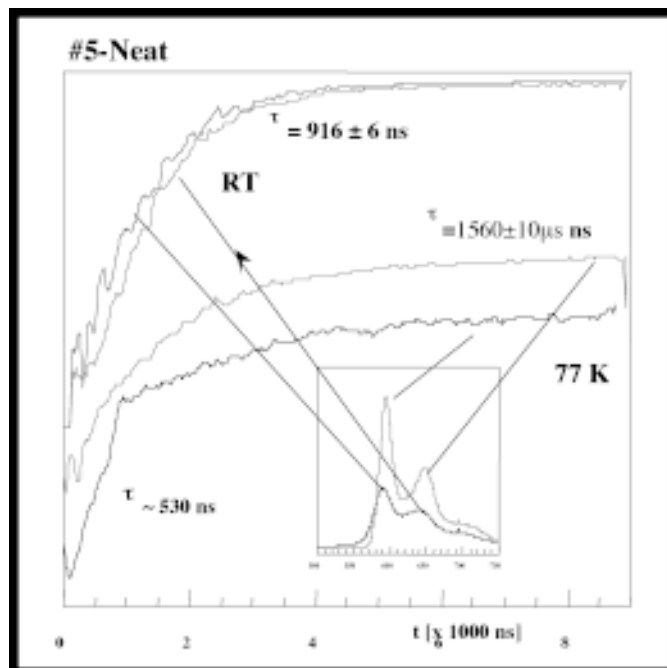
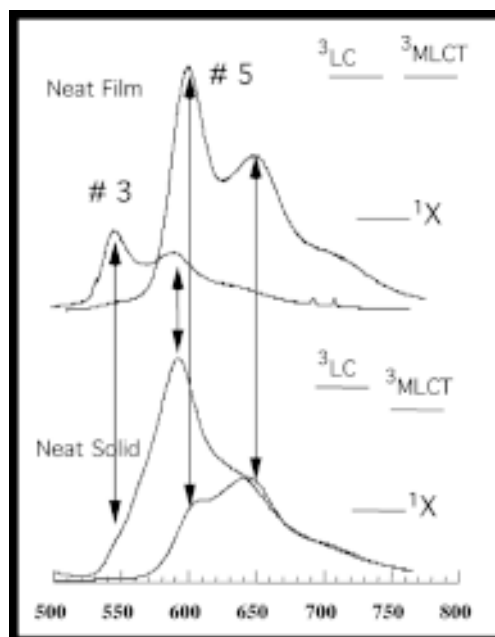


Figure 4, above: Lifetime of #5 at different temperature and band of PL.
Figure 5, below: Comparison of PL between Film and Solid.



Conformational Analysis of Phenylenevinylene Oligomers

Chau Tang, Polymer Science, University of Southern Mississippi, Ngoc79@aol.com

Principal Investigator(s): Guillermo C. Bazan, Chemistry and Materials,
University of California at Santa Barbara (UCSB), Bazan@chem.ucsb.edu

Mentor(s): Jacek Ostrowski and Matthew Robinson, Chemistry and Materials, UCSB

Abstract:

Synthesis and spectroscopic analysis of two oligophenylenevinylenes is described herein. Oligophenylenevinylene molecules constitute a fundamental basis for studying intermolecular interactions and charge transfer within conjugated polymers. Conformationally selective ion spectroscopy is used to determine the shape of 4,4'-Distyryl-(2,2',5,5'-tetraethyloxystilbene) (**4OPV**) and 1,4-Bis-[2',5'-dioctoxy-4'-(4''-(3''',5'''-dihexyloxystyryl) styryl) styryl] benzene (**9OPV**). A model of their conformations was constructed to determine the relative amount of *cis*-defects within the bulk. This model can further be used to define *cis*-defects in polyphenylenevinylene polymers. These novel molecules are synthesized using Heck, McMurry, and Wittig coupling reactions.

Introduction:

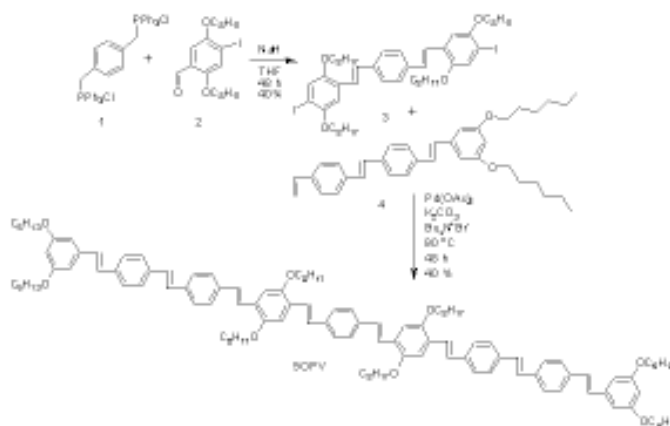
Cis-bonds yield lower electroluminescence and photoluminescence quantum efficiency in the bulk; hence, they are considered defects. Oligomers of phenylenevinylene will contain a certain percentage of *cis*-bond defects. Conformationally selective ion chromatography is a new technique that has been developed by the Bowers group at UCSB [1]. This technique can determine the shape and thus *cis*-bond defect content of molecules. The synthesis of 4,4'-distyryl-(2,2',5,5'-tetraethyloxystilbene) (**4OPV**) makes use of this analytical technique.

A disadvantage with this method is that as the size of a molecule increases, it becomes more difficult to compute mobility and relative abundance of the conformations. Because of its size, bis-[2',5'-dioctoxy-4'-(4''-(3''',5'''-dihexyloxystyryl) styryl) styryl] benzene (**9OPV**) will be difficult to model using conformationally selective ion chromatography. However, the method is a reliable procedure to determine the *cis*-defect content of the **4OPV** molecule, and the *cis*-defect content of **9OPV** should be similar to the *cis*-defect content of the **4OPV** molecule. The data about molecular conformations provided by the experiment can be used to understand the shapes of the oligomers and polymers in films. This data can also be used by researchers who are interested in other methods of research, such as single molecule spectroscopy.

Experimental Procedure:

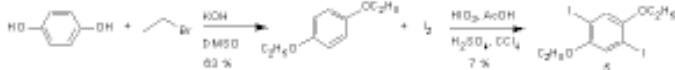
The preparation of the **9OPV** started by treating 1,4-dibenzyltriphenylphosphonium chloride (**1**), 3,6-dioctyloxy-4-iodo-benzaldehyde (**2**), and sodium hydride in THF and stirring for 2 days to yield 1-(4'-styryl-styrylbenzene)-4-(3',5'-dihexyloxystyrylbenzene)-benzene (**3**) using Wittig coupling reaction. In a Heck coupling reaction, **3** and 1,4-di(2',5'-dihexyloxy-4'-iodostyrylbenzene)benzene (**4**) were added to a flask with palladium acetate, potassium carbonate, and tetrabutylammonium bromide, which was degassed 3 times, heated to 90°C, and stirred for 48 hours, to give the **9OPV**.

Scheme 1:



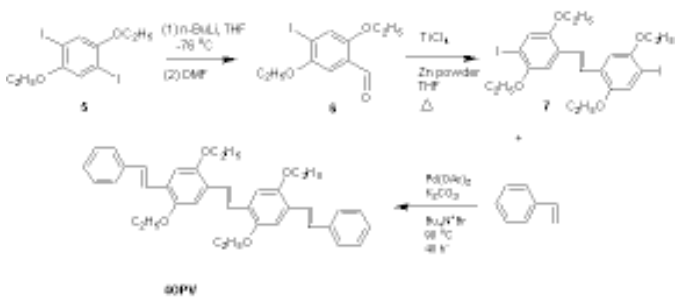
For the synthesis of **4OPV**, the ethylation of hydroquinone with excess ethyl bromide and potassium hydroxide in DMSO provided the 1,4-diethyloxybenzene derivative. The 1,4-diethyloxybenzene compound was further treated with iodine, iodic acid, acetic acid, sulfuric acid, carbon tetrachloride, heated at 40°C, and stirred for five hours to give 1,4-diethyloxy-3,6-diiodobenzene (**5**).

Scheme 2: Part A



The derivative from the previous step was converted into 3,6-diethoxy-4-iodobenzaldehyde (**6**) by lithiation with *n*-butyl lithium in THF at -78°C then treating with DMF. Compound **6** undergoes a McMurry coupling condition with titanium tetrachloride and zinc powder in THF while refluxing for three hours to provide 2,2',5,5'-tetraethoxy-1,1'-diiodostilbene (**7**). With Heck coupling conditions, using **7** and styrene gave the **4OPV**.

Scheme 2: Part B



All compounds were characterized using ^1H and ^{13}C nuclear magnetic resonance (NMR), mass spectroscopy, gas chromatography mass spectroscopy, laser desorption ionization, and high pressure liquid chromatography (HPLC).

Conclusion:

The synthesis of the **9OPV** was successful. Several complications of synthesis arose during the production, characterization, and purification processes. The Heck coupling reaction was the most difficult step in making the desired molecule due to two factors: (1) The catalyst

dies if a reaction temperature exceeds over 100°C , (2) oxygen that is introduced would cause the reaction to fail. The difficulty in characterizing the **9OPV** was due to its structure being complex and large. The molecule has many double bonds, which lead to many isomers; therefore, NMR data were complicated to interpret. With the different isomers and other molecules that interact closely to the **9OPV** on a chromatographic column, the purification step was long and laborious. Several cycles of column chromatography were used upon the compound to ensure complete purity. If the compound was not clean, then using it for single molecule spectroscopy can affect the results. Thus, the compound was analyzed by HPLC to ensure its purity.

Due to time constraints, the **4OPV** is not yet finished. However, some precursors have been developed for continuation and completion of this molecule. One problem experienced in making the **4OPV** was getting a low yield of **5**.

Conformationally selective ion chromatography can be used to directly determine *cis*- defects of **4OPV** and **9OPV**. Since the structure of **9OPV** approaches polymeric dimensions, its deficiencies can be related with conjugated polymers to determine the fitness of the bulk for application purposes.

References:

- [1] Gidden, J.; Wytenbach, T.; Jackson, A.T.; Scrivens, J.H.; Bowers, M.T. *J. Am. Chem. Soc.* 2000, 122, 4692-4699.
- [2] Ulf Stalmach, Heinz Kolshorn, Isabella Brehm, and Herbert Meier. *Liebigs Ann.* 1996, 1449-1456.



**Thank you
all for a
wonderful
summer!**

INDEX

A

Albrecht, Andreas C. 22
Allara, David 48
Alvarez, Sara 81, 82

B

Bacon, Anna E. 5, 6
Baeumner, Antje 24
Bakhru, Nitasha 81, 84
Baskaran, Rajashree 96
Bawazer, Lukmaan 81, 86
Bazan, Guillermo C. 102
Beck, Noah 55, 56
Benghale, Hemant 20
Bixby, Teresa J. 41, 42
Blakely, Jack 10
Boxer, Steven G. 62
Bracero Rodriguez, Julio 31, 32
Brickey, Mary C. 81, 88
Brink, Paul 70

C

Cabrera, Blas 70
Carter, Arthur Francis, Jr. 41, 44
Chang, Aileen 55, 58
Chen, Nianhuan 90
Choi, Philip 5, 8
Clemens, Bruce M. 78
Cuiffi, Joe 44, 46

D

Dai, Hongjie 58, 72
Daniel, Tad 48
Daniels, Matthew 5, 10
Daub, Lisa 41
Davenport, Andrew 55, 60
Deal, Michael 55
DenBaars, Steven 86
Devereaux, Caitlin 5, 12
Diallo, Mamadou 32

E

Engstrom, James 14
Ercius, Peter 81, 90
Eshiet, Unyime 31, 34

F

Fischer, Peer 22
Flink, Albert 81
Fonash, Stephen 44, 46
Fontaine, Jamie 41, 46
Franklin, Nathan 58, 72
Freedman, Danna 5, 14

G

Gerardot, Brian 92
Griffin, James 32, 36
Griffin, Peter 66, 76

H

Hansma, Helen 94
Harness, Ashley 5, 16
Harris, Gary 31, 32, 34, 36, 38
Hatzor, Anat 52
Hayes, Dan 44, 46
Hebert, Damon N. 81, 92
Hellstrom, Sondra 55, 62
Horn, Mark 41
Hubbi, Samar 55, 64

I

Israelachvili, Jacob 90

J

Jensen, Noel 55, 66
Jones, Kimberly 38

K

Kam, Lance 62
Kan, Edwin C. 8
Katona, Thomas 86
Kim, Myongseob 8
Kittle, Matthew 81, 94
Klein, Kate 55, 68
Klein, Robert 31, 36
Kramer, Edward J. 98
Kwakye, Sylvia 24

L

Lam, Hayley	81, 96
Lavallee, Guy	52
Liu, Joy	41, 48
Liu, Ying	50
Lui, Natalie	55, 70

M

Ma, Paul	14
Maiga, Fatou	5, 18
Malliaras, George	12
Mallison, Melanie-Claire	5
Manuel, Brian	5, 20
McElroy, Meredith	5, 22
Metwalli, Ezz	42
Mitragotri, Samir	84, 88
Moler, Kathryn	56
Morris, Nathan	55, 72
Morse, Daniel E.	82
Moussa, Laura	5, 24

O

Ober, Christopher	26
Ohsie, Linda H.	55, 74
Oroudjev, Emin	94
Ostrowski, Jacek	102

P

Pantano, Carlo	42
Pease, Fabian	60, 68
Petroff, Pierre M.	92
Pham, Victor Q.	26
Phillips, Mark	78
Pickard, Dan	60, 68

R

Rao, G. Nagesh	5, 26
Rathbun, Lynn	6
Robinson, Matthew	102
Roman, Gregory T.	5, 28
Rosario, Mari-Anne	50
Russell, Heather	41, 50

S

Schaefer, Kathleen E.	81, 98
Schramm, Joy	84
Schroeder, Todd	14
Schuller, Jonathan	55, 76
Segalman, Rachel	98
Sisay, Metages	81, 100
Skvarla, Michael	18
Sofos, Marina	55, 78
Spencer, Michael G.	20
Srdanov, Vojislav	100
Sumerel, Jan	82
Swiggers, Michele	12

T

Tadmor, Rafael	90
Tang, Chau	81, 102
Tang, Mary	64, 74
Taylor, Crawford	36
Tezel, Ahmet	88
Tiwari, Sandip	6
Tran, Linh My	81, 90
Turner, Kimberly L.	96

U

Umbach, Christopher	10
---------------------------	----

W

Wang, Pingshan	8
Wang, Qian	58
Weiss, Paul S.	52
Williams, Yvette	31
Wilson, Court	31, 38
Wissner-Gross, Alexander D.	41, 52
Woodie, Daniel	5, 16, 28
Wynn, Janice	56

Z

Zhang, Yeugang	58
Zhou, Peizhen	34